Unravel the Effects of Locally Resonant Metamaterials on Hydroelastic Membranes for Wave Energy Modulation

Master of Science

Chen Liang

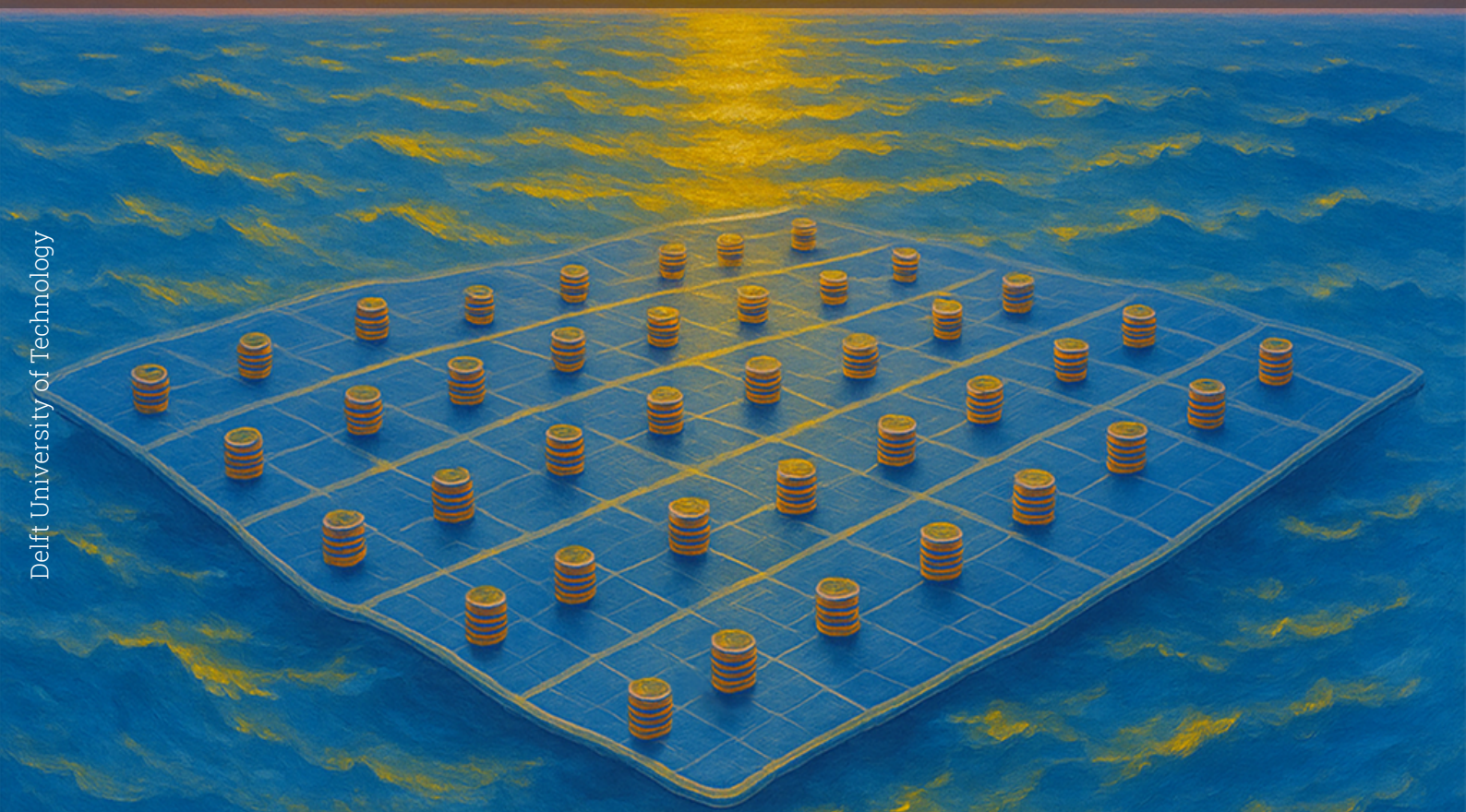

Delft University of Technology

TU Delft

Unravel the Effects of Locally Resonant Metamaterials on Hydroelastic Membranes for Wave Energy Modulation

by

Chen Liang

to obtain the degree of Master of Science

at the Delft University of Technology,

to be defended publicly on Thursday November 27, 2025 at 15:00 PM.

Student number:	6055303	
Project duration:	April 10, 2025 – November 27, 2025	
Thesis committee:	Dr. ir. J.O. Colomes Gene,	TU Delft, chair
	Dr. ir. S. Agarwal,	TU Delft
	Dr. ir. A. B. Faragau,	TU Delft

An electronic version of this thesis is available at http://repository.tudelft.nl/.

TU Delft

Preface

This thesis marks the culmination of my graduation project that has accompanied me through a long and enjoyable journey. When I first began, I had limited knowledge of this topic and unfamiliar with the new coding language. Over time, however, I grew from uncertainty to confidence, gradually developing the ability to understand the underlying physics, implement complex models, and interpret the results to the reader. Through this process, I saw myself progress as a researcher—gaining not only technical skills, but also independence, patience, and resilience.

The process was far from linear. There were ups and downs, unexpected issues, hours spent debugging, and moments of frustration. Yet, every time a figure finally made sense, a simulation ran successfully, or an insight emerged from the data, I felt a deep sense of accomplishment. I genuinely enjoyed the period of focused and peaceful research that this project allowed me to experience.

This work would not have been possible without the people who supported me throughout this journey. I am sincerely grateful to my supervisors, Andrei, Oriol and Shagun. Their constant guidance, incredible patience, and professional insights helped me push through many difficult stages of the research. I also want to thank my friends for their companionship and motivation, and my family for their unconditional support. They have been my strongest foundation.

Looking back, this project has strengthened not only my academic skills, but also my spirits to learn independently, stay resilient, and find joy in solving challenging problems. For all of these experiences, I am truly thankful!

Chen Liang
Delft, November 2025

Summary

This study investigates the integration of local resonant metamaterials (LRMM) into floating membrane systems to enhance their wave energy interaction performance. The primary objective is to numerically examine how LRMM influence the dynamic response and energy characteristics of a coupled fluid–structure system, with a particular focus on wave reflection, transmission, and absorption under different configurations and excitation frequencies.

Floating membranes have gained attention as novel candidates for wave energy converters (WECs) and floating breakwaters due to their lightweight, flexible properties and adaptability to marine environments. However, they are less effective at lower frequencies and near their structural natural frequencies, where wave transmission becomes dominant and energy absorption is low. Insights from previous studies in acoustic and elastic metamaterials suggest that local resonators may introduce bandgaps that block wave propagation in certain frequency ranges. Motivated by this, the current work explores whether similar principles can be applied to enhance hydrodynamic control in floating membrane systems.

The numerical model is built upon a monolithic finite element framework that handles strong fluid–structure coupling in a unified variational formulation. The fluid is governed by a linear free-surface potential flow model, while the membrane is treated as a pre-tensioned one-dimensional structure. A linear single-degree-of-freedom (SDOF) viscoelastic model is used to describe the dynamics of the LRMM. This setup enables consistent coupling and modal analysis across mixed-dimensional domains, and serves as the foundation for all simulations performed in this study.

A comprehensive set of dry and wet modal analyses reveal that LRMM introduce new resonant modes that are strongly frequency-selective and spatially localized. The presence of LRMM also alters membrane-dominated modes, with effects depending on resonator frequency, mass, and placement relative to modes. Frequency-domain simulations further demonstrate that LRMM can significantly reduce wave transmission and amplify reflection when resonance occurs, even suppressing the structural resonance of the membrane itself. These results confirm the potential of LRMM to induce bandgaps in water wave systems and to function as passive wave control devices.

Extensive parametric studies were conducted to systematically examine how key resonator properties—including natural frequency, spatial placement, mass, and damping—affect the system's energy behavior. The results provide clear design insights, such as optimal placements aligned with antinodes and damping-tuning to maximize absorption. Finally, a realistic sea-state scenario based on a scaled JONSWAP spectrum was simulated to assess the effectiveness of the system in practical conditions. The findings demonstrate that LRMM can meaningfully reduce the downstream wave loading and increase wave energy absorption over a target frequency band, highlighting its application potential in floating structures.

In summary, this work provides a systematic numerical investigation into LRMM-enhanced floating membrane systems, establishes a rigorous modeling and simulation framework, and offers key insights into their wave energy control capabilities. The results form a theoretical basis for future design and experimental implementation of metamaterial-based wave-interacting structures.

Contents

1

Introduction

1.1. Research Context

As global attention shifts towards renewable energy development and climate resilience, the role of offshore structures has become increasingly prominent. Especially in Europe, where the European Commission (2020) has outlined a strategy to harness offshore renewable energy as part of its 2050 carbon-neutral goal. Meanwhile, coastal regions face growing pressure due to rising sea levels, climate change-driven extreme wave conditions (Lobeto et al., 2021), and the expanding need for clean energy and habitable space. In this context, the oceans are not only seen as a source of environmental risk but also as a potential platform for integrated solutions that combine energy production, coastal protection, and spatial expansion. Research on how to address these challenges and harness ocean energy to relieve the associated pressures represents a promising yet urgent direction for future exploration.

An increasingly explored and effective structural solution in this domain is the use of Very Large Floating Structures (VLFS). These are large-scale, flexible platforms floating on the sea surface, often spanning hundreds of meters. Due to their relatively low structural stiffness and the comparable wavelength of ocean waves, the response of VLFS is governed by a complex interplay of inertial, hydrodynamic, and elastic forces (Suzuki et al., 2006) - commonly referred to as hydroelasticity. This complex coupling requires accurate modeling to predict system behavior under wave loading and to ensure structural stability and performance.

VLFS have a wide range of applications in offshore and energy-related fields. Floating photovoltaic (FPV) platforms, for example, enable large-scale solar energy deployment in regions with limited land availability (Agnelli et al., 2023; Ramanan et al., 2024; Trapani et al., 2013). Floating infrastructure projects have been proposed to relieve pressure on land-based development. These include floating airport runways (Suzuki, 2005), offshore urban extensions such as floating cities (Takeuchi & Yoshida, 2022), and specialized facilities like floating sports fields and offshore oil storage platforms (C. M. Wang & Tay, 2011). Floating breakwaters serve as lightweight and low-environmental-impact wave barriers to protect coastal region or offshore structures (Cho & Kim, 1998; Dai et al., 2018). Figure 5.12b shows various applications of VLFS.

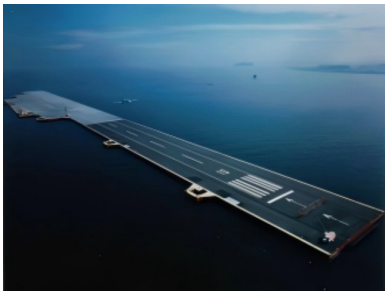

(a) floating airport runway

(b) floating photovoltaic

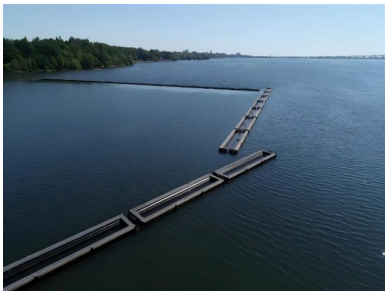

(c) floating breakwater

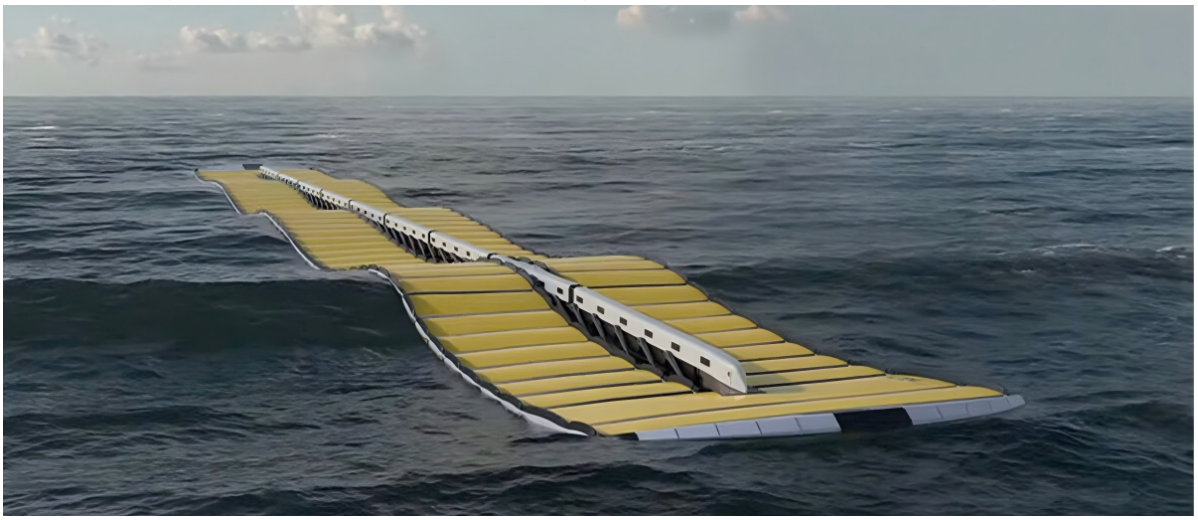

(d) wave energy converter

Figure 1.1: Applications of very large floating structures (VLFS)

In response to the need for multifunctional and adaptive floating systems, recent research has explored hybrid structures that integrate energy harvesting and wave attenuation within a unified design. One such approach is the use of modular wave energy converters (WECs) deployed at the front of a VLFS, as proposed by Cheng et al. (2022). These WECs are traditional point absorbers, typically consisting of a floating buoy connected to a seabed-mounted generator that extracts energy from their relative motion. Another way of harvesting wave energy is by transforming the wave-induced kinematic motion of the VLFS itself into storable energy (Michele et al., 2020). Recent research has demonstrated that employing piezoelectric materials allows the transformation of mechanical energy into electrical energy via the piezoelectric effect (Renzi et al., 2016).

1.2. Research Problem

VLFS as breakwaters hold great promise when integrated with wave energy conversion mechanisms. Compared to conventional point-absorber wave energy converters (WECs), floating membranes offer the potential to harvest wave energy across a broader range of frequencies. Their distributed and compliant nature enables more continuous energy extraction and may enhance overall efficiency in real sea states. A recent example of such an approach is the viscoelastic floating membrane proposed by Agarwal et al. (2024), which simultaneously acts as a wave absorber and a breakwater by dissipating incident wave energy through structural deformation.

While this membrane-based concept is elegant and lightweight, the same study also revealed its limita-

tions. Due to the inherent characteristics of viscoelastic membranes, their energy absorption capacity is generally stronger at higher frequencies, whereas performance at lower frequencies remains limited. Furthermore, when the excitation frequency aligns closely with the membrane's natural frequency, resonance occurs, resulting in almost complete wave transmission through the structure. In such scenarios, the membrane's capacity to act as an effective breakwater is significantly diminished. These frequency-selective limitations highlight a fundamental challenge in designing broadly effective membrane-based WECs.

A promising solution to this issue lies in the incorporation of Locally Resonant Metamaterials (LRMM). These consist of periodically distributed resonant units, typically mass-spring-damper systems, capable of inducing bandgaps through local resonance (Chang et al., 2018). Such structures can be tuned to attenuate specific low-frequency components, even when the overall wavelength is much larger than the feature scale of the resonators. By integrating LRMM into floating membranes, it may be possible to enhance energy absorption in the low-frequency range and suppress resonance-induced transmission.

Previous studies on LRMM have predominantly focused on their use in elastic solids or acoustic media, demonstrating remarkable capabilities in vibration isolation, energy trapping, and wave filtering (Pires et al., 2022). However, little work has been done to explore their behavior under a multi-physics hydroelastic environment. To better understand its effect and role under this scenario, it needs a systematic analysis of the system's dynamic characteristics. This gap motivates the current research. This task presents multiple challenges: the response of the system is highly sensitive to the properties and configuration of the resonators, and the three-way interaction between fluid, membrane, and resonator(s) requires careful numerical treatment to capture the coupled dynamics accurately.

1.3. Research Objectives

This research aims to systematically investigate how the coupling of locally resonant metamaterial (LRMM) affects the dynamic response of the floating membrane and its capacity to modulate or utilize wave energy, particularly in lower frequency regimes. Through modal analysis and systematic numerical simulations, the study explores their potential applications and the corresponding key design parameters for wave energy absorption or mitigation.

1.4. Research Scope

This thesis builds upon an existing finite element framework developed for hydroelastic floating membranes (Agarwal et al., 2024; Colomes, 2022), and does not aim to construct a new numerical model from scratch. The focus is instead placed on extending this model by incorporating locally resonant metamaterials (LRMM), and investigating the coupled dynamics through a series of numerical simulations.

The study adopts a fully numerical approach. The modeling framework is based on **linear wave theory** over a constant-depth water domain, and a **linearized** representation of LRMM modeled as mass–spring–dashpot systems. The structural domain is represented by a **one-dimensional pre-tensioned membrane**, while the fluid field is resolved over a **two-dimensional vertical slice**, assuming width-direction uniformity. These simplifications enable efficient parametric analysis while retaining the essential physics of wave–structure–resonator interaction.

The simulations are designed to provide insights into the dynamic response of the system, such as deformation modes, frequency-dependent behavior, and wave energy modulation effects. The model does not account for nonlinearity in fluid or structural responses. Instead, the aim is to understand the fundamental mechanisms and to lay a numerical foundation for future extension toward more realistic

and complex configurations.

1.5. Research Questions

From the previous information the main research question can be drawn:

> How does the coupling between *Locally Resonant Metamaterials* and *Hydroelastic Membrane* influence the *dynamic response* of the whole system and surrounding wave field, and how can this understanding guide the design for *wave energy absorption or attenuation devices*?

To address this question, the following sub-questions are defined:

1. What are the dry and wet natural frequencies and mode shapes of the coupled system, and how does LRMM influence and modify these?
2. What are the characteristic deformation patterns of the membrane and the surrounding wave field when subjected to different excitation frequencies?
3. How does the addition of LRMM modify the energy reflection, transmission and dissipation characteristics of the structure?
4. How do the key parameters of the resonators (frequency, position, damping ratio, mass ratio) affect the energy distribution (absorption, reflection, transmission) in the wave–structure system?
5. How does the LRMM-membrane system perform under a sea-state condition, and what does this imply for its potential application as a wave energy converter or a floating breakwater?

1.6. Thesis Structure

This thesis is structured into eight chapters, systematically addressing the research questions through numerical modeling, parametric study, and structural optimization.

- **Chapter 2 Literature Review:** Provides a critical analysis of existing research related to hydroelasticity, locally resonant metamaterials (LRMs), and their coupling effects. It also examines the numerical modeling techniques (FEA, CFD) and coupling strategies used in similar studies and identifies research gaps that justify this thesis.
- **Chapter 3 Numerical Formulation:** Introduces the governing equations of the coupled fluid–structure–resonator system, based on linear potential flow and membrane dynamics. It presents the monolithic finite element formulation used to solve the problem, along with the numerical implementation details, including coupling strategy, boundary conditions, and weak form in the frequency domain.
- **Chapter 4 Modal Analysis of the Coupled System with LRMM:** Present the discrete form of this problem and a novel methodology of wet modal analysis.
- **Chapter 5 Numerical results analysis:** Investigates the deformation patterns of the membrane and the surrounding wave field under various excitation frequencies. Both wet modal analysis and frequency-domain simulations are performed to analyze the influence of LRMM on the system's natural frequencies, mode shapes, and energy characteristics such as reflection, transmission, and absorption. It starts with one resonator without damping and goes to more complicated cases.
- **Chapter 6 Parametric studies of LRMM:** Conducts a systematic parametric study on key LRMM properties, such as resonance frequency, mass, and spatial position, to evaluate their influence on wave interaction performance and to identify favorable parameter ranges for wave attenuation or absorption.

- **Chapter 7 Application of the hydroelastic LRMM-membrane system:** This chapter investigates the performance of the LRMM-membrane system under a representative sea-state, aiming to bridge the gap between theoretical modeling and practical application. Using a scaled-down Jonswap spectrum as input, the system's response is analyzed in terms of wave force reduction and energy absorption. The results are used to evaluate its potential application as a multi-functional offshore structure, serving as both a breakwater and a wave energy converter, while highlighting how key resonator mechanisms contribute to desirable performance under realistic conditions.
- **Chapter 8: Conclusion and Suggestions:** Summarizes key findings, reflects on current approach and models, discusses limitations, and suggests directions for future research, such as multiple or non-linear resonators and model sensitivity study.

To clarify the relationship between the research questions and the thesis chapters, Table 1.1 outlines how each research question is addressed within the thesis structure.

Table 1.1: Mapping of Research Questions to Thesis Chapters

Research Questions	**Relevant Thesis Chapters**
RQ.1	Chapter 4, 5
RQ.2	Chapter 5
RQ.3	Chapter 5
RQ.4	Chapter 6
RQ.5	Chapter 7

2

Literature Review

This chapter reviews the theoretical and numerical foundations relevant to fluid-structure-resonator interaction in flexible floating membranes. It begins by introducing the concept of hydroelasticity, followed by a summary of two main methods, namely modal expansion and the direct method, together with representative applications. It then presents the principles and applications of LRMM, along with strategies used to model their dynamic behavior. Finally, it discusses numerical coupling schemes for fluid–structure–resonator systems, highlighting the advantages of monolithic formulations in strongly coupled settings.

2.1. Hydroelasticity and Hydroelastic Methods

Hydroelasticity describes the interaction between fluid forces and deformable structures, particularly in marine environments. Unlike rigid bodies, floating structures made of flexible materials undergo elastic deformations when subjected to waves. This requires a coupled analysis of hydrodynamics and structural mechanics. Bishop and Price (1979) first systematically studied the hydroelasticity of ships at an early stage, laying a theoretical foundation in this field. It is further contributed by Y. Wu (1984) for three-dimensional applications. These studies enabled early hydroelastic analysis of large floating structures modeled as beam (Georgiadis, 1981), as well as structures of arbitrary geometry (Price & Wu, 1985). To numerically analyze hydroelastic problems, two main methodological approaches have emerged, as summarized by Zhang and Schreier (2022): the mode expansion method and the direct method. These represent fundamentally different philosophies of coupling hydrodynamics with structural response.

In the mode expansion method, the structural motion is expressed as a combination of mode shapes and modal amplitudes, while the fluid field is solved independently, often through Green's integral formulation. The coupling is achieved by evaluating hydrodynamic forces caused by unit amplitude motion of each mode. This method has been extensively applied to beam and plate-type VLFS due to its computational efficiency and ease of implementation (Abul-Azm & Gesraha, 2000; D. Chen et al., 2022; Karmakar & Soares, 2012; Meylan, 2021). Although some of the studies use wet modes to evaluate structure motion (Loukogeorgaki et al., 2012), the dry-mode approach has been widely favored for its simplicity and orthogonality properties. However, its accuracy decreases for large or highly flexible structures, where many modes are needed to capture the dynamic response, and the hydrodynamic forces may be overestimated (Taylor, 2007).

In contrast, the direct method solves the coupled fluid–structure interaction equations directly, through various numerical schemes. This allows for greater accuracy in high-frequency or strongly coupled scenarios, but normally results in larger systems of unknowns and is time-consuming (Taylor, 2007). Early implementations used Green's function on the wet surface and finite element discretization to obtain

structural responses (Yago, 1997), but were often limited by computational cost. Improvements such as the analytical cover method proposed by Ohkusu and Nanba (1996) and the expansion-matching approach by Ertekin and Kim (1998) enhanced efficiency by reducing domain complexity and avoiding full wet-surface integration. Overall, while modal expansion offers efficiency and conceptual simplicity, the direct method provides higher accuracy and robustness in complex or strongly coupled systems.

2.2. Locally Resonant Metamaterials and its modeling

Locally resonant metamaterials (LRMM) are artificial structures designed to manipulate wave propagation by introducing subwavelength-scale resonating units into a host medium. These types of metamaterial have unusual physical properties such as negative effective mass (Liu et al., 2000). Unlike conventional scattering metamaterials, which rely on periodicity and structural scale comparable to the wavelength, LRMM achieve wave attenuation through local resonance, allowing them to operate effectively even at low frequencies (Cenedese et al., 2021).

The fundamental mechanism of LRMM lies in the formation of locally resonant bandgaps-these are frequency ranges in which wave propagation is inhibited. When a structure containing internal resonators is excited within such a range, the resonators oscillate out of phase with the surrounding medium, leading to destructive interference and strong wave attenuation. This mechanism is effective in elastic, acoustic, and mechanical wave systems, particularly in the low-frequency regime (Chang et al., 2018; Huang & Sun, 2009). The bandgap characteristics can be tuned by altering the mass, stiffness, and geometry of the resonating units, providing design flexibility for targeted wave control (Bigoni et al., 2013; Krushynska et al., 2014; Sugino et al., 2016).

Due to their frequency-selective attenuation characteristics, LRMM have been widely applied across different fields. In structural dynamics, they have been used to suppress vibrations and mitigate impact loads in beams, plates, and embedded components (He et al., 2023; Li et al., 2025). In acoustics, LRMM are employed in sound insulation and noise control by tailoring resonator configurations to create tunable acoustic bandgaps (Y. Chen et al., 2024). In the electromagnetic, LRMM are frequently employed to design frequency-selective resonators and filters. For instance, in the mid-infrared range, C. Wu et al. (2013) developed a silicon-based metasurface, enabling highly precise control over optical wave propagation. These applications demonstrate the versatility of locally resonant systems in passive wave control and energy localization.

LRMM are most commonly modeled using discrete mass–spring-dashpot systems, which capture the essential dynamics of internal resonators. The simplest and most widely used configuration is a single degree of freedom (SDOF) system, where each resonator is idealized as a lumped mass connected to the host structure via a linear spring and damper (Valappil & Aragón, 2025). This allows analytical or semi-analytical exploration of bandgap formation and parameter sensitivity. More complex representations involve connecting multiple lumped resonators, resulting in multi-degree of freedom (MDOF) systems (Chang et al., 2018; G. Wang et al., 2023). For example, two-stage resonators or nested structures can introduce additional bandgaps or broaden the frequency range of attenuation. Beyond that, nonlinear extensions of the basic model have also been proposed, where nonlinear stiffness or damping terms are introduced to account for amplitude-dependent behavior, large deformation, or hysteretic effects (Fang et al., 2018).

However, due to the limited availability of research on LRMM in fluid–structure interaction environments, particularly in the context of wave–membrane systems, we adopt the simplest form of modeling in this work. Each resonator is treated as a linear SDOF mass–spring–damper unit coupled to the membrane. This choice provides a clear baseline to assess the potential of LRMM in attenuating water wave energy through local resonance. More advanced models, such as nonlinear or distributed resonator systems, are seen as future studies.

In the context of floating hydroelastic systems, the integration of LRMM introduces additional challenges due to the presence of fluid–structure interaction. However, the same fundamental principles apply: resonators can be tuned to suppress wave-induced structural responses in selected frequency bands, potentially improving energy absorption and reducing transmitted wave energy.

2.3. Numerical Modeling strategies for FSI

Numerical strategies for modeling fluid–structure interaction (FSI) problems involve two key considerations: the strength of coupling (one-way or two-way coupling) and the solution strategy (partitioned or monolithic approach). A one-way coupling considers only the influence of one domain on another, while the reverse feedback is ignored. For instance, when analyzing the influence of waves on a structure, the feedback from the structure to the wave field, such as wave dispersion or scattering, is neglected. This simplification may be acceptable when the structure is small or rigid compared to the wavelength. However, for flexible systems such as floating membranes, two-way coupling becomes essential, as the structural deformation can significantly affect wave propagation, reflection, and energy dissipation.

Two-way coupling problems can be addressed using either a partitioned approach, which solves the fluid and structural domains separately and enforces compatibility through boundary exchange, or a monolithic approach, which formulates a single system of coupled equations. One example of the partitioned approach is given by Ioannou et al. (2025), where it addresses the non-linearity in the time domain. While partitioned methods allow the reuse of established solvers for each domain, they often suffer from stability and convergence issues, especially when the added mass effect is considered (Causin et al., 2005).

The monolithic approach, by contrast, treats the coupled dynamics in a unified framework and is well-suited for multi-physics systems involving strong fluid-structure interaction (Hübner et al., 2004). It can apply the compatibility conditions simultaneously by iteratively solving the coupled fluid and structural domains, updating until convergence is reached. In recent studies, monolithic finite element models have been successfully applied to simulate the wave interaction with floating flexible membranes under a multi-physics setup (Agarwal et al., 2024; Colomés et al., 2022). In particular, such formulations facilitate the computation of wet mode shapes and frequency responses, which are critical for understanding performance as WEC or floating breakwaters.

This modeling philosophy is also applicable to systems involving local resonators. The interaction between the fluid, membrane, and local resonant units forms a tightly coupled system that can benefit from the same monolithic treatment. The numerical framework developed in this study builds upon this approach to simulate the dynamic behavior of LRMM-based floating membranes under wave loading.

3

Numerical Formulation

This chapter establishes the governing equations and monolithic formulation for the coupled fluid–membrane–resonator system. Starting from linear potential flow theory and membrane dynamics, the equations are reformulated in the frequency domain to capture steady-state wave excitation. A monolithic variational framework is then developed to simultaneously represent the interactions among fluid, membrane, and LRMM. This unified formulation forms the basis for both modal analysis and frequency-domain simulations in subsequent chapters.

3.1. Problem setup

We consider a two-dimensional, inviscid, incompressible, and irrotational fluid domain Ω, bounded below by a rigid bottom Γ_b, and above by a fluid free-surface Γ_{fs} where the elevation is small compared to the wavelength and depth. The lateral boundaries are denoted by Γ_{in} and Γ_{out}, where incident and outgoing waves are respectively applied or absorbed using damping zones $\Omega_{d1,2}$. The fluid domain is described by the linear potential flow theory. Additionally, the fluid domain is coupled with a thin (one-dimensional) floating pre-tensioned membrane Γ_m. And we consider there is no air gap (cavitation) between Γ_m and Γ_{fs}. The floating membrane is anchored or free along portions of its lateral boundary Λ_m, as appropriate. The whole problem setup is shown in 3.1. Please note that nonlinearities arising from ocean wave dynamics and membrane deflection are neglected in the following analysis.

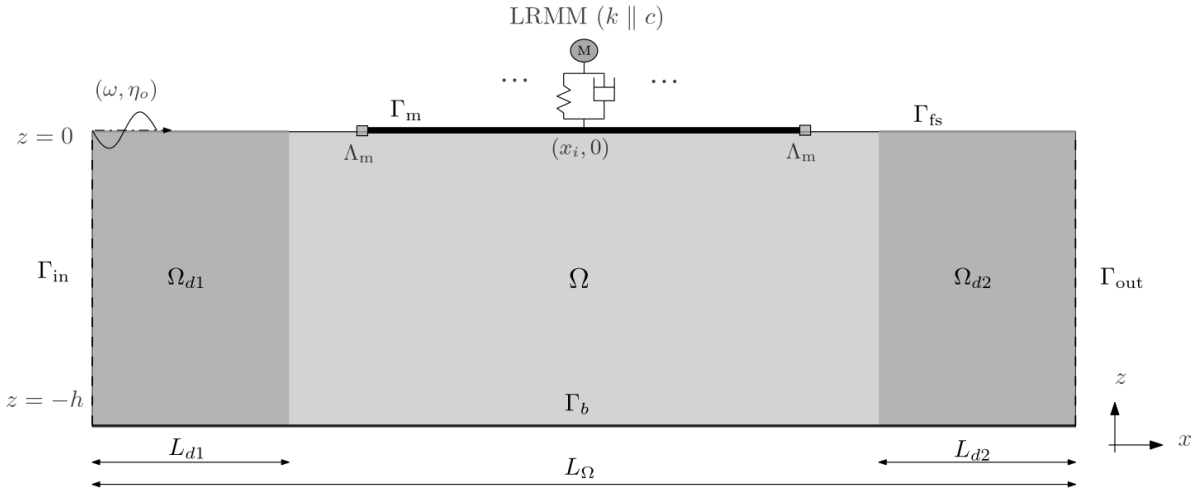

Figure 3.1: Problem setup of floating hydroelastic membrane coupled with locally resonant metamaterials

3.1.1. Linear potential flow theory

Let $\phi(\mathbf{x}, t)$ denote the velocity potential, such that the fluid velocity is $\mathbf{u} = \nabla\phi$. The governing equation for the potential flow is Laplace's equation:

$$\Delta\phi = 0 \quad \text{in } \Omega \tag{3.1}$$

In the following boundary conditions, $\mathbf{n}$ is the outward unit vector normal to domain boundaries. On the bottom boundary Γ_b, we impose a no-flow (Neumann) condition:

$$\mathbf{n} \cdot \nabla\phi = 0 \quad \text{on } \Gamma_b \tag{3.2}$$

At the fluid inlet Γ_{in} and outlet Γ_{out}, we impose:

$$\mathbf{n} \cdot \nabla\phi = u_{\text{in}} \quad \text{on } \Gamma_{\text{in}} \tag{3.3}$$
$$\mathbf{n} \cdot \nabla\phi = u_{\text{out}} \quad \text{on } \Gamma_{\text{out}} \tag{3.4}$$

On the free fluid surface Γ_{fs}, the standard linearized kinematic boundary conditions apply:

$$\mathbf{n} \cdot \nabla\phi = \frac{\partial\phi}{\partial z} = \kappa_t \quad \text{on } \Gamma_{\text{fs}} \tag{3.5}$$

where $\kappa(\mathbf{x}, t)$ is the free surface elevation.

The pressure at the free surface is given by linearized Bernoulli equation Eq. (3.6), at free surface the pressure is zero, thus leading to the linearized dynamic boundary conditions Eq. (3.7)

$$p = -\rho_w\phi_t - \rho_w g\kappa \tag{3.6}$$
$$\phi_t = -g\kappa \quad \text{on } \Gamma_{\text{fs}} \tag{3.7}$$

where ρ_w is the water density, and $g = 9.81$ m/s^2 is the gravitational acceleration.

3.1.2. Governing equation for viscoelastic membrane

In this paper we are studying pre-tensioned membranes, for thin structures, the pre-tensioning would dominate and the bending stiffness can be neglected. Detailed derivation and dimensional analysis is given by Agarwal et al. (2024). Thus, the dynamic equation for the viscoelastic membrane can be simplified to:

$$m\eta_{tt} - \nabla_h \cdot (T\nabla_h\eta) - \nabla_h \cdot (\tau T\nabla_h\eta_t) = f_{\text{ext}}, \qquad \text{where} \nabla_h = \frac{\partial}{\partial x}\,\hat{\mathbf{i}} + \frac{\partial}{\partial y}\,\hat{\mathbf{j}}. \tag{3.8}$$

where $\eta(\mathbf{x}, t)$ is the transverse deflection of the membrane, $m = \rho_m h_m$ is the membrane areal mass, T is the pretension, and τ is a constant damping parameter. The right-hand side f_{ext} represents external forcing due to various excitations.

The boundary conditions for membrane edges Λ_m are given as:

$$\nabla_h(\eta) \cdot \mathbf{n} = 0 \qquad \text{(free edge)} \tag{3.9}$$

In the following formulation derivation, the free edge boundary condition is used as default.

3.1.3. Governing equations of LRMM

To represent the effect of LRMM, we introduce a series of spring-mass-damper systems distributed over the membrane Γ_m. Each resonator is modeled by a lumped vertical degree-of-freedom $q(\mathbf{x}, t)$, defined over each membrane element (assumed piecewise constant), with mass m_r, damping c_r, and stiffness k_r.

The relative displacement between the resonator and the membrane causes a restoring and damping force, which is:

$$f_{\mathrm{r}}(\mathbf{x}, t) = c_r(\dot{q} - \dot{\eta}) + k_r(q - \eta) \quad \text{on } \Gamma_m \tag{3.10}$$

The governing equation of each resonator satisfies:

$$m_r\ddot{q} + c_r(\dot{q} - \dot{\eta}) + k_r(q - \eta) = 0 \quad \text{on } \Gamma_m \tag{3.11}$$

3.1.4. Coupling boundary conditions

On the membrane interface Γ_m, the kinematic free-surface condition is similarly:

$$\frac{\partial \phi}{\partial z} = \dot{\eta} \quad \text{on } \Gamma_m \tag{3.12}$$

The dynamic free-surface condition for Γ_m coupled with LRMM is derived by expanding the external excitation term on the right-hand side in Eq. (3.8). The external forcing contains two parts,The first contribution arises from the fluid–structure interaction, where the free-surface pressure term derived in Eq. (3.6) is applied on the right-hand side of the membrane equation. The second contribution originates from the restoring and damping force exerted by the resonators, corresponding to the reaction force in Eq. (3.10). By substituting these two terms into f_{ext} in Eq. (3.8) and divided by water density ρ_w on each side, the complete coupling boundary conditions at the membrane-fluid interface is finally obtained:

$$m_\rho \eta_{tt} - \nabla_h \cdot (T_\rho \nabla_h \eta) - \nabla_h \cdot (\tau T_\rho \nabla_h \eta_t) + \phi_t + g\eta = f_{\mathrm{r}}(\mathbf{x}, t)_\rho \quad \text{on } \Gamma_m \tag{3.13}$$

3.1.5. Frequency domain formulation

We assume all variables are time-harmonic with angular frequency ω:

$$\phi(\mathbf{x}, t) = \phi(\mathbf{x})e^{-i\omega t}, \quad \eta(\mathbf{x}, t) = \eta(\mathbf{x})e^{-i\omega t}, \quad q(\mathbf{x}, t) = q(\mathbf{x})e^{-i\omega t}, \quad \kappa(\mathbf{x}, t) = \kappa(\mathbf{x})e^{-i\omega t}$$

We consider N identical spring-mass-damper oscillators located at discrete points $\{\mathbf{x}_i\}_{i=1}^{N} \subset \Gamma_m$, each exerting a pointwise coupling force on the membrane via a Dirac delta function. The governing equations in the frequency domain are given as:

$$\Delta\phi = 0 \quad \text{in } \Omega \tag{3.14}$$

$$\frac{\partial\phi}{\partial z} + i\omega\kappa = 0 \quad \text{on } \Gamma_{\text{fs}} \tag{3.15}$$

$$-i\omega\phi + g\kappa = 0 \quad \text{on } \Gamma_{\text{fs}} \tag{3.16}$$

$$\frac{\partial\phi}{\partial z} + i\omega\eta = 0 \quad \text{on } \Gamma_m \tag{3.17}$$

$$\begin{aligned} &- m_\rho\omega^2\eta - i\omega\phi + g\eta - \nabla_h \cdot [T_\rho(1 - i\omega\tau)\nabla_h\eta] \\ &= \sum_{i=1}^{N}(-i\omega c_r + k_r)/\rho_w \cdot (q_i - \eta(\mathbf{x}))\,\delta(\mathbf{x} - \mathbf{x}_i) \quad \text{on } \Gamma_m \end{aligned} \tag{3.18}$$

$$(-m_r\omega^2 - i\omega c_r + k_r)/\rho_w \cdot q_i = (-i\omega c_r + k_r)/\rho_w \cdot \eta(\mathbf{x})\,\delta(\mathbf{x} - \mathbf{x}_i) \quad \text{for } i = 1, \ldots, N \quad \text{on } \Gamma_m \tag{3.19}$$

This completes the coupled frequency-domain model describing the interaction of waves, floating membranes, and distributed spring-mass oscillators.

3.2. Monolithic FEM formulation

3.2.1. Monolithic weak form

This problem is solved using a monolithic finite element formulation, following the method proposed by Colomes (2022), which is later extended to analyzing the dynamic response of visoelastic pre-tensioned floating membranes by Agarwal et al. (2024). In this research, we extended this formulation one step further by introducing the strong coupling of LRMM. Before proceeding to the weak form and discrete form of the problem, we first introduce some functional notation used throughout this work. Let $L^r(\Omega)$, with $1 \leq r < \infty$, denote the space of functions whose r^{th} power is absolutely integrable over the domain Ω. In our particular case where $r = 2$, this space becomes a Hilbert space equipped with the standard inner product:

$$(u, v)_\Omega \overset{\text{def}}{=} \int_\Omega u(\mathbf{x})\, v(\mathbf{x})\, d\Omega. \tag{3.20}$$

The space of functions whose distributional m^{th} order derivatives in $L^2(\Omega)$ are denoted by $H^m(\Omega)$. When $m = 1$, which is the situation widely occurred in the following equation derivation process, it is also a Hilbert space. The same notation as in Eq. 3.20 will also be used to take the integral of the product of two functions for both scalar and vector fields. Additionally, this integral notation is also applied on a given boundary of our interested domain, $\Gamma \subset \Omega$, written as:

$$(u, v)_\Gamma \overset{\text{def}}{=} \int_\Gamma u(\mathbf{x})\, v(\mathbf{x})\, d\Gamma. \tag{3.21}$$

We now describe the monolithic weak formulation of the coupled problem in the frequency domain. Let ω denote the angular frequency of interest, ϕ denote the velocity potential, κ denote the free-surface elevation, η denote the membrane deflection and q denote the displacement of the resonators. All field variables are assumed time-harmonic with time dependence $e^{-i\omega t}$. We define the complex-valued trial and test spaces as follows.

Let

$$[\phi, \kappa, \eta, q] \in \mathcal{V} \times \mathcal{V}_{\Gamma_{\text{fs}}} \times \mathcal{V}_{\Gamma_m} \times \mathcal{Q}$$

where:

- $\mathcal{V} := H^1(\Omega)$ is the fluid potential space,
- $\mathcal{V}_{\Gamma_{\text{fs}}} := \{v|_{\Gamma_{\text{fs}}} : v \in \mathcal{V}\}$ is the trace space on Γ_{fs} for κ,
- $\mathcal{V}_{\Gamma_m} := \{v|_{\Gamma_m} : v \in \mathcal{V}\}$ is the trace space on Γ_m for η,
- $\mathcal{Q} := \{q \in L^2(\Gamma_m) \mid q|_K \in \mathbb{C},\ \forall K \subset \Gamma_m\}$ is a piecewise constant function space for the oscillator field.

The associated test functions are in sequence denoted by $[w, u, v, \xi] \in \mathcal{V} \times \mathcal{V}_{\Gamma_{\text{fs}}} \times \mathcal{V}_{\Gamma_m} \times \mathcal{Q}$.

The monolithic weak formulation reads:

$$\text{Find } [\phi, \kappa, \eta, q] \in \mathcal{V} \times \mathcal{V}_{\Gamma_{\text{fs}}} \times \mathcal{V}_{\Gamma_m} \times \mathcal{Q} \text{ such that:} \tag{3.22}$$

$$B_\omega([\phi, \kappa, \eta, q], [w, u, v, \xi]) = L_\omega([w, u, v, \xi]) \qquad \forall [w, u, v, \xi] \in \mathcal{V} \times \mathcal{V}_{\Gamma_{\text{fs}}} \times \mathcal{V}_{\Gamma_m} \times \mathcal{Q} \tag{3.23}$$

The bilinear form B_ω consists of the following contributions:

$$\begin{aligned} B_\omega([\phi, \kappa, \eta, q], [w, u, v, \xi]) = {} & (\nabla\phi, \nabla w)_\Omega \\ & +(-i\omega\phi + g\kappa, \beta_h(u + \alpha_h w))_{\Gamma_{\text{fs}}} + (i\omega\kappa, w)_{\Gamma_{\text{fs}}} \\ & +(-m_\rho\omega^2\eta - i\omega\phi + g\eta, v)_{\Gamma_m} + (i\omega\eta, w)_{\Gamma_m} \\ & +(T_\rho(1 - i\omega\tau)\nabla\eta, \nabla v)_{\Gamma_m} \\ & -(T_\rho(1 - i\omega\tau)\nabla\eta \cdot \mathbf{n}, v)_{\Lambda_m} \\ & + \sum_{i=1}^{N} \left((-i\omega c_r + k_r)(q_i - \eta(\mathbf{x}_i))\right) / \rho_w \cdot v(\mathbf{x}_i) \\ & + \sum_{i=1}^{N} \left[(-m_r\omega^2 - i\omega c_r + k_r)q_i - (-i\omega c_r + k_r)\eta(\mathbf{x}_i)\right] / \rho_w \cdot \xi_i \end{aligned} \tag{3.24}$$

The right-hand side linear functional L_ω is given by:

$$L_\omega([w, u, v, \xi]) = (u_{\text{in}}, w)_{\Gamma_{\text{in}}} + (u_{\text{out}}, w)_{\Gamma_{\text{out}}} \tag{3.25}$$

For completeness and clarity, we now describe and outline the steps leading to the bilinear form. We first multiply the governing equation Eq. 3.14 with test function, w, integrate it over the domain Ω, and integrate by parts. The kinematic boundary conditions from Eq. 3.2 to Eq. 3.5 are then substituted to replace the normal velocity at boundaries. It results in the term in the first row, last term in the second and third row. For the dynamic boundary condition, it is incorporated by multiplying against a modified test function, $\beta_h(u + \alpha_h w)$, resulting in the first term in the second row. The modified test function is used to keep the free surface stabilize, see (Akkerman et al., 2020). The dynamic fluid-structure-resonator coupling conditions in Eq. 3.18 is multiplied against test function,v, and the high order terms are reduced also using integrate by parts, taking the free edge boundary conditions(Eq. 3.9). It results in the first term in the third row and all the terms form the 4^{th} to the 6^{th} row. Finally the last row is obtained by multiplying the governing equation of LRMM (Eq.3.19) with its test function ξ.

This monolithic formulation incorporates the fluid domain, free-surface dynamics, floating membrane, and distributed resonators in a unified variational framework. The coupling between membrane and resonator is captured via $q - \eta$ terms both in the membrane equation and the oscillator equation, ensuring energy-conserving interconnection.

3.2.2. Spatial discretization

The continuous weak formulation derived in Section 3.2.1 is discretized using finite-dimensional function spaces defined over a conforming triangulation of the computational domain. Let $\mathcal{T}_h$ denote the conforming mesh of the fluid domain Ω, with corresponding triangulations of the boundary subsets Γ_{fs}, Γ_m, and Γ_q, representing the free surface, membrane, and resonator locations, respectively.

We define the following finite-element spaces for the primary variables:

- $\mathcal{V}_h$ for the fluid potential ϕ, defined as a continuous Lagrangian space of polynomial degree $r \geq 1$:

$$\mathcal{V}_h := \left\{ w_h \in C^0(\Omega) \,\middle|\, w_h|_K \in \mathbb{P}_r(K),\ \forall K \in \mathcal{T}_h \right\},$$

  where $\mathbb{P}_r(K)$ denotes the space of polynomials of degree r on element K.

- $\mathcal{V}_{\text{fs},h}$ for the free-surface elevation κ, defined as the restriction of $\mathcal{V}_h$ to the free-surface boundary:

$$\mathcal{V}_{\text{fs},h} = \{ w_h|_E : w_h \in \mathcal{V}_h,\ \forall E \in \Gamma_{\text{fs},h} \}.$$

- $\mathcal{V}_{m,h}$ for the membrane displacement η, similarly defined on Γ_m:

$$\mathcal{V}_{m,h} = \{ w_h|_E : w_h \in \mathcal{V}_h,\ \forall E \in \Gamma_{m,h} \}.$$

- $\mathcal{Q}_h$ for the lumped resonator displacement q, defined as a piecewise constant space on the discrete resonator support Γ_q:

$$\mathcal{Q}_h = \left\{ q_h \in L^2(\Gamma_{m,h}) : q_h|_K \in \mathbb{C},\ \forall K \subset \Gamma_{m,h} \right\}.$$

The discrete trial and test function spaces are thus defined as:

$$\mathcal{X}_h := \mathcal{V}_h \times \mathcal{V}_{\text{fs},h} \times \mathcal{V}_{m,h} \times \mathcal{Q}_h, \qquad \mathcal{Y}_h := \mathcal{V}_h \times \mathcal{V}_{\text{fs},h} \times \mathcal{V}_{m,h} \times \mathcal{Q}_h.$$

The monolithic finite-element problem reads: Find $(\phi_h, \kappa_h, \eta_h, q_h) \in \mathcal{X}_h$ such that

$$B_\omega[(\phi_h, \kappa_h, \eta_h, q_h), (w_h, u_h, v_h, \xi_h)] = L_\omega[(w_h, u_h, v_h, \xi_h)], \quad \forall (w_h, u_h, v_h, \xi_h) \in \mathcal{Y}_h, \tag{3.26}$$

where the bilinear and linear forms are defined as in Eqs. (3.22)–(3.23), evaluated over the discrete mesh.

In practice, we use second-order Lagrange elements for $\mathcal{V}_h$, and assign Dirac delta function for $\mathcal{Q}_h$ to represent the pointwise coupling between the resonators and the membrane. The discrete system matrix is sparse, complex-valued, and assembled using the Gridap.jl finite element framework in Julia.

3.2.3. Wave generation and wave damping zone

In this study, waves are introduced into the numerical domain by prescribing the incoming velocity potential on the inflow boundary Γ_{in}, following Neumann boundary conditions derived from linear Airy wave theory. A damping layer of length L_d is implemented adjacent to this boundary to prevent reflection of incident waves, as schematically shown in Fig. 3.1

To prevent spurious reflections from the membrane back into the inlet domain, a specially designed *free-surface damping region* Ω_d is applied near the structure. Within this zone, we adopt a spatially varying artificial damping approach (applied on Γ_d) based on the so-called ϕ–η type formulation, similar to the Method 5 approach detailed in Kim et al. (2014). The damping is introduced via additional terms in the governing equations for ϕ_{in} and η_{in}, which gradually attenuate wave energy over the length of the damping zone. These terms are modulated using smooth spatial functions:

$$\mu_1 = \mu_0 \left(1 - \sin\left(\frac{\pi}{2} \cdot \frac{x - x_0}{L_d}\right)\right), \qquad \mu_2 = k\mu_1 \tag{3.27}$$

where x_0 denotes the location where damping begins, k is the wave-number, and μ_0 determines the maximum damping strength. This smooth distribution ensures gradual energy decay, minimizing artificial reflections. Additional implementation details can be found in Kim et al. (2014).

The prescribed quantities η_{in} and ϕ_{in} follow linear Airy wave theory. Two types of damping-modified free surface conditions are applied:

- Dynamic-Free Surface Condition (DFSC):

$$\frac{\partial \phi}{\partial t} = -g\kappa - \mu_1 \left(\frac{\partial \phi}{\partial t} - \frac{\partial \phi_{\text{in}}}{\partial n}\right) \tag{3.28}$$

- Kinematic-Free Surface Condition (KFSC):

$$\frac{\partial \eta}{\partial t} = \frac{\partial \phi}{\partial z} - \mu_2(\kappa - \kappa_{\text{in}}) \tag{3.29}$$

These expressions selectively damp wave components along the free surface, particularly those reflected from the floating membrane.

To simulate an open water environment, the Sommerfeld radiation boundary condition is applied on Γ_{out}. This condition allows waves to pass through the boundary without being reflected back, effectively creating a semi-infinite fluid domain. In the frequency domain, it is written as:

$$\nabla\phi \cdot \mathbf{n} = ik\phi \quad \text{on } \Gamma_{\text{out}} \tag{3.30}$$

This helps ensure that the outgoing waves leave the domain smoothly. An additional damping zone near Γ_{out} is only used in special cases when needed.

This combined approach of damping zones and non-reflecting boundary conditions has proven effective in eliminating spurious wave reflections and enabling stable simulation of both incident and scattered waves, even in mildly nonlinear and multidirectional scenarios (Kim et al., 2014).

4

Modal Analysis Approach of the Coupled System with LRMM

This chapter presents the methodology for performing modal analysis of the coupled fluid–structure–resonator system in the absence of damping. Starting from the system's governing equations, we formulate the eigenvalue problem to compute both dry and wet natural frequencies and the corresponding mode shapes. Particular attention is given to the iterative algorithm for both dry and wet modal analysis as the presence of the frequency (ω) dependent terms.

4.1. Dry modal analysis approach

Neglecting the interaction between the floating membrane and the surrounding fluid, we first consider the *dry modal characteristics* of the coupled system consisting of the membrane and the locally resonant spring–mass resonator (hereafter referred to as *resonator*). This analysis excludes all fluid interaction and focuses solely on the intrinsic structural modes of the membrane–resonator system. These dry modes serve as a reference for interpreting the added mass and stiffness contributions from the surrounding fluid, and offer insight into the underlying structural dynamics of the coupled system.

To derive the dry modal formulation, we begin by considering the membrane with resonator coupling, excluding the fluid potential ϕ and free-surface elevation κ. The governing equation is obtained by setting $\tau = 0$ and removing all fluid-related terms from the full weak formulation of the wet problem.

The resulting frequency-domain weak form reads as follows:

Find $\eta_h \in \mathcal{V}_{\Gamma_m}$, $q_h \in \mathbb{C}$, such that for all test functions $v_h \in \mathcal{V}_{\Gamma_m}$, $\xi_h \in \mathbb{C}$,

$$a((\eta_h, q_h), (v_h, \xi_h)) = 0$$

with the bilinear form defined as:

$$\begin{aligned} a((\eta_h, q_h), (v_h, \xi_h)) = {} & \underbrace{(T_\rho \nabla \eta_h, \nabla v_h)_{\Gamma_m}}_{K_{11}^d} - \omega^2 \underbrace{(m_\rho v_h, \eta_h)_{\Gamma_m}}_{M_{11}} \\ & + \underbrace{-(i\omega r_C - r_K)\, \delta(v_h \cdot \eta_h)}_{K_{11}^r} + \underbrace{(i\omega r_C - r_K)\, \delta(\xi_h \cdot v_h)}_{C_{14}} \\ & + \underbrace{-(i\omega r_C - r_K)\, \delta(v_h \cdot \xi_h)}_{C_{41}} + \underbrace{(r_K - i\omega r_C)\, \delta(\xi_h \cdot \xi_h)}_{K_{44}} - \omega^2 \underbrace{r_M \delta(\xi_h \cdot \xi_h)}_{M_{44}} \end{aligned}$$

This leads to the following 2×2 block eigenvalue problem:

$$\begin{bmatrix} K_{11}^d + K_{11}^r - \omega^2 M_{11} & C_{14} \\ C_{41} & K_{44} - \omega^2 M_{44} \end{bmatrix} \begin{bmatrix} \eta_p \\ q_p \end{bmatrix} = \begin{bmatrix} 0 \\ 0 \end{bmatrix} \tag{4.1}$$

Matrix definitions:

$$\begin{aligned} M_{11} &= (m_\rho v_h, v_h)_{\Gamma_m}, \\ K_{11}^d &= (T_\rho \nabla \eta_h, \nabla v_h)_{\Gamma_m}, \\ K_{11}^r &= -(i\omega r_C - r_K)\, \delta(\eta_h \cdot v_h), \\ K_{44} &= (r_K - i\omega r_C)\, \delta(\xi_h \cdot \xi_h), \\ M_{44} &= r_M\, \delta(\xi_h \cdot \xi_h), \\ C_{14} &= (i\omega r_C - r_K)\, \delta(\xi_h \cdot v_h), \\ C_{41} &= -(-i\omega r_C + r_K)\, \delta(v_h \cdot \xi_h) \end{aligned} \tag{4.2}$$

Here, $m_\rho = m/\rho_w$ and $T_\rho = T/\rho_w$ are the non-dimensionalized membrane mass and pre-tension parameters. The Dirac delta operator $\delta(\cdot)$ represents the evaluation of the fields at the resonator attachment location(s). This formulation captures the resonator-enhanced dry dynamics of the membrane, and can be used to compute its natural frequencies and mode shapes in the absence of fluid coupling. The structure of the eigenvalue problem mirrors that of the wet formulation, minus the contributions from the fluid DOFs ϕ and κ.

We further rewritten the block eigenvalue problem4.1as a system of two equations:

$$(K_{11}^d + K_{11}^r - \omega^2 M_{11})\boldsymbol{\eta}_h + C_{14}\boldsymbol{q}_p = 0 \tag{4.3}$$

$$C_{41}\boldsymbol{\eta}_h + (K_{44} - \omega^2 M_{44})\boldsymbol{q}_p = 0 \tag{4.4}$$

Assuming $(K_{44} - \omega^2 M_{44})$ is invertible, we solve Equation (4.4) for $\boldsymbol{q}_p$:

$$\boldsymbol{q}_p = -(K_{44} - \omega^2 M_{44})^{-1} C_{41}\boldsymbol{\eta}_h \tag{4.5}$$

Substituting (4.5) into (4.3) yields:

$$(K_{11}^d + K_{11}^r - \omega^2 M_{11})\boldsymbol{\eta}_h - C_{14}(K_{44} - \omega^2 M_{44})^{-1} C_{41}\boldsymbol{\eta}_h = 0 \tag{4.6}$$

We now define the frequency-dependent operator representing the influence of the resonator(oscillator):

$$\mathcal{R}_{\text{osc}}(\omega) = -C_{14}(K_{44} - \omega^2 M_{44})^{-1} C_{41} \tag{4.7}$$

This leads to the final eigenvalue problem:

$$\left[K_{11}^d + K_{11}^r + \mathcal{R}_{\text{osc}}(\omega)\right] \boldsymbol{\eta}_h = \omega^2 M_{11}\boldsymbol{\eta}_h \tag{4.8}$$

4.2. Wet modal analysis approach

In addition to the effects of the surrounding fluid, the presence of locally resonator alters the dynamic behavior of the membrane and modifies its natural modes. The modal analysis accounting for both fluid interaction and local resonator dynamics is thus referred to as the *wet modal analysis with resonator coupling*.

The weak form used for modal analysis is derived from the linearized frequency domain formulation (cf. Eq. (15)) by setting $\tau = 0$ and excluding all external forcing terms. This results in a strongly coupled eigenvalue problem involving the membrane displacement η, the fluid potential ϕ, the free-surface elevation κ, and the resonator displacement q.

The simplified weak form and its relationship with each element within the discretized eigenvalue matrix reads:

> Find $(\eta_h, \phi_h, \kappa_h, q_h) \in \mathcal{V}_{\Gamma_m} \times \mathcal{V}_\Omega \times \mathcal{V}_{\Gamma_{\text{fs}}} \times \mathbb{C}$, such that for all test functions $(v_h, w_h, u_h, \xi_h) \in \mathcal{V}_{\Gamma_m} \times \mathcal{V}_\Omega \times \mathcal{V}_{\Gamma_{\text{fs}}} \times \mathbb{C}$,
>
> $$a\big((\eta_h, \phi_h, \kappa_h, q_h),\ (v_h, w_h, u_h, \xi_h)\big) = 0$$

$$
\begin{aligned}
a\big((\eta_h, \phi_h, \kappa_h, q_h),\ (v_h, w_h, u_h, \xi_h)\big) = {} & \underbrace{(T_\rho \nabla \eta_h, \nabla v_h)_{\Gamma_m}}_{\text{membrane stiffness } K_{11}^d} + \underbrace{(g v_h, \eta_h)_{\Gamma_m}}_{K_{11}^w} - \omega^2 \underbrace{(m_\rho v_h, \eta_h)_{\Gamma_m}}_{M_{11}} \\
& + \underbrace{(g\kappa_h - i\omega\phi_h,\ u_h)_{\Gamma_{\text{fs}}} + i\omega(\kappa_h, v_h)_{\Gamma_{\text{fs}}}}_{\text{fluid–membrane coupling}} \\
& + \underbrace{-(i\omega r_C - r_K)\,\delta(v_h \cdot \eta_h)}_{K_{11}^r} + \underbrace{(i\omega r_C - r_K)\,\delta(\xi_h \cdot v_h)}_{C_{14}} \\
& + \underbrace{-(i\omega r_C - r_K)\,\delta(v_h \cdot \xi_h)}_{C_{41}} + \underbrace{(r_K - i\omega r_C)\,\delta(\xi_h \cdot \xi_h)}_{K_{44}} - \omega^2 \underbrace{r_M \delta(\xi_h \cdot \xi_h)}_{M_{44}} \\
& + \underbrace{(\nabla \phi_h, \nabla w_h)_\Omega}_{K_{22}} + \underbrace{-(i\omega w_h, \phi_h)_{\Gamma_{\text{in,out}}}}_{\text{radiation BC}} \\
& + \underbrace{(g\kappa_h - i\omega\phi_h, u_h)_{\Gamma_{\text{fs}}} + i\omega(\kappa_h, w_h)_{\Gamma_{\text{fs}}}}_{C_{23}, K_{33}} \\
& + \underbrace{(\kappa_h, u_h)_{\Gamma_m}}_{C_{32}}
\end{aligned}
$$

Discretization of the system using appropriate finite element spaces yields the following block matrix form:

$$
\begin{bmatrix}
K_{11}^d + K_{11}^w + K_{11}^r - \omega^2 M_{11} & -i\omega C_{12} & 0 & C_{14} \\
i\omega C_{21} & K_{22} & C_{23} & 0 \\
0 & C_{32} & K_{33} & 0 \\
C_{41} & 0 & 0 & K_{44} - \omega^2 M_{44}
\end{bmatrix}
\begin{bmatrix} \boldsymbol{\eta}_h \\ \boldsymbol{\phi}_h \\ \boldsymbol{\kappa}_h \\ \boldsymbol{q}_h \end{bmatrix}
=
\begin{bmatrix} F_\eta \\ F_\phi \\ F_\kappa \\ F_q \end{bmatrix}
\tag{4.9}
$$

The matrices are defined as follows:

$$
\begin{aligned}
M_{11} &= (m_\rho v_h, v_h)_{\Gamma_m}, & K_{11}^d &= (T_\rho \nabla v_h, \nabla v_h)_{\Gamma_m}, \\
K_{11}^w &= (g v_h, v_h)_{\Gamma_m}, & K_{11}^r &= -(i\omega r_C - r_K) \cdot \delta_p(v_h \cdot v_h), \\
C_{12} &= (w_h, v_h)_{\Gamma_m}, & C_{21} &= (v_h, w_h)_{\Gamma_m}, \\
K_{22} &= (\nabla w_h, \nabla w_h)_\Omega - (ikw_h, w_h)_{\Gamma_{\text{in,out}}}, & K_{33} &= (g u_h, u_h)_{\Gamma_{fs}}, \\
C_{23} &= (i\omega u_h, w_h)_{\Gamma_{fs}}, & C_{32} &= (-i\omega w_h, u_h)_{\Gamma_{fs}}, \\
M_{44} &= r_M \delta_p(\xi_h) \cdot \xi_h & K_{44} &= (r_K - i\omega r_C)\delta_p(\xi_h) \cdot \xi_h \\
C_{14} &= (i\omega r_C - r_K) \cdot \delta_p(\xi_h \cdot v_h), & C_{41} &= -(-i\omega r_C + r_K) \cdot \delta_p(v_h \cdot \xi_h)
\end{aligned}
\tag{4.10}
$$

To extract the wet modes of the membrane, the variables ϕ and κ are eliminated through static condensation. Following the approach in Agarwal et al. (2024), we define the frequency-dependent fluid response matrices as:

$$\mathcal{M}_\phi(\omega) = K_{22} - C_{23} K_{33}^{-1} C_{32}, \tag{4.11}$$

$$\mathcal{A}(\omega) = C_{12}\, \mathcal{M}_\phi^{-1}\, C_{21} \tag{4.12}$$

The resonator contribution is introduced through a dynamic stiffness term:

$$\mathcal{R}_{\text{osc}}(\omega) = -C_{14}\, (K_{44} - \omega^2 M_{44})^{-1} C_{41} \tag{4.13}$$

The final frequency-dependent eigenvalue problem is then written as:

$$[K_{11} + \mathcal{R}_{\text{osc}}(\omega)]\, \boldsymbol{\eta}_h = \omega^2 (M_{11} + \mathcal{A}(\omega)) \boldsymbol{\eta}_h \tag{4.14}$$

where,

$$K_{11} = K_{11}^d + K_{11}^w + K_{11}^r$$

This nonlinear eigenvalue problem is solved iteratively since both $\mathcal{A}$ and $\mathcal{R}_{\text{osc}}$ depend on the eigenfrequency ω. The iterative algorithm employed is illustrated in Figure 4.1. The resulting eigenfrequencies and mode shapes reflect the joint influence of fluid inertia, hydrostatic stiffness, and local resonator dynamics.

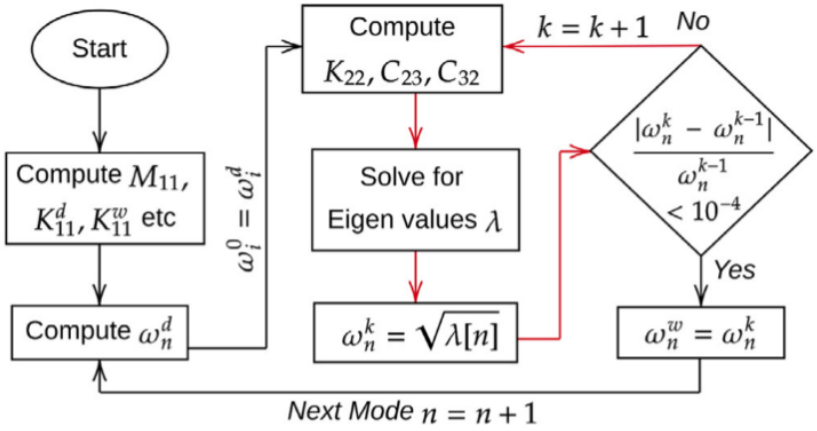

Figure 4.1: Iterative algorithm for determining the natural frequencies and mode shapes

5

Numerical Results

This chapter presents the numerical results obtained from the modal analysis and frequency-domain simulations of the coupled fluid–membrane–resonator system. The aim is to investigate the inherent dynamic characteristics of the system under selected configurations, and to highlight the role of LRMM in shaping the vibrational behaviour and energy interactions within the coupled fluid–structure domain.

The results are organized into two main parts. The first part focuses on modal analysis, beginning with the dry modes of the membrane-resonator system and followed by the wet modes obtained under fluid–structure interaction. Special attention is given to how the introduction of LRMM alters both the natural frequencies and associated mode shapes. The second part investigates the dynamic response of the system in the frequency domain under monochrome excitation, covering both undamped and damped configurations.

The numerical implementation of the finite-element formulation and associated solvers was carried out in the Julia programming language (Bezanson et al., 2017), using the Gridap finite element library (Badia & Verdugo, 2020). Gridap enables high-level implementation of weak form formulations in a syntax that closely mirrors mathematical notation (Verdugo & Badia, 2022), facilitating the development of accurate and maintainable code. Moreover, Gridap supports mixed-dimensional and mixed-order finite-element assembly, which is essential for the coupled formulation involving both fluid domains and membrane surfaces. These features make it well suited for the current study, where rapid prototyping and efficient simulation of multi-physics systems are required.

5.1. Modal analysis results

In this section, the iterative algorithm mentioned in Chapter. 4 are used for studying the natural frequencies and mode shapes for both dry and wet situations. The analysis is done for a finite size, materially undamped, hydroelastic 1D membrane coupled with one specific LRMM. To be specific, a 1000 (kg) local resonator with its frequency 2.4 (rad/s) and zero damping is coupled at the middle of the membrane. The length of the membrane is $L_m = 2h$, placed in 2D water domain with depth $h = 10$ (m), and length $L_\Omega = 3L_m$. The per-unit-area mass of the membrane is $0.9\rho g$, and the tension $T = 10\rho g$ We use this combination of the parameters as default when there is no explicit changes are mentioned. In Subsection 5.1.3 we vary the properties of LRMM to see its influence on the results.

Because the analysis is done for free vibration case, no generation of incoming waves is needed. Therefore, there are no damping zones in the water domain and the boundaries $\Gamma_{in}, \Gamma_{out}$ are set as radiation BC 3.30. Given the convergence analysis information from Agarwal et al. (2024) and the similarity of the simulation, we use the same element (rectangular elements with quadratic polynomial shape function) and mesh setup as in that paper.

5.1.1. Dry modal analysis

Dry natural frequencies and modes of the membrane only

We first introduce the dry membrane modes without LRMM as basic knowledge and a counterpart for our following results. For dry modal analysis without LRMM, the coupling of the water domain or LRMM is neglected, which simplifies this problem to an ordinary modal analysis case. There are several approaches to performing this dry model analysis, either numerically or analytically. To keep these results consistent and comparable with the following modal analysis results, we simply remove all the LRMM terms from equation 4.8, and perform the modal analysis numerically. Figure 5.1 illustrates the results.

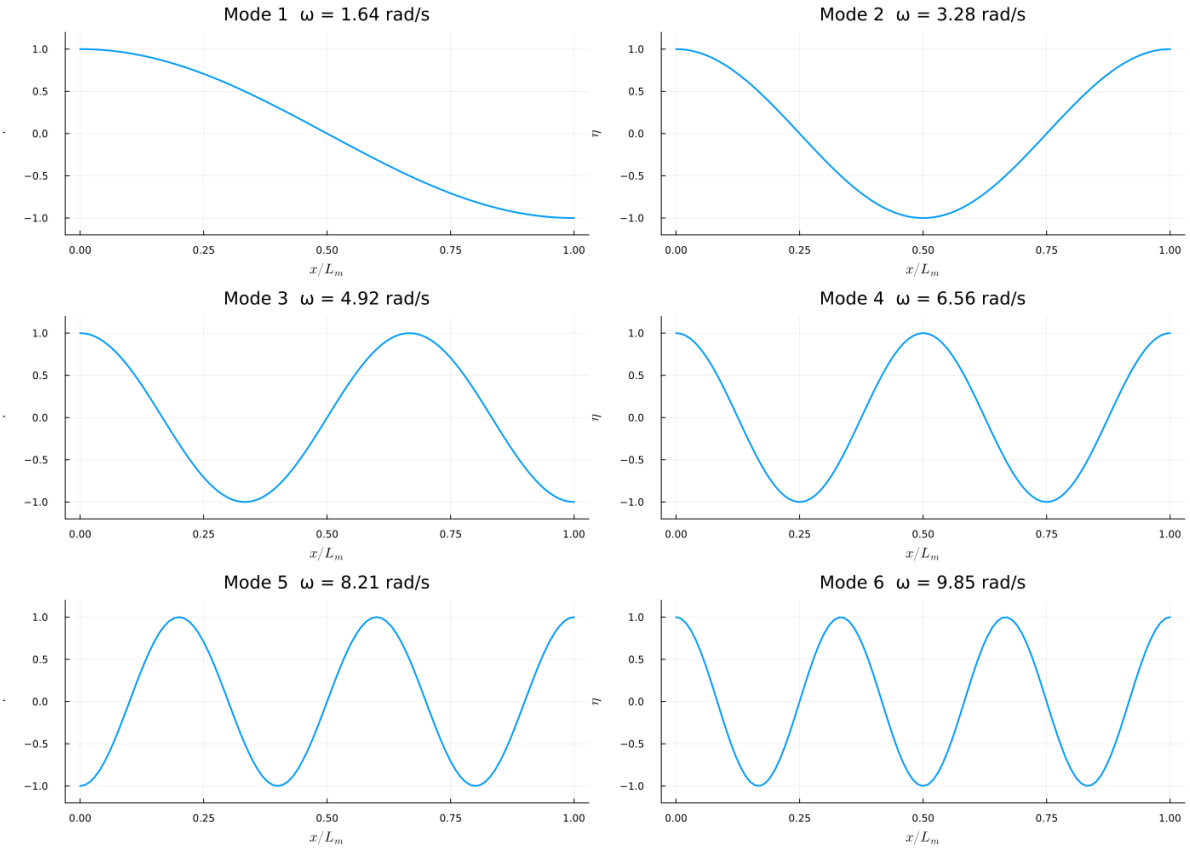

Figure 5.1: Dry natural frequencies and modes shape for membrane only

Dry natural frequencies and modes of the coupled system

We then proceed to the dry modal analysis of the system, including LRMM. The first six natural frequencies and modes are given in figure 5.2. The dry modal analysis of the coupled system reveals critical insights into how the inclusion of a point-attached spring–mass local resonator alters the vibrational behavior of the base membrane structure.

By comparing results from the dry membrane only and the coupled system, we observe the emergence of a new mode (mode 2 in figure 5.2) between the original Mode 1 and Mode 2 (in figure 5.1), resulting in a position shift in the modal sequence for higher modes. For example, the third mode in figure 5.2 is actually very similar to the second mode in figure 5.1, and the fourth mode for the coupled system is almost the same as the third mode of the counterpart.

Focusing on this new ”emerged” mode, it exhibits a natural frequency close to that of the resonator itself, and its modal shape is highly localized at the resonator location in contrast to the rest membrane dominated modes. The mode shape features a pronounced kink at the midpoint, indicating a strong modal participation of the resonator. This observation is consistent with the fundamental working principle of LRMM, where energy is locally trapped by the sub-wavelength resonator when excitation aligns with its natural frequency (Chang et al., 2018).

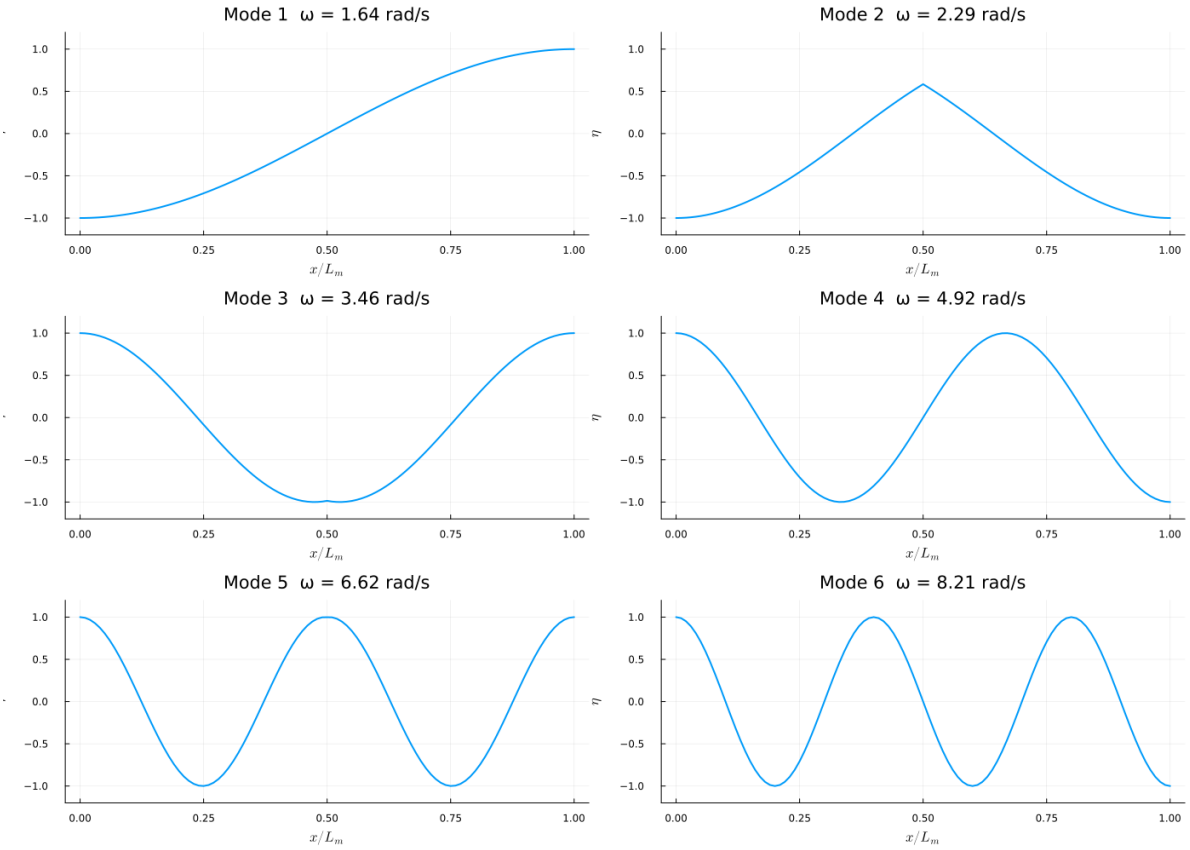

Figure 5.2: Dry natural frequencies and modes shape for membrane coupled with LRMM

Another important phenomenon is the occurrence of modes that remain nearly unaffected by the presence of the resonator. These are mode 1, 4, and 6. (Please also note that for wet mode i, $(i > 2)$, it should be compared with dry mode $i - 1$ as the emergence of the new mode.) These correspond to cases where the resonator is located at or near a nodal point of the mode shape. Since the displacement at the resonator location is negligible, the resonator is not significantly excited and does not contribute to the modal deformation, leading to negligible changes in both the natural frequency and mode shape.

For other modes such as mode 3 and 5, where the resonator is situated near an antinode, partial excitation occurs. In such cases, the interaction between the membrane and resonator causes a noticeable increase in the natural frequency, as the system stiffness effectively increases. Furthermore, the mode shapes are modified around the resonator location, where a sharp gradient or slope change can be observed. This local deformation feature, while continuous, indicates the presence of additional dynamic stiffness and mass contributed by the resonator.

These results confirm that the influence of LRMMs on structural dynamics is strongly mode-dependent, governed by the spatial location of the resonator relative to the modal pattern, and can either dominate,

modify, or have negligible impact on specific modes

5.1.2. Wet modal analysis

Wet natural frequencies and mode shapes of the coupled system

Figure 5.3a shows the wet natural frequencies and modes for the same setup as used in dry modal analysis. To compare between dry and wet situations, figure 5.3b visualizes the differences. The units for all the natural frequencies shown in these figures are rad/s

The results clearly demonstrate the impact of fluid–structure interaction on the membrane's dynamic properties. Across all modes, the wet natural frequencies are consistently lower than the dry ones. This frequency reduction is attributed to the *added mass effect* introduced by the surrounding fluid (demonstrated in equation 4.12), which increases the system's effective inertia and thereby reduces its natural frequencies.

In terms of mode shapes, the wet modes tend to be smoother and exhibit less spatial curvature compared to the dry cases. This is again due to the distributed influence of fluid loading, which suppresses high spatial gradients in the structural response.

Rather interestingly, a notable exception occurs at Mode 2, where the wet mode shape is more peaked than its dry counterpart, exhibiting a local amplification near the resonator region. This phenomenon can be attributed to the different influence of added fluid mass depending on the dominant component of the mode. Specifically, Mode 2 is resonator-dominated, in contrast to all other membrane-dominated modes. In this case, the resonator undergoes strong resonance and exhibits large local deformation. Since the LRMM itself is not significantly affected by fluid loading, its motion remains relatively unaffected. However, it drives the adjacent membrane into motion, where the fluid's added mass effect becomes significant. Compared to the dry case, the membrane's local response in the wet configuration is suppressed due to the increased effective mass, resulting in a sharper peak at the resonator while the surrounding deformation is dampened. This leads to the conclusion that for resonator-dominated modes, the wet mode shape becomes more peaked than the dry counterpart, while for the membrane-dominated modes, the wet mode shapes are consistently smoother due to the distributed added mass of the surrounding fluid.

These observations underscore the importance of including both fluid loading and resonator dynamics in modal analyses, as they jointly determine the system's vibrational characteristics.

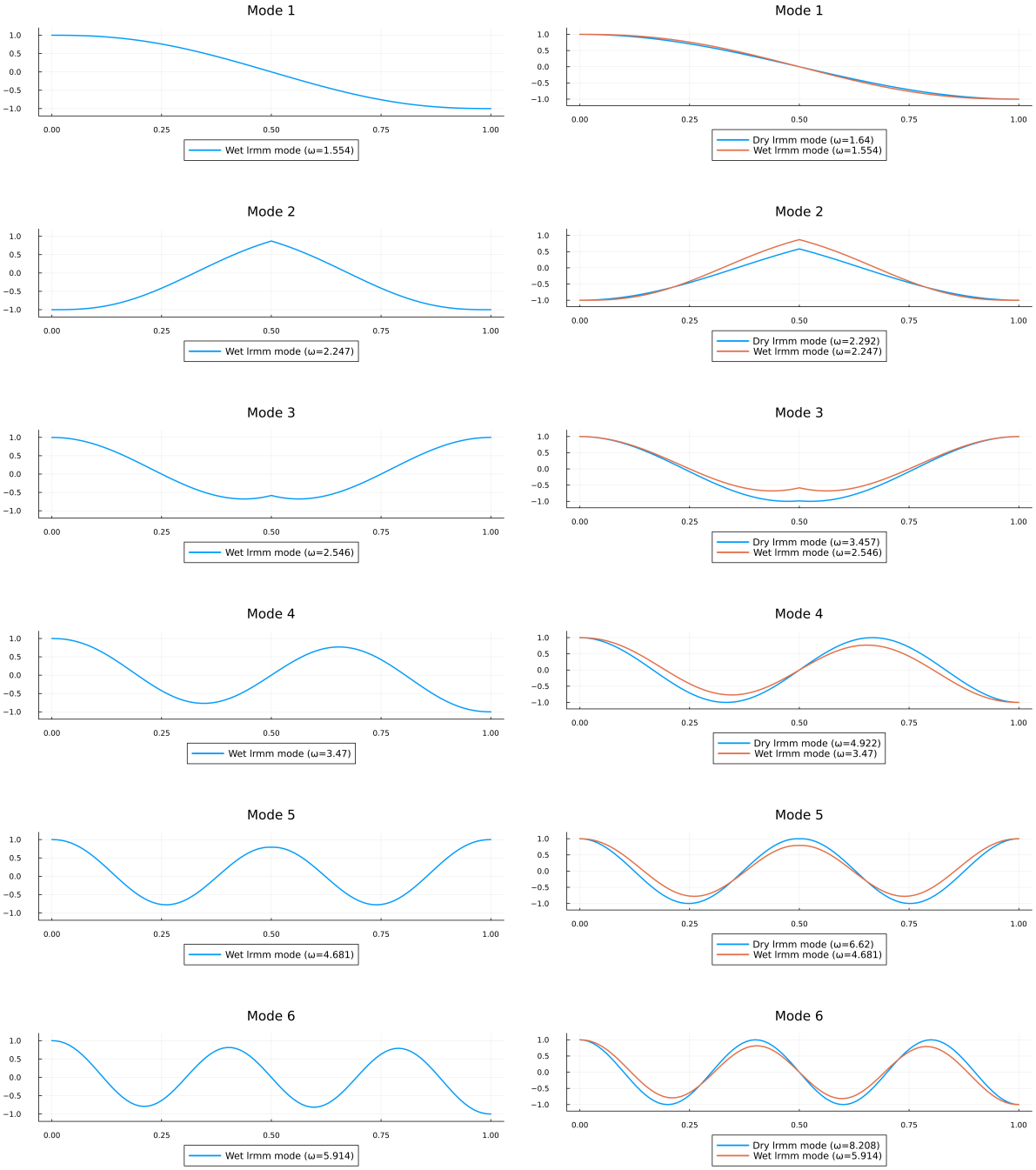

(a) Wet natural frequencies and modes

(b) Comparison between dry and wet modes

Figure 5.3: Wet natural frequencies and modes and comparison with dry modal results. ($r_M = 1000\ kg,\ r_\omega = 2.4\ rad/s$)

5.1.3. Influence of LRMM on wet natural frequencies and modes

In this section, we aim to investigate how different parameters of the LRMM influence the results of the wet modal analysis. We begin by examining the effect of the resonator's eigen frequency on the natural frequencies of the coupled system. This is followed by an analysis of its influence on the associated mode shapes, with particular attention given to the "newly emerged mode" introduced by the presence of the resonator. Lastly, we explore how variations in the resonator mass affect the spatial characteristics of the mode shapes.

Influence of r_ω on natural frequencies

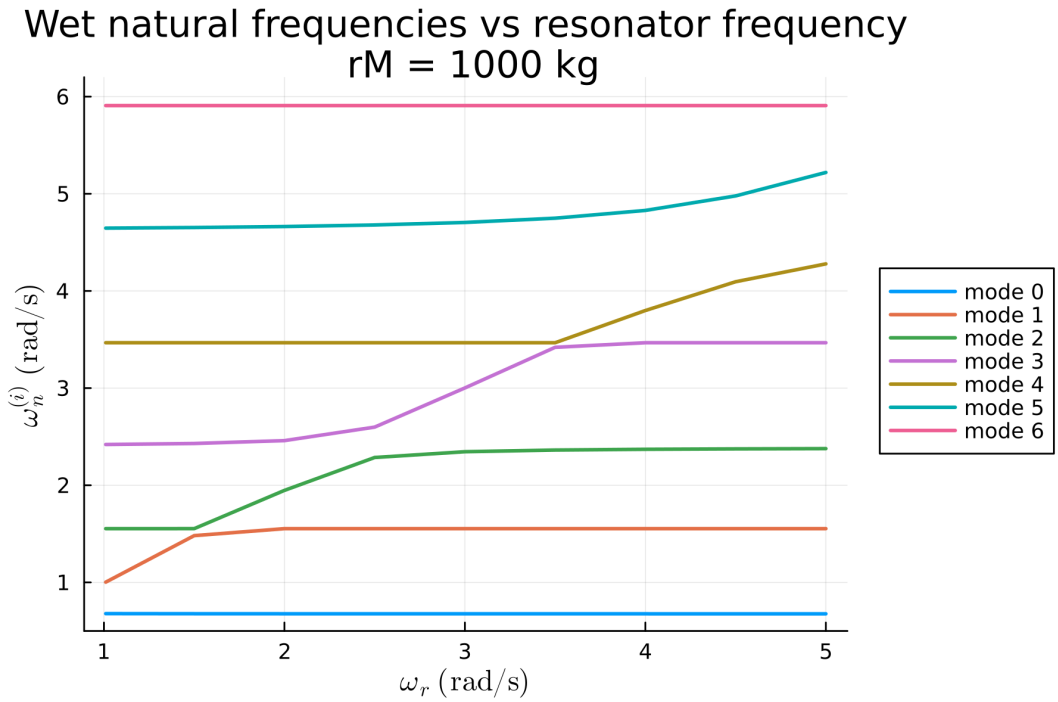

Figure 5.4: influence of LRMM's eigenfrequencies on natural frequencies of the system

To investigate how the eigen frequency of the local resonator influences the natural frequencies of the coupled system, a frequency sweep was performed. The mass of the resonator, r_M, and other system parameters were kept constant, while the eigenfrequency of the resonator, r_ω, was varied from 1 to 5 rad/s. For each value of r_ω, the wet modal analysis was conducted and the first six elastic natural frequencies were recorded. The results are presented in Figure 5.4, where the horizontal axis corresponds to the resonator frequency and the vertical axis denotes the natural frequencies $\omega^{(i)}$ of the system.

The first mode ($i = 0$) corresponds to a rigid-body translational mode and is thus excluded from the analysis. In the absence of LRMM coupling, the natural frequencies of the membrane structure would remain constant, producing flat horizontal lines in the figure. However, due to the introduction of the local resonators, the resulting curves exhibit more complex behavior.

One of the most notable features in the figure is the emergence of a set of diagonally rising lines. These curves represent the resonance frequencies that are strongly influenced—or even generated—by the resonator itself. We refer to these as *LRMM-dominant modes*, as they arise when the system's excitation frequency approaches the eigenfrequency of the resonator. In these cases, the resonator

is significantly excited and induces vibrations in the membrane that would not otherwise occur in its absence. As a result, new vibrational modes appear that do not align with the membrane's intrinsic modal structure.

In contrast, the remaining modes—those appearing as nearly flat lines—are only mildly perturbed by the resonator. These can be viewed as *membrane-dominant modes*, where the LRMM plays a secondary role. While the presence of the resonator may slightly shift the natural frequencies or locally alter the mode shapes, it does not fundamentally change the character of the vibration.

This result clearly demonstrates the frequency-selective nature of the LRMM and highlights its ability to inject new modal content into the system when its eigenfrequency aligns with the system's resonance band. Such behavior is central to the LRMM's functionality and underscores its potential for targeted wave manipulation and vibration control.

Influence of r_ω on modes

In our earlier analysis of the dry modal behavior in Section 5.1.1, we observed that the introduction of a local resonator effectively inserted an additional mode into the spectrum. This mode appeared between the original first and second modes of the membrane-only system, resulting in an apparent shift of subsequent modes. This observation suggested the emergence of a new mode predominantly influenced by the dynamics of the resonator itself, often referred to as a resonator-dominant mode.

Here, we extend it by performing a systematic investigation of how this behavior varies with the resonator's eigen frequency r_ω. To this end, we fix the resonator mass at $r_M = 1000\ kg$, and vary r_ω across values of $1.0, 3.0,$ and $5.0\ rad/s$. For each case, we compute the wet modes of the coupled system.

As shown in Figure 5.5, a clear pattern emerges: in each configuration, a new mode arises whose natural frequency closely follows the value of r_ω compared with the membrane only case, that is mode 1 in Figure 5.5a, mode 3 in Figure 5.5b), and mode 5 in Figure 5.5c. And these modal shapes' profile exhibits a sharp kink at the resonator location. This behavior is a strong indicator that the mode is dominated by the motion of the resonator. Notably, the presence of this resonator-driven mode leads to a rearrangement of the membrane-dominant modes, effectively shifting them upward in the mode sequence, in a manner consistent with what was previously observed in the dry modal case.

This finding directly supports and further explains the diagonal "resonator line" observed in Figure 5.4. Each point along this diagonal corresponds to one of these resonator-dominant modes, whose frequencies track closely with the resonator's eigen frequency.

To further confirm this interpretation, we extract the eigenvalue associated with the resonator variable q from the coupled system's EVP for each mode. This value serves as an indicator for the modal participation of the resonator: higher magnitudes indicate a greater contribution of the resonator to the mode shape. As shown in Figure 5.6, the highest modal participation for these three cases is mode 1,3,5 separately. These resonator-dominant modes are associated with significantly larger resonator eigenvalues compared to the other modes, reinforcing the conclusion that these are indeed primarily governed by the resonator dynamics. However, for the $r\omega = 5.0\ rad/s$ case, the fourth wet natural frequency is also close to the eigen frequency of the LRMM. We can see from Figure 5.6c that the LRMM is also largely excited, thus resulting in a localized kink at the middle of the structure at mode 4 in Figure 5.5c

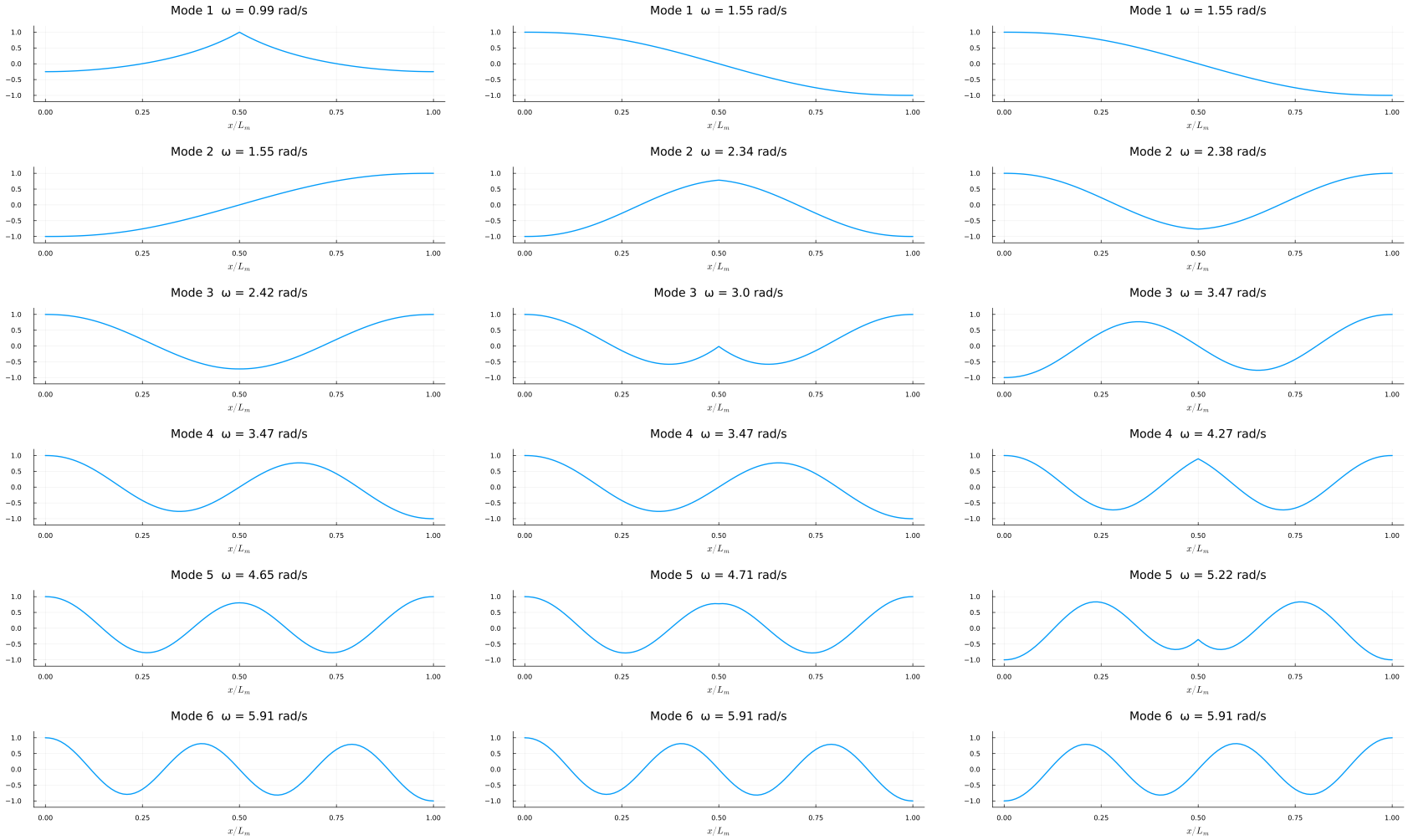

(a) wet mode shapes for $r_\omega = 1.0\ rad/s$

(b) wet mode shapes for $r_\omega = 3.0\ rad/s$

(c) wet mode shapes for $r_\omega = 5.0\ rad/s$

Figure 5.5: Wet mode shapes for $r_\omega = 1.0,\ 3.0,\ 5.0\ rad/s$

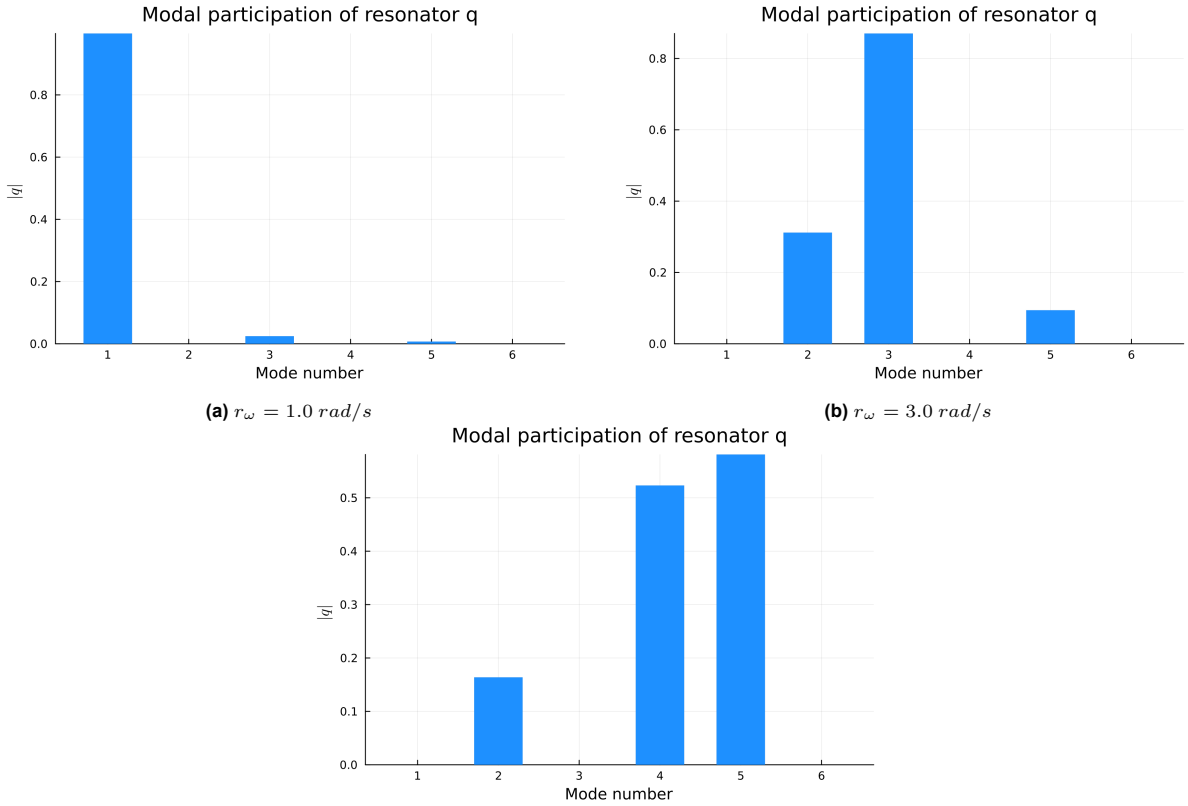

(a) $r_\omega = 1.0\ rad/s$

(b) $r_\omega = 3.0\ rad/s$

(c) $r_\omega = 5.0\ rad/s$

Figure 5.6: normalized eigenvalues associated with the resonator variable (q_h) from the system's EVP for each mode, for $r_\omega = [1.0,\ 3.0,\ 5.0]\ rad/s$

Influence of r_M on modes

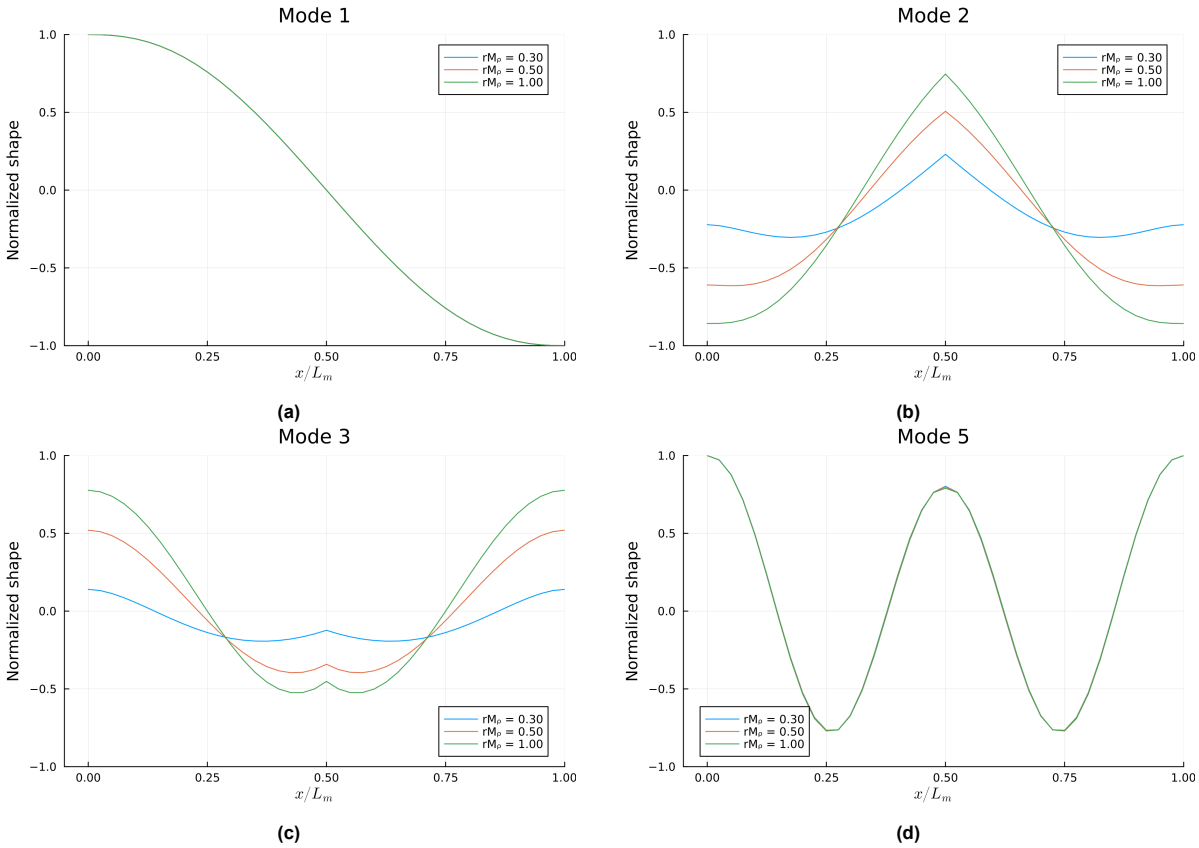

Figure 5.7: Selected mode shapes for for $r_{M_\rho} = 0.3,\ 0.5,\ 1.0$ under $r_\omega = 2.4\ rad/s$situation

To assess how the mass of the resonator influences the system's vibrational characteristics, we conduct a parametric study where the dimensionless resonator mass ratio $r_{M_\rho} = r_M/\rho_w$ is varied while keeping its eigen frequency fixed at $r_\omega = 2.4\ rad/s$ and positioned at the middle of the membrane. Figure 5.7 presents selected mode shapes for $r_{M_\rho} = 0.3$, 0.5, and 1.0.

The results demonstrate that the impact of the resonator mass depends significantly on its location relative to the membrane mode shapes. When the resonator is positioned at or near a nodal point of a given mode, its influence is negligible. For instance, Mode 1 shows no visible difference in shape for different values of r_M, indicating the resonator is effectively inactive for this mode.

In contrast, for modes where the resonator is situated away from nodes, its influence becomes evident. This effect is obvious in Modes 2 and 3, where increasing the mass ratio results in sharper peaks around the resonator location. This amplification is a consequence of the resonator contributing more to the overall dynamic response, which is consistent with the trends observed in the modal participation part.

Finally, for higher-order modes such as Mode 5, even though the resonator may be located away from a node, its influence becomes minimal if the mode's natural frequency is far from the resonator's eigenfrequency. In such cases, the dynamic coupling is weak, and changes in r_M do not significantly alter the modal shape.

5.2. Frequency domain dynamic response

After completing the modal analysis, we proceed to examine the steady-state dynamic response of the system under monochromatic wave excitation. All simulations in this section are conducted in the frequency domain, where the system is subjected to progressive incident waves generated using linear wave theory. The incoming wave field is prescribed with a target amplitude $|\kappa_{\text{in}}| = \kappa_0$, and a wave frequency ω ensuring a consistent wave input in all simulations. The primary goal is to assess how the structure reflects, transmits, and absorbs wave energy under various configurations, both with and without material damping.

The computational setup consists of a 1D membrane structure coupled with one LRMM at its middle, floating in a 2D rectangular fluid domain of uniform depth h ($h = 10\ m$). The length of the membrane is L_m, occupying the region between $x \in [4L_m, 5L_m]$. To suppress unwanted reflections at the domain boundaries, wave-absorbing regions are introduced. A damping zone of length $L_d = 7.5L_m$ is placed upstream of the membrane at $x \in [-7.5L_m, 0]$ to absorb waves reflected by the structure. On the downstream side, a radiation boundary condition is applied (eq. 3.30). No additional damping zone is included near the outlet. The chosen properties of the LRMM and the membrane are fixed and consistent with the default setup used in the modal analysis unless otherwise specified.

The fluid domain is discretized using second-order quadrilateral elements. A uniform mesh spacing of $\Delta x = 0.01L_m$ is used horizontally, while in the vertical direction, the grid is gradually refined near the free surface—ranging from $\Delta z = 0.0054h$ at the top to $\Delta z = 0.17h$ at the bottom—to accurately capture surface wave behavior. This meshing strategy ensures adequate resolution of both fluid and structural responses. The simulations are executed frequency by frequency, with a typical run time of about 4.5 seconds per case on a standard desktop computer.

Let κ_{in}, κ_r, and κ_t denote the complex-valued wave amplitudes associated with the incident, reflected, and transmitted waves, respectively. These quantities vary spatially and are extracted from the numerical solution using probe data. One upstream probe at $x = 2.75L_m$ is used to gather data from incoming and reflected waves, and the downstream probe is set symmetrically at $x = 6.25L_m$, measuring the transmitted wave amplitude. The extracted complex wave amplitudes are then used to compute the reflection $K_r = \frac{P_R}{P_{in}}$, transmission $K_t = \frac{P_T}{P_{in}}$, and absorption $K_a = \frac{P_A}{P_{in}}$ coefficients, based on the corresponding power fluxes:

$$P_{in} = \frac{1}{2}\rho g|\kappa_{\text{in}}|^2 C_g, \tag{5.1}$$

$$P_R = \frac{1}{2}\rho g|\kappa_r|^2 C_g, \tag{5.2}$$

$$P_T = \frac{1}{2}\rho g|\kappa_t|^2 C_g, \tag{5.3}$$

$$\text{where} \quad C_g = \frac{1}{2}\left(\frac{\omega}{k}\right)\left(1 + \frac{2kh}{\sinh(2kh)}\right) \tag{5.4}$$

C_g is the group velocity of the wave. In simulations involving structural damping, the absorbed power P_A is taken into consideration with two contributions - one from the membrane and one from the local resonator. The averaged absorbed power per unit length of the membrane over one wave period ${P_A}^{mem}$ is defined by taking the first derivative of the system's total energy to time (Agarwal et al., 2024). It is described in equation 5.5. And the averaged absorbed wave energy by the local resonator over one wave period is given in equation 5.6:

$${P_A}^{mem} = \frac{1}{t_{\text{wave}}}\int_t^{t+t_{\text{wave}}}\left(\int_{\Gamma_m} p_{\text{diss,struc}}\, d\Gamma_m\right) dt = \frac{1}{2}\rho T_0 \omega^2 \int_{\Gamma_m} |\nabla\eta|^2\, d\Gamma_m. \tag{5.5}$$

$${P_A}^{lrmm} = \frac{1}{2} r_C \omega^2 \left|q - \kappa\right|^2 \tag{5.6}$$

These energy terms will serve as the basis for the analysis in the following sections. To further visualize and study the system's ability to control or attenuate wave energy. We set the reflection wave energy coefficient as $K_r = \frac{P_R}{P_{in}}$, transmitted wave energy coefficient as $K_t = \frac{P_T}{P_{in}}$, and absorbed wave energy coefficient as $K_a = \frac{P_A}{P_{in}}$.

5.2.1. Without damping

To establish a baseline for comparison, we first examine the dynamic response of the membrane-only configuration without any attached resonators. This provides a reference case to assess the additional effects introduced by the LRMM system. We consider a membrane of length $L_m = 2h$, tension parameter $T_\rho/gL_m^2 = 0.025$, no material damping ($\tau = 0$), and non-dimensional mass $m_\rho/L_m = 0.045$, floating in still water of constant depth $h = 10$ m. Free-edge boundary conditions are applied at both ends of the membrane. These parameter settings are consistent with those used in the previous modal analysis. The frequency-domain simulations are carried out under the same numerical framework as introduced in Section 3.2. The first few wet natural frequencies of this membrane are computed as

$$\omega_{mem}^{w} = \{1.553,\ 2.413,\ 3.467,\ 4.642\}\ \text{rad/s},$$

which will serve as useful reference points when interpreting resonance behavior in the upcoming LRMM-coupled cases.

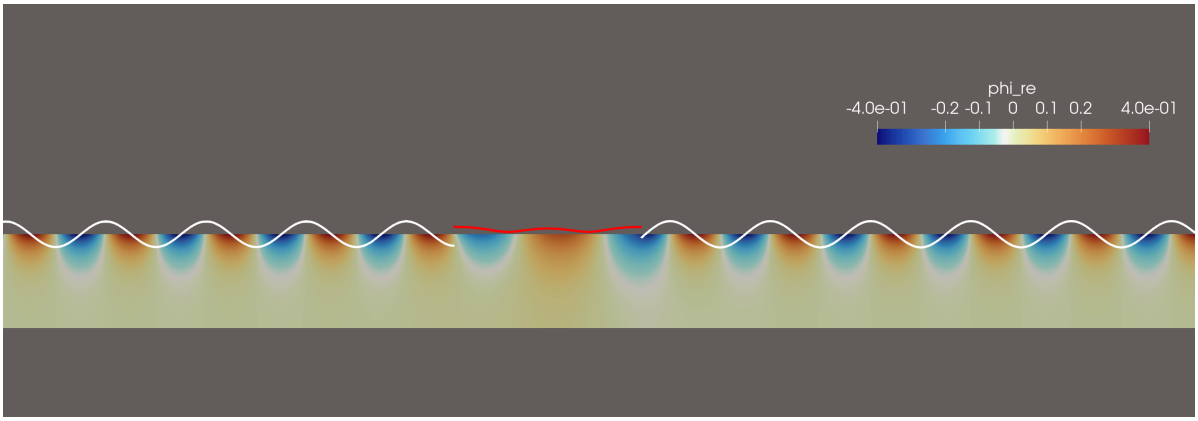

(a) dynamic response of membrane only configuration and vicinity water domain solution

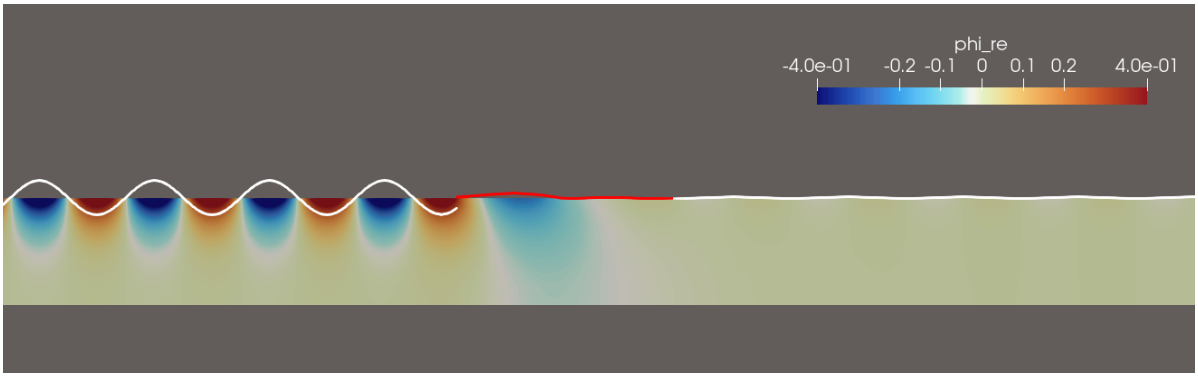

(b) dynamic response of coupled system and vicinity water domain solution

Figure 5.8: Numerical simulation results of ϕ in the vicinity of the structure and exaggerated plots of surface elevation κ and structure deformation η

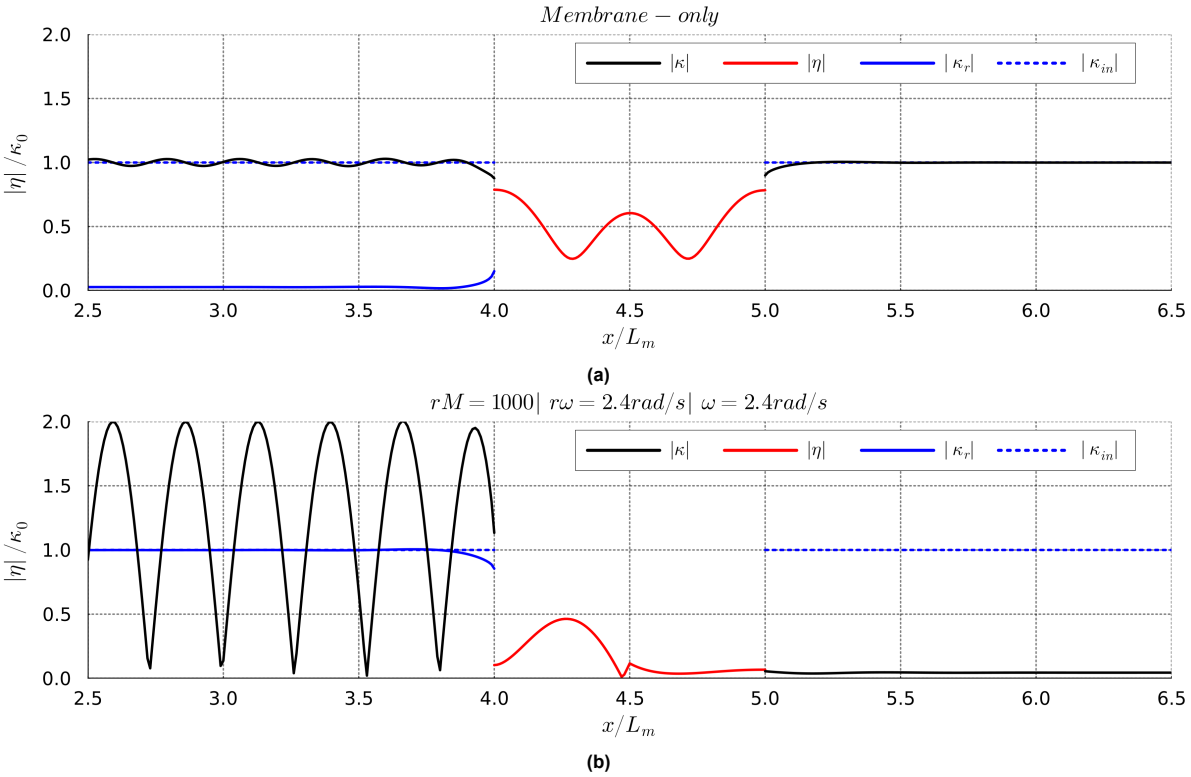

Figure 5.9: Plots of amplitude of structure deflectionη, incoming wave $\kappa_i n$, reflected wave κ_r, transmitted wave κ_t, and total free-surface elevation. (a)membrane-only, (b)coupled system

The next step is to examine the dynamic response of the system with LRMM in the absence of material damping, with $\tau = 0$ and $r_C = 0$. And the eigen natural frequency of the LRMM is $r\omega = 2.4$. The results are presented in Fig. 5.8, which compares the wave–structure interaction behaviour under two configurations: (a) a membrane-only system, and (b) a membrane coupled with a resonator tuned to match the excitation frequency. In both cases, the incoming regular wave has a frequency of $\omega = 2.4$ rad/s, which coincides with the local resonator's frequency $r\omega$ and is close to the second natural frequency of the membrane-only configuration. The amplitude of the solution for surface elevation κ near the membrane, along with the membrane deflection η, is illustrated in Fig. 5.9. In this plot, the upstream κ field is decomposed into the incoming wave κ_{in} and the reflected component $\kappa_{\text{r}} = \kappa - \kappa_{\text{in}}$, while the downstream solution corresponds to the transmitted wave κ_{t}.

As shown in figure 5.8a, the excitation of the membrane near resonance leads to almost complete transmission of wave energy, with very little reflection observed upstream of the structure. This is further evidenced by the high amplitude of deflection and transmitted wave signals in the membrane region 5.9a. However, in the LRMM-coupled case shown in figure 5.8b, a rather interesting difference is observed. Since the resonator frequency is chosen to be identical to the excitation frequency, the local resonator is strongly excited and starts to resonate. As a result, the incoming wave is almost entirely reflected, and the transmitted wave amplitude is significantly reduced. This is once identified in figure 5.9b with nearly zero transmitted wave, and the free-surface elevation from upstream is nearly doubled of κ_{in}. This observation shows that with the modification of LRMM, the system can capture wave energy selectively, even for waves that could have fully transmitted the membrane before.

From figure 5.9, it is also observed that the reflected and transmitted wave amplitudes remain constant away from the membrane, whereas localized variations appear in the vicinity of the structure. These localized disturbances correspond to evanescent waves, which decay exponentially in space and do not

transport energy away from the structure. Mathematically, they are associated with solutions involving imaginary wave numbers and are a common feature in wave–structure interaction problems under harmonic excitation. Additionally, it should be noted that continuity between the surface elevation κ and the membrane deflection η is not enforced in this simulation. This is because the membrane and fluid surfaces are treated as distinct boundaries in the model, and the only required continuity is in the velocity potential ϕ, which couples the dynamics across the fluid–structure interface.

In conclusion, the contrast between the membrane-only and coupled systems clearly demonstrates the effectiveness of the LRMM system in selectively inhibiting wave propagation near its eigenfrequency. It also reinforces the insights from the modal analysis that identified the LRMM's capability to dominate the system's response in frequency bands close to its own resonance. The strong reflection and minimal transmission confirm the frequency-selective nature of LRMMs, making them effective candidates for targeted wave mitigation.

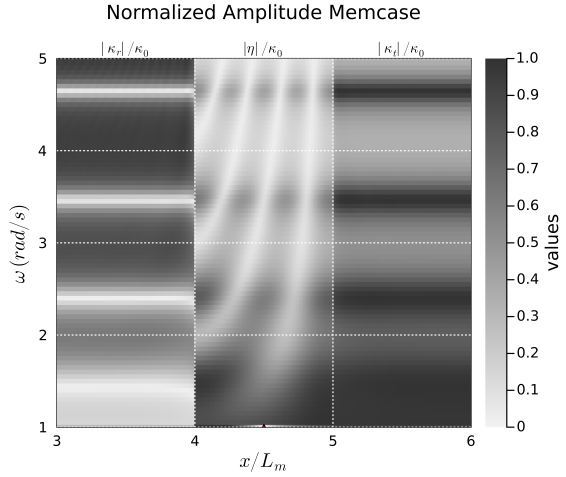

(a) Response contour of the membrane and vicinity water domain

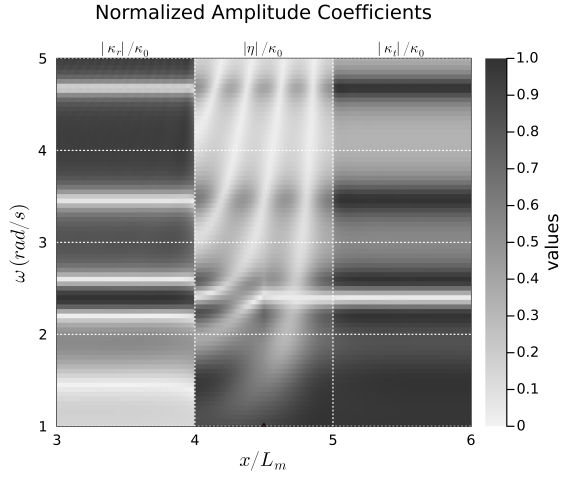

(b) Response contour of coupled system and vicinity water domain solution

Figure 5.10: Response contour plots of the normalized amplitude of the deflection η, reflected wave κ_r, and transmitted wave κ_t in the vicinity of the structure for wave frequency $\omega = [1,\ 5]$

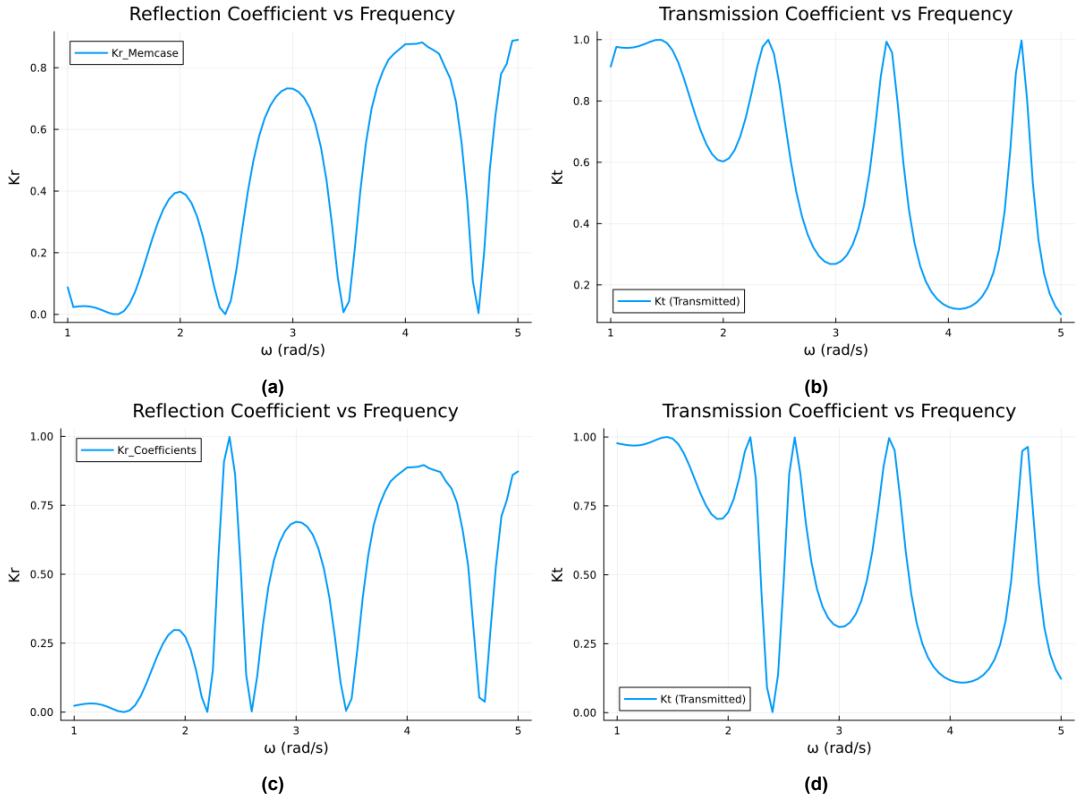

Figure 5.11: Plots of reflection coefficient K_r, transmitted coefficient K_t under monochrome frequency $\omega = [1 : 5]$. (a)(b) membrane-only, (c)(d) coupled system

To further investigate the system's dynamic characteristics without material damping, we perform a series of simulations using monochromatic waves with $\omega = [1, 5]$ rad/s, and evaluate the amplitude of the structural response and wave fields at each frequency. The resulting response contours and energy coefficients are shown in Figure 5.10 and Figure 5.11.

Figure 5.10a presents the normalized amplitude of the membrane deflection η, reflected wave κ_r, and transmitted wave κ_t across the spatial domain and wave frequencies. The overall patterns reveal that lower wave frequencies produce a more pronounced structural response, with η exhibiting higher amplitude in this range. In contrast, higher wave frequencies lead to relatively small membrane deflections, indicating that the structure is more compliant to longer waves and stiffer to shorter ones. Figure 5.10b shows the corresponding response of the coupled system with a local resonator (LRMM) of eigenfrequency $r_\omega = 2.4\,\mathrm{rad/s}$. Compared to the membrane-only case, we observe a significant increase in the amplitude of the reflected waves around the resonator's frequency, indicating strong wave reflection at this specific frequency. Interestingly, the membrane deflection η remains at a similar magnitude, suggesting that the resonator effectively alters wave energy distribution without necessarily increasing structural vibration. This contrast highlights the LRMM's selective filtering capability—reflecting targeted frequencies while maintaining the structural deformation similar to that of the uncoupled membrane.

This frequency-selective behavior is further quantified through the energy coefficients plotted in Figure 5.11. The reflection coefficient K_r and transmission coefficient K_t are calculated for both the membrane-only system (top row) and the coupled LRMM system (bottom row). From previous research results, the membrane can be treated as a frequency-dependent filter, transmitting low-frequency waves and reflecting higher-frequency ones. And for waves whose frequencies are close to the wet natural frequency of the membrane, it can be completely transmitted with no material damping. This

can be seen in Figure 5.11a and 5.11b as troughs in K_r and peaks in K_t, revealing passbands centered around the structure's natural frequencies. These correspond to the white bands in the κ_t contour plot in Figure 5.10a, where transmitted wave amplitudes are high. Conversely, strong reflection is observed outside these resonant bands, forming distinct bandgaps in the spectrum. When the LRMM is introduced, this filtering pattern is fundamentally altered near the resonator frequency. In Figure 5.11c and 5.11d, K_r becomes significantly larger and K_t correspondingly smaller around $\omega = 2.4\ rad/s$—the prescribed LRMM eigenfrequency. A striking transition is observed where a sharp flip occurs: the original single trough in K_r (and peak in K_t) near 2.4 splits into two distinct troughs, approximately located at 2.2 and $2.6\,\mathrm{rad/s}$. This transition reflects the emergence of a reflective bandgap around the resonator frequency, as seen in Figure 5.10b, where the bright passband near $2.4\ rad/s$ in the membrane-only case is replaced by a dark region, bounded by two newly formed passbands.

This spectral splitting behavior aligns closely with the results from the wet modal analysis. As shown in Figure 5.3a, which uses the same structural parameters as the current dynamic test, wet natural frequencies of mode 2 and 3 are found at $2.247\,\mathrm{rad/s}$ and $2.546\,\mathrm{rad/s}$—matching precisely the locations of the new passbands. These arise due to the interaction between the resonator and the membrane, which modifies the original dynamic responses. This modal bifurcation is also clearly visible in Figure 5.4, where a vertical line at $r_\omega = 2.4\ rad/s$ intersects the modal trajectories, showing one resonator-dominated mode and another mode emerging in place of a single mode in the uncoupled case. This confirms that the observed splitting of the energy transmission bands is rooted in the shift and mix of the structure's modal properties induced by LRMM coupling.

In summary, the frequency-domain simulations without damping reveal that the membrane-only system acts as a passive filter, selectively transmitting waves near its natural frequencies and showing abilities in reflecting high-frequency waves. However, the inclusion of LRMM introduces a strong frequency-dependent modulation in this behavior. The resonator disrupts the original passband structure by creating a localized band gap around its eigenfrequency, where wave reflection is significantly enhanced, showing its potential in reflecting certain-frequency energy. This results in the splitting of the original transmission peak into two distinct passbands, accompanied by the formation of a reflective zone in between.

This phenomenon is rooted in the hybridization of the system's vibrational modes. The modal analysis confirms that the resonator introduces a new mode near its resonance frequency, leading to a bifurcation in the modal spectrum. These shifts in the wet natural frequencies directly correspond to the observed changes in wave energy transmission characteristics. The combination of modal and frequency-domain analysis thus reveals the LRMM's potential as a tunable element for controlling wave–structure interaction, enabling the design of structures with customized filtering behavior in the absence of damping.

5.2.2. With damping

Having explored the dynamic response of the coupled system in the absence of material damping, we now proceed to examine how damping within the resonators influences wave structure interaction. This analysis focuses on understanding how energy dissipation mechanisms embedded in the local resonant metamaterials (LRMM) alter the spectral behavior of the system under frequency-domain excitation. In this section, we isolate the effect of damping in the resonators by setting the membrane's viscoelastic parameter $\tau = 0$, as the damping influence on the membrane has been thoroughly explored in previous studies (Agarwal et al., 2024).

Instead, we concentrate on the internal damping within the LRMM components, which are modeled as viscoelastic spring–mass systems. To characterize the damping within each resonator, we adopt a classical mass-spring-dashpot viscoelastic model, where the damping coefficient r_C is defined through

the damping ratio ζ as follows:

$$r_C = 2\zeta\sqrt{r_K r_M} \tag{5.7}$$

Here, r_K and r_M represent the resonator's stiffness and mass, respectively. This formulation ensures that the energy dissipation rate scales with both the inherent mechanical properties of the resonator and the specified damping ratio.

We begin by analyzing the system's response under a single wave frequency $\omega = 2.4$ rad/s, which corresponds to the resonator's natural frequency and is known to induce strong interaction. In this analysis, we set the damping ratio $\zeta = 0.1$, and keep all other variables the same as the LRMM coupled case in Section 5.2.1. Figure 5.12 shows the spatial distribution of the complex solution of velocity potential ϕ, exaggerated membrane deflection η, and free-surface elevation κ at steady state. Compared to the undamped case, the presence of damping suppresses the build-up of resonator-dominated amplification, resulting in a reduced reflected wave amplitude and a modified structural response. And for the transmitted wave, it is observed to be lower than the incoming wave, suggesting there is a part of the wave absorbed or dissipated by the resonator.

This interpretation is further supported by the amplitude plots shown in Figure 5.13, which provide a detailed view of the normalized magnitudes of κ, κ_r, κ_t, and η across the domain. The simulation is conducted using an incident wave with $\omega = 2.4$ rad/s and a fixed amplitude $\kappa_0 = 0.1$m. The reflected wave amplitude is observed to reduce from 2.0 in the undamped case to 1.4 when a damping ratio of $\zeta = 0.1$ is introduced. Meanwhile, the transmitted wave amplitude increases from nearly zero to 0.6, and the structural response η also shows a noticeable decrease in peak magnitude. This initial observation suggests that LRMM damping can effectively tune the energy partition between reflection and absorption, a hypothesis further explored in the following parametric studies.

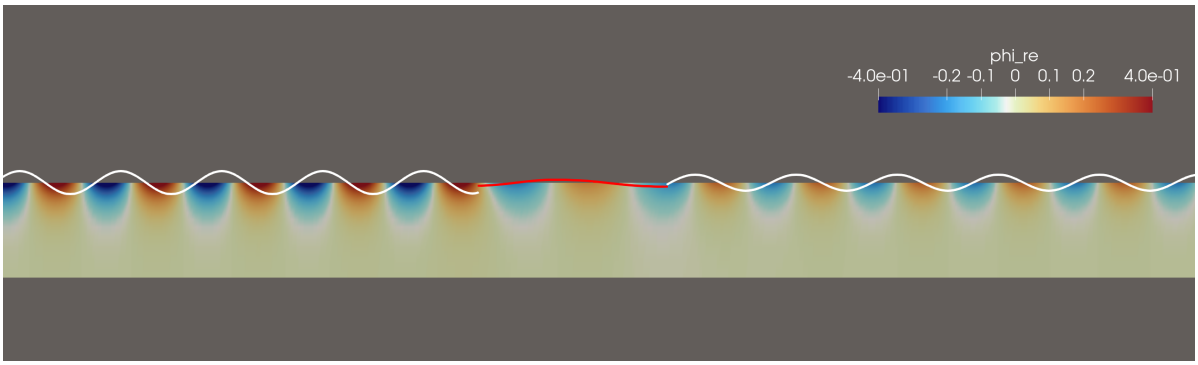

(a) real part solution

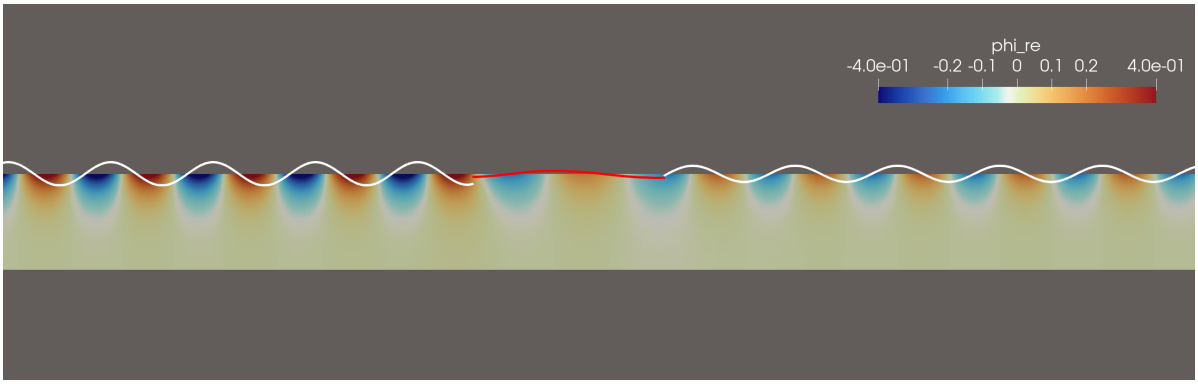

(b) imaginary part solution

Figure 5.12: Numerical simulation results of ϕ in the vicinity of the structure and exaggerated plots of surface elevation κ and structure deformation η under damping situation

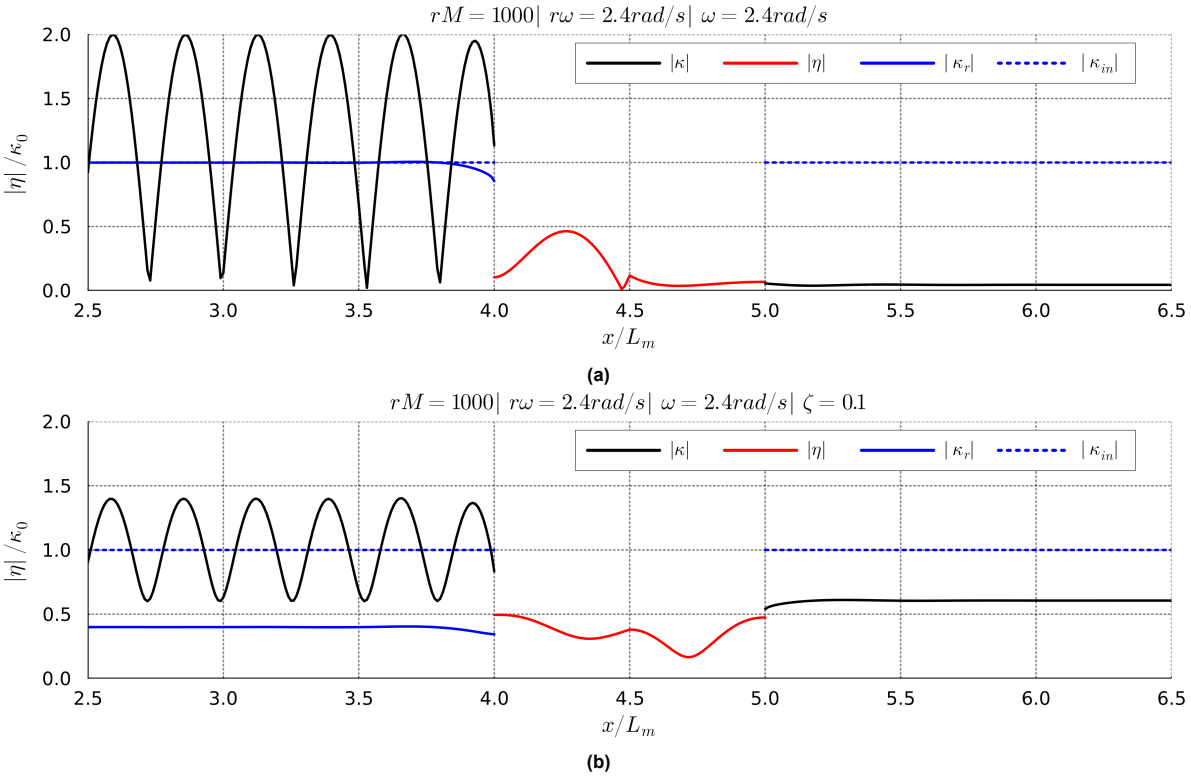

Figure 5.13: Plots of amplitude of structure deflectionη, incoming wave $\kappa_i n$, reflected wave κ_r, transmitted wave κ_t, and total free-surface elevation. (a)no damping situation, (b) with damping ratio $\zeta = 0.1$

Figure 5.14 presents the normalized amplitudes of the membrane deflection η, reflected wave κ_r, and transmitted wave κ_t for a range of excitation frequencies under varying damping ratios ζ applied to the LRMM. These results reveal how damping modifies the system's frequency-selective behavior.

At low damping levels (e.g., $\zeta = 0.02$), the system retains much of the frequency selectivity observed in the undamped case. The reflected wave κ_r still exhibits strong amplitudes at frequencies near the resonator frequency $\omega \approx 2.4$ rad/s, forming a prominent bandgap region. Compared to the undamped case, this bandgap becomes slightly broader, but the peak reflection amplitude is reduced. Simultaneously, the transmitted wave κ_t shows an expansion of the passband region and increased amplitudes, indicating that damping not only introduces energy dissipation but also enhances the structure's permeability to certain frequencies. These patterns are consistent with the previous modal observations and further confirm the resonator's role in governing wave-structure interactions.

As the damping ratio increases (e.g., $\zeta = 0.05$ and 0.1), a progressive smoothing of the wave field emerges. In the κ_r region, the original sharp bandgaps become wider and less distinct, gradually merging with adjacent passbands. The amplitude of reflected waves continues to decrease, though it remains notably higher than in the membrane-only case. On the transmitted side, κ_t exhibits broader high-amplitude bands, but their magnitude stays below that of the membrane-only system. These observations indicate a redistribution of energy from narrow-band reflection toward broader, moderately transmitted ranges, enabled by increased energy absorption within the LRMM.

At high damping ($\zeta = 0.5$), the structure's dynamic response becomes almost indistinguishable from that of the membrane without any resonator. Both reflected and transmitted amplitudes show minimal variation across the frequency spectrum, and the spatial structure of the membrane deflection flattens significantly. This implies that the LRMM no longer contributes meaningfully to dynamic interactions, effectively behaving as a passive mass. Such results underscore the importance of damping ratio selec-

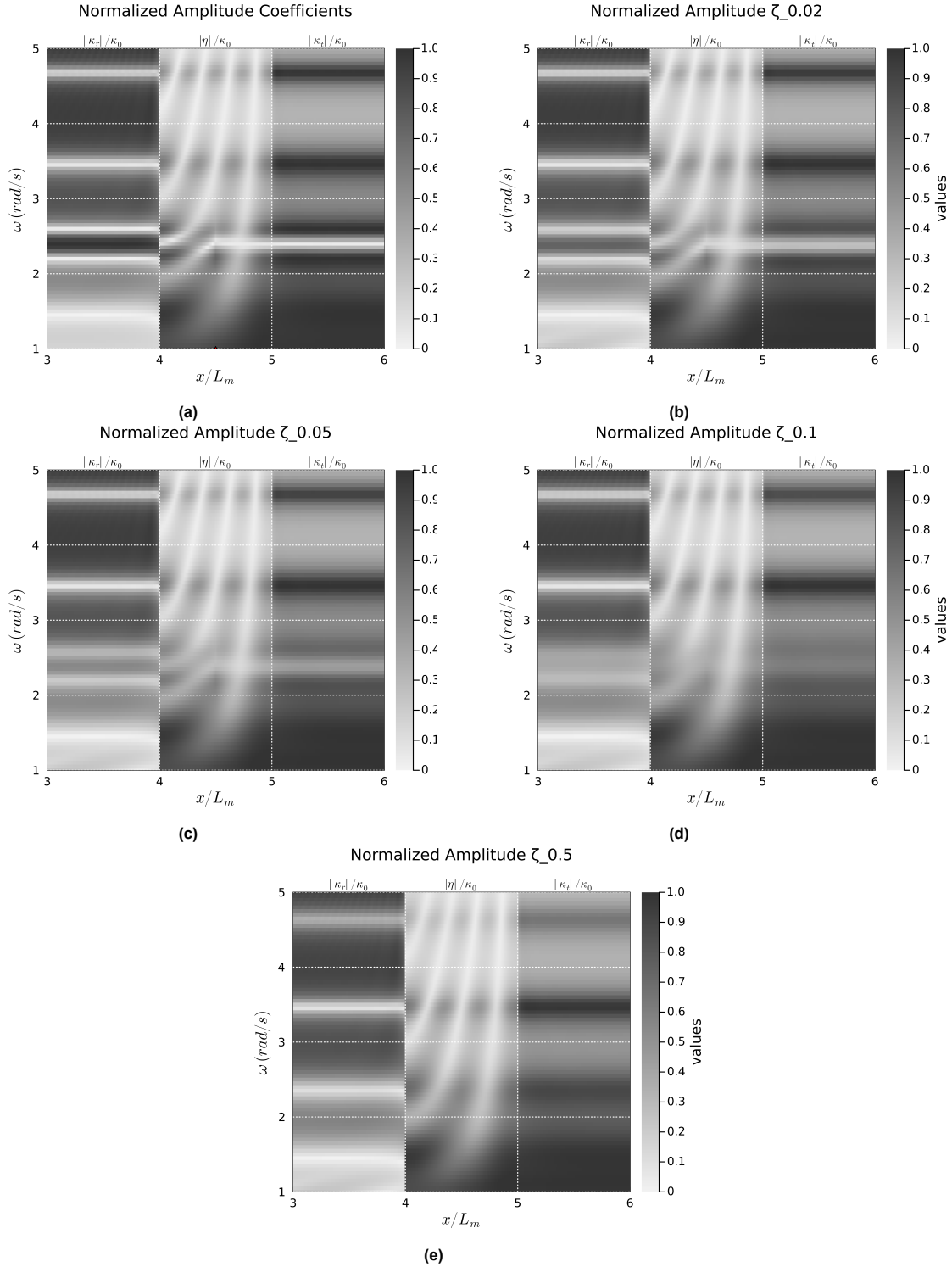

Figure 5.14: Response contour plots of the normalized amplitude of the deflection η, reflected wave κ_r, and transmitted wave κ_t in the vicinity of the structure for wave frequency $\omega = [1,\ 5]$ and for damping ration $\zeta \in [0, 0.02, 0.05, 0.1, 0.5]$

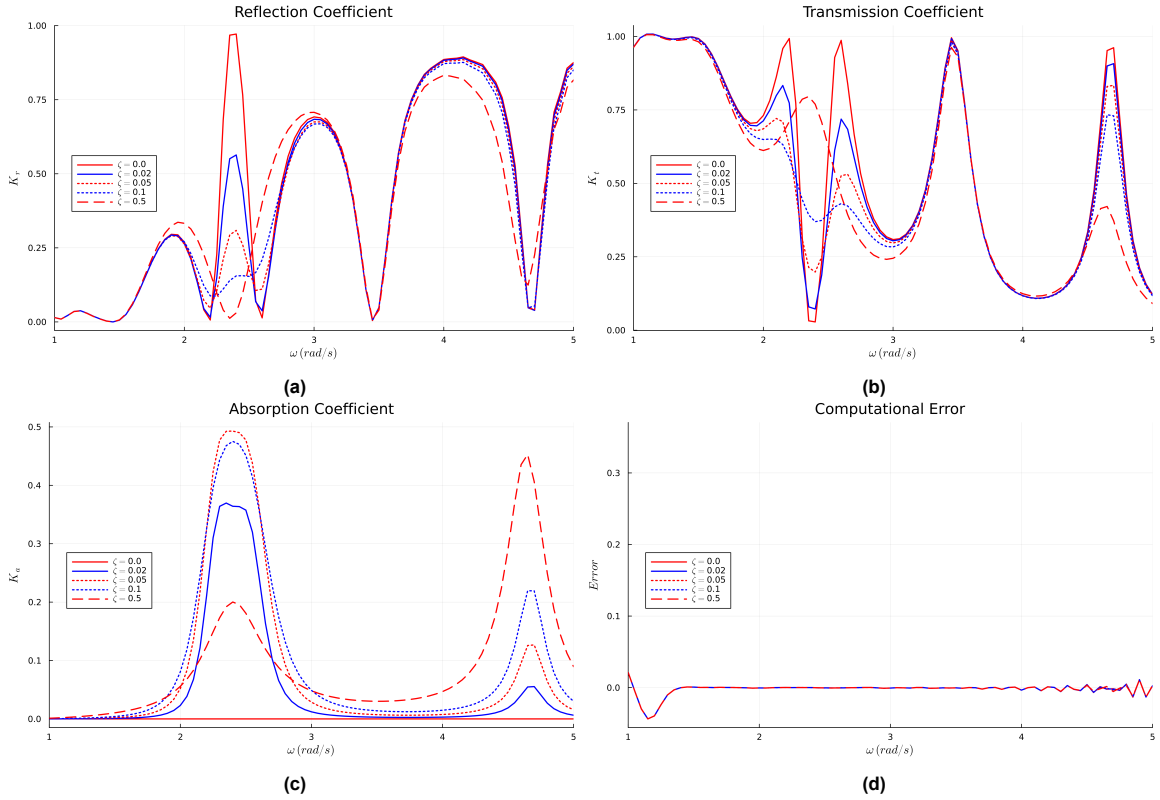

Figure 5.15: Plots of reflection coefficient K_r, transmitted coefficient K_t, and absorption coefficients K_a for $\zeta = [0.01, 0.02, 0.05, 0.1, 0.5]$ under monochrome frequency $\omega = [1:\ 5]$ for

tion: inappropriate values can suppress the LRMM's filtering and amplification effects, while moderate damping enables a balance between selectivity and energy absorption.

In summary, LRMM damping introduces a tunable mechanism to control both wave reflection and transmission characteristics. Low damping preserves selective filtering while slightly widening response bands. Moderate damping smooths modal features and redistributes energy over broader frequencies. Excessive damping neutralizes LRMM effects, rendering the system nearly equivalent to the baseline membrane. These findings highlight the critical sensitivity of wave-structure interactions to the damping level and offer practical insights for engineering resonator-based coastal or floating systems.

The trends observed in the response contours are further corroborated by the energy-based coefficients shown in Figure 5.15. As the damping ratio increases, a significant shift in the energy partition between reflection, transmission, and absorption is observed. Specifically, for low damping values (e.g., $\zeta = 0.02$), the reflection coefficient K_r near the resonant frequencies remains high though dropped compared with no damping, consistent with the strong wave rejection seen in the contour plots. However, as ζ increases further (e.g.,$\zeta = 0.05\ \zeta = 0.1$), K_r continues to decrease while the absorption coefficient K_a increases and begins to dominate, indicating that a significant portion of the incoming wave energy is now dissipated by the LRMM. Notably, the sharp peaks of K_a near the resonant frequencies confirm the damping-enhanced selective absorption capacity of the system.

At very high damping (e.g., $\zeta = 0.5$), the LRMM's influence becomes less pronounced: K_a remains non-negligible, but both K_r and K_t exhibit behavior approaching that of the membrane-only case, consistent with the flattening response observed earlier. This again underscores the importance of tuning the damping ratio to optimize wave energy management.

Interestingly, at $\omega \approx 4.64$ rad/s—corresponding to the membrane's fourth wet natural frequency ω_n^w

(with the mode bifurcation effects due to LRMM, that is fifth mode of the coupled system), we observe that K_r remains nearly constant while K_a increases and K_t decreases with increasing damping ratio ζ. This frequency excites a membrane-dominated mode, where the LRMM is located at an anti-node and thus undergoes noticeable motion (see Figure 5.3). Although not in resonance, the LRMM contributes to energy dissipation through its motion. This contrasts with the third mode, where the LRMM sits at a nodal point and remains almost inactive. As a result, while the LRMM does not induce strong wave reflection here, it acts as a passive damper, increasing energy absorption with higher damping. This explains the observed monotonic rise in K_a and decline in K_t, with K_r largely unaffected.

To ensure the validity of these results, the total energy conservation is evaluated by comparing K_r, K_t, and K_a against the input power. And the power error of the system is defined as:

$$\text{PErr} = \left(1 - \frac{P_r + P_t + P_a}{P_{in}}\right) = 1 - K_r - K_a - K_t \tag{5.8}$$

As shown in Figure 5.15d, the computational error remains low throughout the tested frequency range, confirming the robustness of the numerical model.

6

Parametric Analysis of LRMM's Influence on Coupled System

Building upon the dynamic response analyses presented in Chapter 5, this chapter shifts the focus toward understanding how specific design parameters of the LRMM influence the overall performance of the coupled system. While section 5.2 explored two representative cases—undamped and damped LRMM—to reveal the fundamental mechanisms of wave interaction, the current chapter aims to systematically quantify the influence of key LRMM design variables through targeted parametric sweeps.

In this chapter, we use the parameters combination mentioned below as default. Water depth is $h = 10$m, length of the membrane is $L_m = 2h$, non-dimensional mass of membrane $m_\rho/L_m = 0.045$, tension parameter $T_\rho/gL_m^2 = 0.025$, mass of LRMM is $r_M = 1000$kg, LRMM natural frequency is $r_\omega = 2.4\,rad/s$, and the place of the LRMM is at the middle point of the membrane. To isolate individual parameter effects and avoid the complexity introduced by damping, all analysis here are conducted under the undamped condition ($\zeta = 0$), as the LRMM damping effect has already been extensively discussed in Section 5.2.2.

Three primary LRMM parameters are selected for investigation:

- the internal resonance frequency r_ω,
- and spatial placement of the resonator x_r,
- the resonator-to-water mass ratio rM_ρ.

For each parameter, a wide range of values is explored while holding other variables fixed. The dynamic response of the system is evaluated by computing energy-based coefficients, namely the reflection coefficient K_r, and transmission coefficient K_t, as functions of both the wave excitation frequency ω and the parameter of interest.

The goal of this chapter is twofold: (1) to assess how these LRMM parameters affect the distribution of energy and dynamic response in the coupled water-membrane-LRMM system, and (2) to identify favorable parameter ranges for enhanced wave attenuation or absorption. These insights will help inform the design of LRMM-augmented floating structures tailored for wave control applications.

This chapter is organized as follows:

- Section 6.1 presents a frequency sweep study across different values of r_ω to analyze its impact on system's frequency selectivity and energy redistribution.
- Section 6.2 investigates the spatial placement of the LRMM within the membrane to assess how location affects mode participation and dynamic performance.

- Section 6.3 presents the wave energy redistribution diagrams for different masses, showing its influence and trend.

6.1. Frequency sweep

In the previous chapter, we studied the effect of the LRMM under a specific configuration with $r_\omega = 2.4\,\mathrm{rad/s}$, and observed that the resonator only significantly influences the wave response when its frequency is close to the excitation frequency. This observation suggested a *frequency-selective behavior* of the LRMM. In this section, we conduct a systematic parametric study by sweeping over a wide range of resonator frequencies $r_\omega \in [1, 5]\ rad/s$. The aim is to seek a comprehensive understanding of how the resonator's natural frequency affects the global energy response of the coupled system across a broad excitation range.

For each value of r_ω, a frequency domain simulation is performed under wave frequency ranging from $\omega \in [1, 5]\ rad/s$. We then compute the reflection and transmission coefficients, which are visualized in Figure 6.1a and Figure 6.1b. The horizontal axis denotes the wave frequency, the vertical axis denotes the resonator frequency, and the color indicates the magnitude of the coefficient. A prominent diagonal feature appears in both figures: a black diagonal band in the reflection plot and a corresponding white band in the transmission plot. Along this line, where $r_\omega \approx \omega$, the reflection coefficient approaches 1 while transmission drops to nearly zero, indicating that the wave is almost entirely reflected. This pattern confirms that the LRMM has a strong influence only when it resonates with the incoming wave, reinforcing the frequency-selective nature previously observed in the single-frequency case.

Beyond the diagonal band, we also observe near-vertically distributed alternating patterns of pass bands and band gaps. Specifically, the white regions in the K_r plot and the corresponding dark regions in the K_t plot represent frequency ranges where waves are transmitted through the structure with minimal reflection. These pass bands follow a distinctive distribution: at certain locations, they curve and extend along the diagonal direction aligned with the resonator frequency, eventually merging into the next pass band. When compared with the modal evolution of the system's wet natural frequencies shown in Figure 5.4, we find that the distribution of these pass bands precisely matches the frequency trajectories of the system's resonant modes. This alignment confirms that the transmission bands arise in frequency ranges where the structure undergoes resonance, allowing wave energy to propagate efficiently through the membrane. The modal analysis thus provides a clear explanation for the formation of these bands.

Interestingly, not all pass bands exhibit the same curved or distorted pattern. For instance, the pass band associated with the original membrane mode 3 remains almost perfectly vertical. This behavior can be attributed to the location of the LRMM, which coincides with a nodal point of mode 3. In such cases, the resonator remains largely inactive and exerts minimal influence on the mode shape, preserving the membrane's original modal behavior. In contrast, modes such as membrane mode 2 and mode 4, where the LRMM lies near an antinode, show significant curvature and deformation in both the modal trajectories and the energy maps. These are precisely the modes where the resonator is effectively excited, modifying the system dynamics and shifting the pass bands accordingly. This strong correlation between modal evolution and energy transmission patterns provides a compelling cross-validation of our findings, linking the observed energy behavior to the underlying physical modes of the coupled system.

Overall, this parametric study provides strong evidence that the LRMM only affects wave behavior within a limited frequency range. Its influence is most significant when its resonance aligns with modes that it actively participates in. This confirms its frequency-selective behavior and highlights the importance of tuning the resonator frequency to match the dominant wave frequencies in design applications. Improper tuning may lead to ineffective wave manipulation, while well-matched configurations can significantly enhance the wave control capability of the system. Besides, this plot and Figure 5.4 cross-

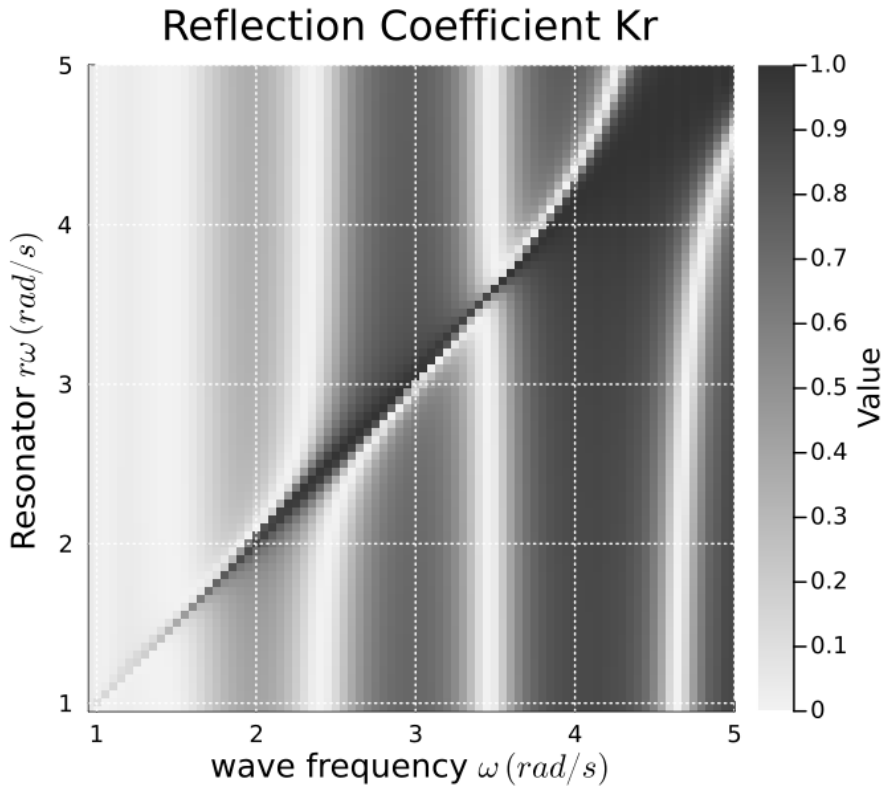

(a) Reflection coefficient K_r

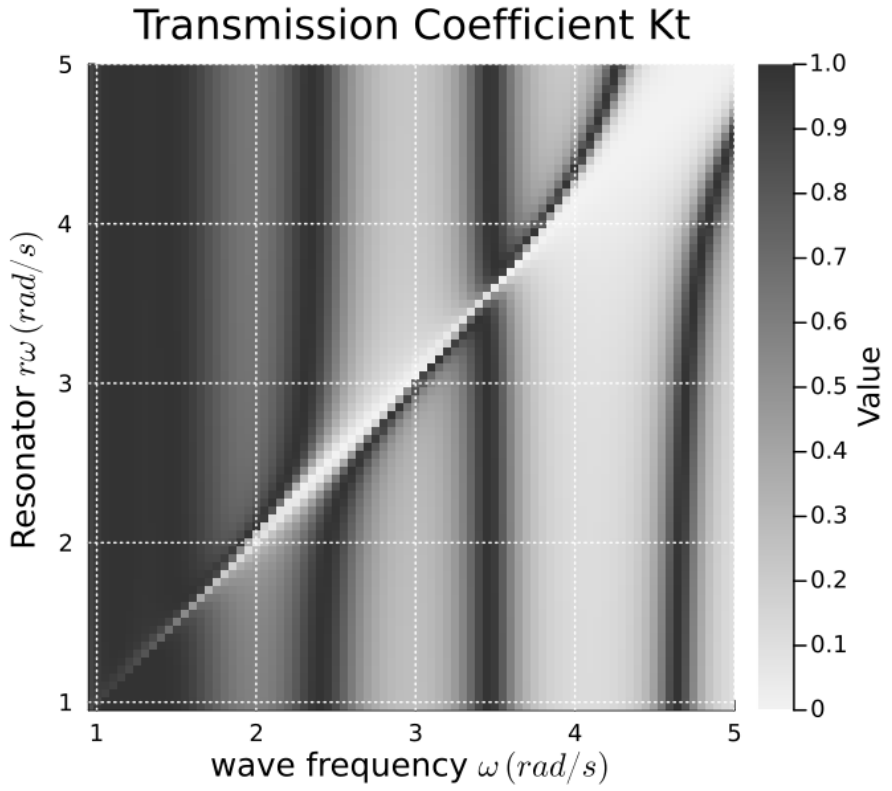

(b) Transmission coefficient K_t

Figure 6.1: Contour plots of reflection coefficient K_r and transmission coefficient K_t for $r\omega \in [1, 5]\ rad/s$, $\omega \in [1, 5]\ rad/s$

validate each other. The modal analysis helps explain the observed response and further highlights the importance of the LRMM position.

6.2. Spatial sweep

In the previous section, we observed that under certain excitation frequencies, the presence of the LRMM had little to no effect on the system response. We initially attributed this phenomenon to the spatial configuration of the resonator—specifically, its alignment with the nodal points of membrane modes, where structural motion is minimal and the resonator remains unexcited. To validate this hypothesis, we now investigate the influence of the LRMM's position along the membrane. In this study, all other parameters, including the resonator frequency and mass, are kept constant. By systematically varying the location of the LRMM and analyzing the resulting energy behavior of the system, we aim to understand how spatial placement affects modal participation and wave–structure interaction performance.

To conduct the spatial sweep, we first select a representative resonator frequency of $r_\omega = 1.55\,\mathrm{rad/s}$, which corresponds to the first wet natural frequency of the membrane. The resonator's position along the membrane, denoted as a normalized coordinate x_r/L_m, is systematically varied from 0 to 1. For each position, we simulate the system response under a range of excitation frequencies, with $\omega \in [1, 5]\,\mathrm{rad/s}$. From each simulation, we extract the reflection coefficient K_r as a function of excitation frequency. These results are then assembled into a contour plot showing K_r as a function of both the LRMM position and the wave frequency. This visualization provides a comprehensive overview of how the spatial placement of the resonator modulates its effectiveness across the excitation spectrum. The figure is shown in 6.2

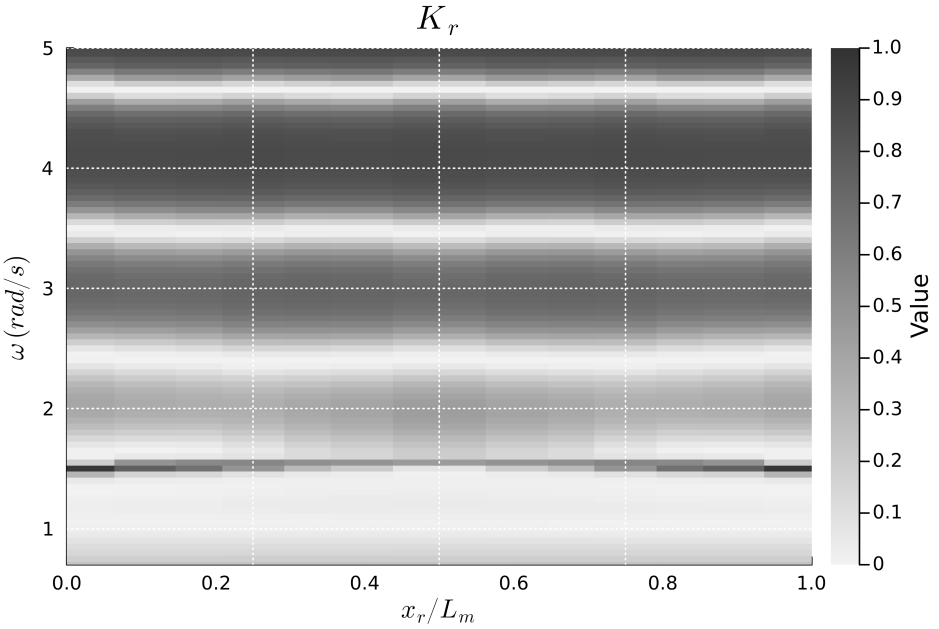

Figure 6.2: Reflection coefficient K_r contour plot for $x_r/L_m \in [0, 1]$, and $\omega \in [1.0, 5.0]\,\mathrm{rad/s}$.

From the resulting contour plot of K_r shown in Figure 6.2, we observe that significant wave reflection occurs when the excitation frequency is close to $\omega = 1.55\,\mathrm{rad/s}$, consistent with the selected resonator frequency. As expected, the magnitude of reflection is not uniform across spatial positions. The res-

onator location moves from the edges of the membrane toward the center, the reflection coefficient gradually decreases, reaching its minimum near the midpoint. This spatial trend resembles the first mode shape observed in the membrane-only configuration, which features a nodal point at the center. However, it is important to note that once a resonator is introduced, the mode shapes of the coupled system are inherently altered. The observed reduction in reflection when the LRMM is placed at the membrane center suggests that, in this particular case, the resonator lies close to a node of the dominant mode at the selected frequency. As a result, structural motion at that point is minimal, leading to weak excitation of the resonator and limited wave interaction. In contrast, the darker regions in the plot indicate positions near anti-nodal points of the dominant mode at the selected frequency.

After examining the special case of $r\omega = 1.55\,rad/s$, we further extend the spatial sweep analysis across a range of resonator frequencies. For each selected $r\omega$, we repeat the same simulation procedure: sweeping the resonator position x_r/L_m across the membrane length, and for each position, computing the reflection coefficient K_r across a range of excitation frequencies $\omega \in [1, 5], \mathrm{rad/s}$. This yields a set of 2D contour plots similar to Figure 6.2, capturing how wave reflection is influenced by both spatial placement and excitation frequency for each resonator configuration. Figure 6.3 presents the contour plots of K_r for a selected set of LRMM natural frequencies that closely match the wet natural frequency of the original membrane.

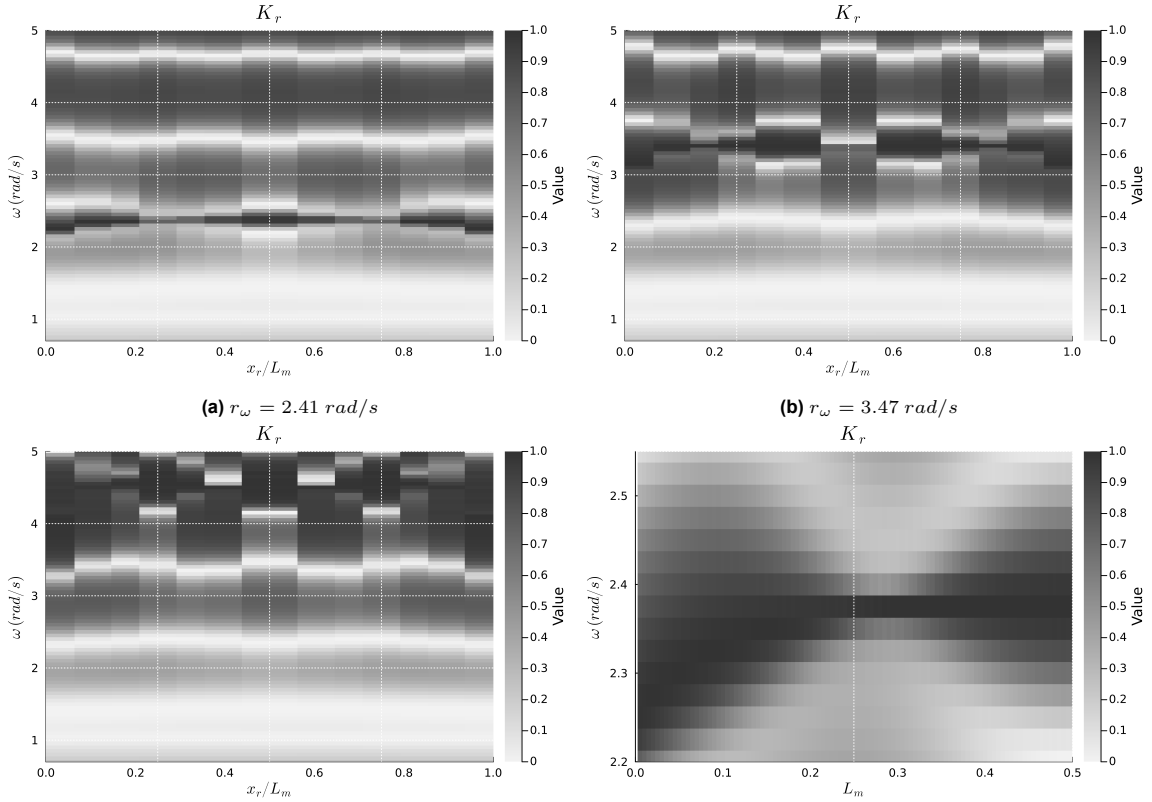

(a) $r_\omega = 2.41\ rad/s$

(b) $r_\omega = 3.47\ rad/s$

(c) $r_\omega = 4.64\ rad/s$

(d) $r_\omega = 2.41\ rad/s$, zoom in around $x/L_m = 0.25$

Figure 6.3: Reflection coefficient K_r contour plot for a selected set of LRMM natural frequencies $r_\omega \in [2.41, 3.47, 4.64]\ rad/s$.

In Figure 6.3a, corresponding to $r_\omega = 2.41\ rad/s$, we observe that the reflection coefficient K_r peaks when the resonator is placed near the center or boundaries of the membrane. These regions likely coincide with areas of high structural displacement in the dominant coupled mode at this frequency, where the resonator can be more effectively excited. Evidence is given by the wet mode shapes of the coupled system for a $2.4\ rad/s$ LRMM is placed at the middle of the membrane (Figure 5.3a).

Interestingly, local reductions in K_r are also observed around one-quarter and three-quarters along the membrane span. However, unlike the case at $r_\omega = 1.55$ rad/s, the reflection does not drop to zero at these locations, as more clearly shown in Figure 6.3d. This difference arises because the mode shapes themselves shift as the resonator position varies, introducing strong coupling effects that alter the nodal structure of the system. As a result, the zero-reflection points no longer align with simple fractional positions on the membrane. This reinforces the importance of the modal analysis of the full coupled system when evaluating spatial placement strategies for the LRMM.

In Figure 6.3b, as well as the previously discussed $r_\omega = 1.55\ rad/s$ case, the dominant mode features a node at the membrane center. Placing the LRMM at this central node does not alter the system symmetry, and although the mode shape changes slightly, the center remains a node. This leads to minimal excitation of the resonator and correspondingly small values of K_r. In contrast, when the resonator is placed at other node positions away from the center, the presence of the LRMM disrupts the structural symmetry. These locations are no longer nodes in the new coupled system, and thus do not exhibit vanishing reflection.

Figure 6.3c shows that the reflection coefficient is high when the LRMM is placed at the membrane center or near the boundaries, whereas lower values are observed around [1/8, 3/8, 5/8, 7/8] positions.

Overall, these spatial sweep results reinforce the idea that LRMM effectiveness is highly dependent on its spatial placement relative to the dominant mode shape at a given excitation frequency. The strongest wave reflection is achieved when the LRMM coincides with an antinode, while placement at or near nodes renders the resonator largely inactive. In particular, when the midpoint is a node—as in certain symmetric modes—it should be avoided. However, beyond these specific cases, the coupled nature of the system leads to complex alterations in mode shapes, making it difficult to predict node or antinode locations. As such, in the following content, we perform a numerical parameter sweep to identify the spatial configurations that maximize wave reflection.

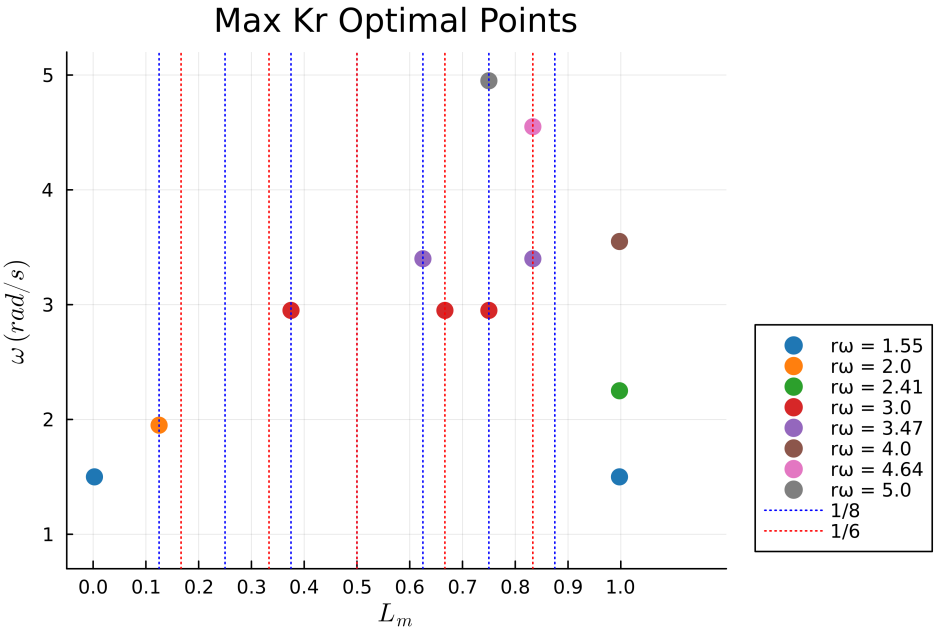

Figure 6.4: Wave reflection optimal pairs for different $r\omega$ under excitation frequency $\omega \in [1, 5]$.

To identify optimal conditions for wave reflection, we extract, for each $r\omega$, the excitation frequency ω and spatial location x_r/L_m corresponding to the maximum K_R in the respective contour map. These optimal pairs are compiled and visualized in a single scatter plot, as shown in Figure 6.4. Each dot represents

one maximum-reflection configuration, with its horizontal position indicating the resonator location and its vertical position indicating the corresponding excitation frequency. Different colors denote different $r\omega$ values. It is noteworthy that the optimal placement of the LRMM has no strict correspondence to the nodes or anti-nodes of the membrane-only modes, instead, it should have a strong correlation with its specific certain modes for the whole system. This further highlights the need to consider the coupled behavior when designing resonator layouts. In general, this plot offers a concise summary of where and when the LRMM is most effective in reflecting wave energy across the tested parameter space, which can serve as practical design guidelines for future implementations.

6.3. Mass ratio sweep

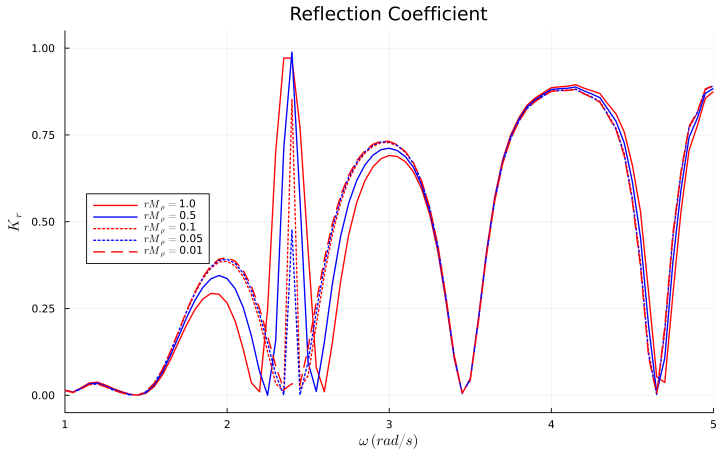

(a) Reflection coefficient K_r

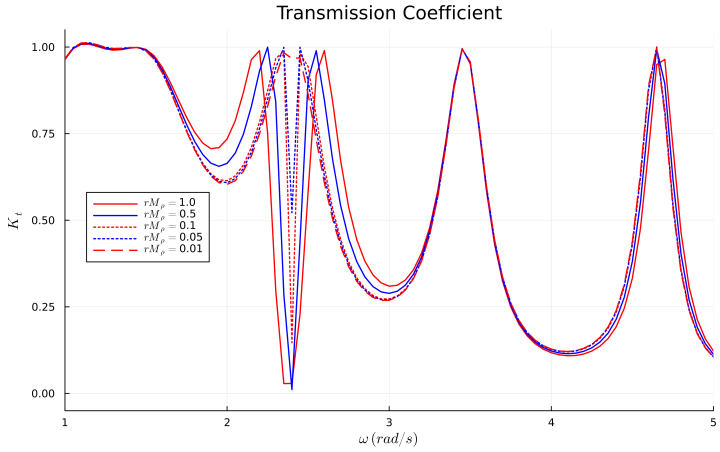

(b) Transmission coefficient K_t

Figure 6.5: Plots of reflection coefficient K_r and transmission coefficient K_t for $rM_\rho \in [0.01, 0.05, 0.1, 0.5, 1.0]$, $\omega \in [1, 5]$

To further examine the influence of resonator properties on system performance, we perform a parametric sweep over the mass ratio rM_ρ, which represents the resonator's relative inertia compared to the membrane. This analysis helps clarify how the resonator's mass affects the system's ability to reflect and transmit wave energy across different excitation frequencies.

Figure 6.5 presents the reflection and transmission coefficients K_r and K_t across a range of excitation

frequencies, for five different mass ratios: $rM_\rho = [1.0, 0.5, 0.1, 0.05, 0.01]$. The resonator's natural frequency is fixed at $r\omega = 2.4\ \mathrm{rad/s}$ in all cases, and no damping is applied.

From the results, we observe a clear trend near the target resonance frequency at $\omega = 2.4\ \mathrm{rad/s}$. As expected, larger resonator masses lead to stronger interaction with incoming waves, resulting in more pronounced peaks in the reflection and transmission coefficients. When $rM_\rho = 1.0$, the system exhibits a sharp peak in K_r and a corresponding dip in K_t, indicating effective wave blocking. Conversely, when $rM_\rho = 0.1$, the response around this frequency becomes much weaker, closely resembling the behavior of a membrane-only system, suggesting that the resonator fails to engage significantly.

Interestingly, we also observe that in the vicinity of the resonance region, particularly around $\omega = 2.0\ \mathrm{rad/s}$, smaller resonator masses produce slightly higher reflection than larger ones. A possible explanation is that for large-mass resonators, only excitation very close to their natural frequency can effectively trigger resonance, while nearby off-resonance frequencies have little effect. In contrast, smaller masses are more easily excited by a broader range of frequencies, allowing the resonator to contribute to wave interaction even outside the primary resonance point. This results in a relatively smoother and more extended reflection profile for lower mass ratios.

In summary, this study confirms that the resonator mass significantly affects the system's frequency-selective behavior. A larger mass leads to stronger interaction and more pronounced wave reflection near resonance, while smaller masses may fail to induce sufficient coupling. These findings support the importance of tuning resonator mass based on the target wave conditions to achieve optimal energy control performance.

7

Application of the hydroelastic LRMM-membrane system

This chapter presents a design-oriented analysis to evaluate the performance of the proposed membrane–LRMM system under a more realistic sea-state. Building upon the frequency-domain results from previous chapters, the system is now subjected to broadband wave excitation derived from a representative JONSWAP spectrum. These simulations serve as a bridge between theoretical studies and practical application, and aim to offer practical insights into the effectiveness of LRMM for wave control and attenuation. To this end, both membrane-only and membrane–LRMM configurations are assessed, with particular focus on how resonator tuning affects system behavior under irregular wave input.

To support upcoming experimental phases of the project, all simulations are conducted using a scaled-down wave condition that approximates typical North Sea parameters at intermediate depths. The setup ensures compatibility between numerical and physical testing environments, and helps position this study within a realistic engineering framework.

7.1. Sea state and numerical setup

To evaluate the practical performance of the proposed membrane–LRMM system, this study adopts a representative sea-state based on real-world measurements from the North Sea, near the Dutch coast. Specifically, we refer to long-term field data collected at intermediate water depths by Rutten et al. (2024). Based on this real-world measurement, a typical sea-state in this region can be characterized by a significant wave height $H_s = 5\,\mathrm{m}$ and a peak wave period $T_p = 8\,\mathrm{s}$, corresponding to a peak wavelength of approximately $71\,\mathrm{m}$ based on linear wave theory.

To ensure compatibility with the physical experiments planned in this project, the numerical simulations are conducted on a scaled-down model. A scaling factor of approximately 0.15 is applied, reducing the membrane length from $134\,\mathrm{m}$ in the prototype to $20\,\mathrm{m}$ in the numerical model. Based on this scaling, the peak wavelength is reduced to about $10.7\,\mathrm{m}$, the significant wave height to roughly $0.75\,\mathrm{m}$, and the water depth from $67\,\mathrm{m}$ to around $10\,\mathrm{m}$. The resulting sea-state is used to generate a JONSWAP wave spectrum, with parameters adjusted accordingly to reflect the scaled conditions (see Figure 7.1).

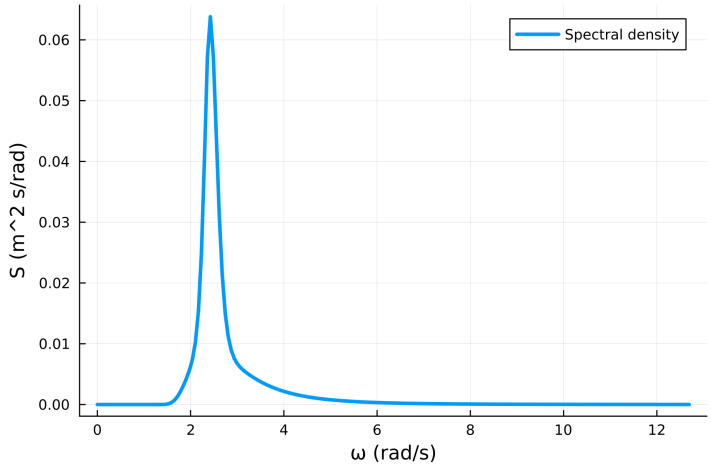

(a) Spectral density spectrum

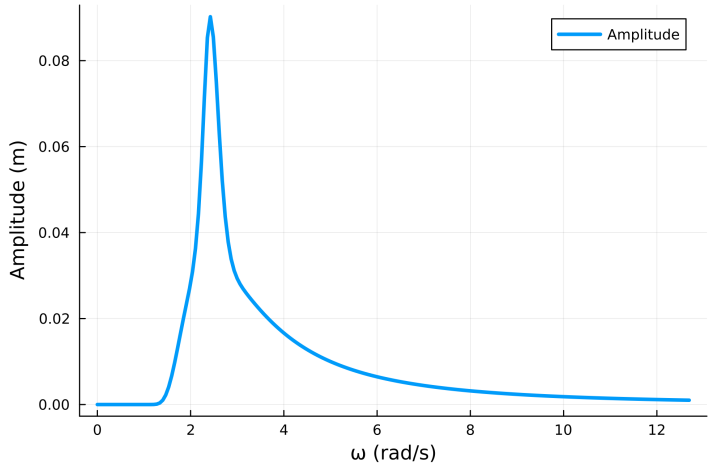

(b) Amplitude spectrum

Figure 7.1: Jonswap spectrum used in the simulation after scaling

The computational model consists of a one-dimensional pre-tensioned membrane structure, centrally coupled with a single LRMM, and floating in a two-dimensional rectangular fluid domain of uniform depth $h = 10\,\text{m}$. The membrane has a total length of $L_m = 20\,\text{m}$ and is placed at $x \in [80, 100]$. A damping zone of length $L_d = 150\,\text{m}$ is applied upstream at $x \in [-150, 0]$ to suppress wave reflections from the structure. On the downstream side, a rigid wall is located at $x = 180\,\text{m}$, acting as the outlet boundary condition. It is also served as an idealized representation for an infinitely wide vertical structure with its bottom fixed at the seabed, and exposed to transmitted wave forces, enabling evaluation of wave impact per unit structural width. The setup is illustrated in Figure 7.2

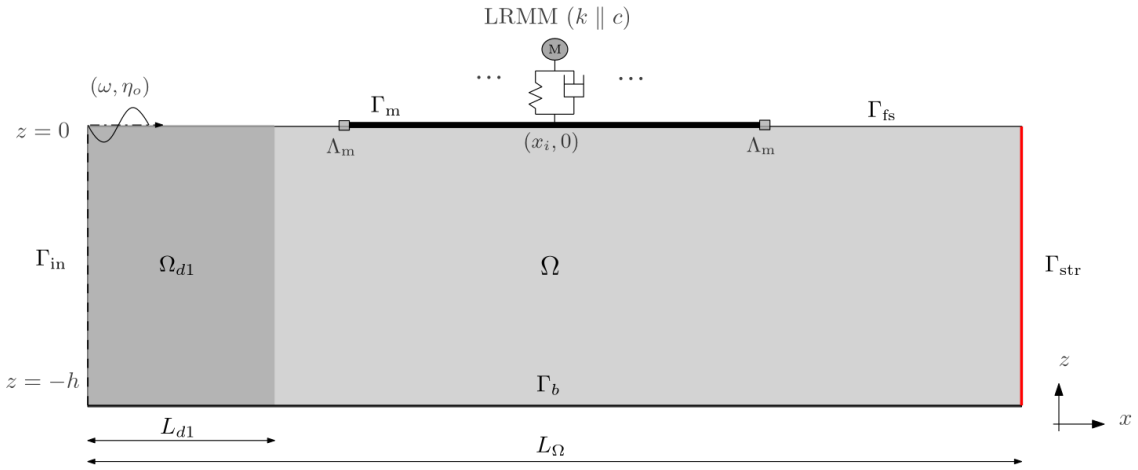

Figure 7.2: Numerical model setup of floating hydroelastic membrane coupled with locally resonant metamaterials under realistic sea-state

The non-dimensional mass and tension parameters of the membrane are defined as $m_\rho/L_m = 0.045$ and $T_\rho/gL_m^2 = 0.025$, respectively. Based on the scaled JONSWAP spectrum introduced earlier, the resonator natural frequency is selected as $r_\omega = 2.4$ rad/s, coinciding with the peak energy frequency of the spectrum. Results from section. 6.3 showed that heavier resonator enhance wave attenuation more effectively by reflecting more incoming waves and allowing less wave passing through. However, to ensure the resonator meaningfully interacts with the system while maintaining the membrane's ability to float, we now investigate two realistic mass values: $r_M = 100\,\mathrm{kg}$ and $250\,\mathrm{kg}$. Furthermore, according to the optimal positioning identified in section. 6.2, the resonator is now placed near the right edge of the membrane. The mesh used for the simulation follows the same discretization strategy adopted in Chapter 5.

7.2. Results and Interpretation

To evaluate the practical performance of the membrane-LRMM system, we compute the wave-induced dynamic force on a bottom-fixed vertical wall located downstream of the floating membrane. This wall acts as a simplified representation of a structural unit subjected to incident wave forces. The dynamic pressure field P_d is derived from the linearized Bernoulli equation as $P_d = \rho i\omega\phi$, where ϕ is the velocity potential of the water domain. Following the linear wave theory formulation, the total dynamic force along the horizontal direction is then obtained by integrating this pressure over the surface of the downstream wall:

$$F_x = \int_{\Gamma_{\mathrm{wall}}} P_d\, n_x\, d\Gamma \tag{7.1}$$

where n_x denotes the x-component of the unit normal vector on the wall surface.

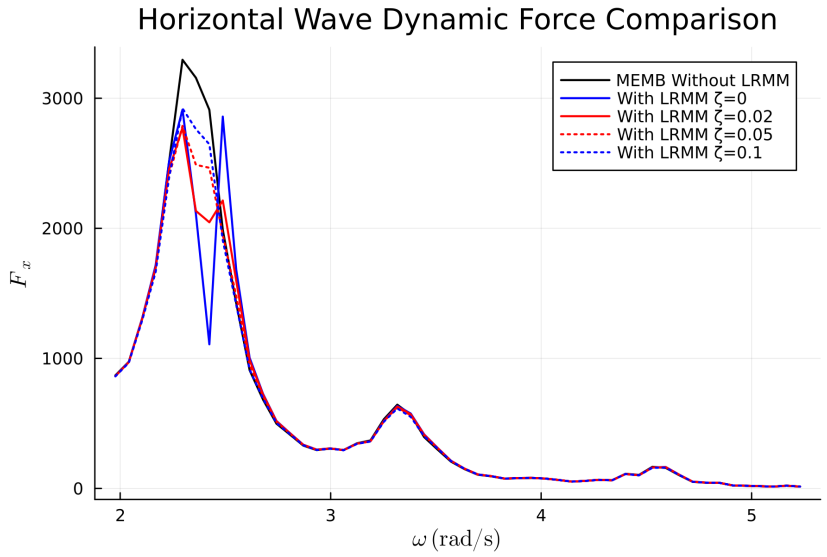

(a) $r_M = 100\,\mathrm{kg}$

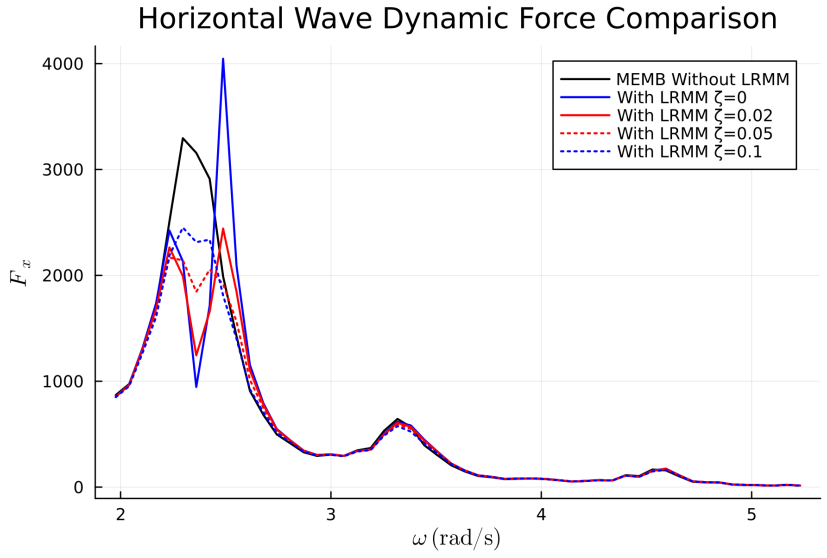

(b) $r_M = 250\,\mathrm{kg}$

Figure 7.3: Comparison of the horizontal force applied on downstream structure for $r_M = 100\ \mathrm{kg},$ and $r_M = 250\ \mathrm{kg}.$

Figure 7.3 presents the variation of this force F_x with respect to wave frequency for several system configurations: a baseline membrane without any resonator, and membranes coupled with a single LRMM having different damping ratios $\zeta = \{0.0,\ 0.02,\ 0.05,\ 0.1\}$. The black curve shows the baseline case, where a dominant peak is observed near $\omega = 2.4$ rad/s. In addition, smaller peaks are observed at higher frequencies around $\omega = 3.5$ and $\omega = 4.7$ rad/s. However, these contribute significantly less force compared to the main resonance peak due to the energy distribution of the JONSWAP spectrum. The most dominant peak corresponds to the second elastic resonance mode of the membrane under sea-state excitation, resulting in strong downstream wave forces.

When a resonator with no damping is introduced ($\zeta = 0$), the force magnitude at around $\omega = 2.4$ rad/s is significantly reduced, confirming the LRMM's ability to alter the structural dynamics and suppress resonance amplification. Meanwhile, two peaks emerge on either side of the original resonance frequency. The new peak appearing on the lower-frequency side represents a resonance mode dominated by the

LRMM, whereas the one on the higher-frequency side corresponds to the shifted membrane-dominated mode of the coupled system. As damping increases, the new peaks become less evident although the force at original peak increase slightly. To quantify the overall wave impact under the realistic sea-state, we integrate the force $F_x(\omega)$ over the range of wave spectrum frequencies. This yields the total horizontal wave force experienced by the downstream structure for each configuration. The results are summarized in Table 7.1. A comparison between the two resonator mass values shows that the $r_M = 250\,\text{kg}$ with material damping configuration generally achieves a greater reduction in the integrated horizontal force than the $r_M = 100\,\text{kg}$ case. While both masses demonstrate the ability to alleviate wave-induced loading when damping is introduced, the heavier resonator interacts more strongly with the membrane and leads to more pronounced attenuation across all damping levels. Among these, for $r_M = 250\,\text{kg}$ with the configuration $\zeta = 0.05$ yields the minimum total wave-induced force, which reduces 12.20% compared to the baseline case without LRMM.

Table 7.1: Integrated horizontal force F_x, force reduction ratio and absorbed wave energy under JONSWAP sea-state excitation.

Mass	**Configuration**	$\mathbf{F_x}$ [N/m]	$\mathbf{F_x}$ reduction [%]	$\mathbf{P_a}$ [W/m]
$\mathbf{r_M = 100\,kg}$	MEMB without LRMM	1825.72	–	–
	With LRMM $\zeta = 0$	1707.27	6.49	–
	With LRMM $\zeta = 0.02$	1704.59	6.63	9.46
	With LRMM $\zeta = 0.05$	1719.82	5.80	8.56
	With LRMM $\zeta = 0.1$	1740.83	4.65	6.39
$\mathbf{r_M = 250\,kg}$	MEMB without LRMM	1825.72	–	–
	With LRMM $\zeta = 0$	1740.07	4.69	–
	With LRMM $\zeta = 0.02$	1605.93	12.04	14.82
	With LRMM $\zeta = 0.05$	1603.07	12.20	16.02
	With LRMM $\zeta = 0.1$	1633.90	10.51	13.30

To further explore its potential as a wave energy converter device, we analyze the corresponding wave energy absorption coefficient K_A in Figure 7.4. This coefficient quantifies the proportion of incident wave power that is absorbed and dissipated by the coupled system. As expected, for both the membrane-only case and the undamped LRMM case ($\zeta = 0$), K_A remains nearly zero across the spectrum. With increasing damping ratio, the absorption coefficient significantly increases. A prominent absorption peak emerges around $\omega \in [2, 3]$ rad/s, confirming the resonator's active role in converting and dissipating wave energy. In addition, secondary peaks appear near $\omega = 3.5, 4.7$ rad/s, which is the third and fourth wet natural frequencies of system. Under these frequencies, the effect of the LRMM can be simplified seen as "added damping" of the system, thus the higher the damping ratio, the larger the absorbed wave energy. Notably, the absorption bandwidth also increases with higher damping ratios, suggesting that a properly damped LRMM can achieve broader frequency coverage and more effective wave energy absorption. To quantify the total energy dissipated by the system, the absorbed wave power $P_a(\omega)$ is integrated across the entire frequency range. This yields the total absorbed wave power for each configuration. The results are presented in Table 7.1. For $r_M = 100\,\text{kg}$ configurations, the case with $\zeta = 0.02$ achieves the highest overall energy absorption 9.46 W/m, and for $r_M = 250\,\text{kg}$, the case with $\zeta = 0.05$ achieves the highest overall energy absorption with 16.02 W/m.

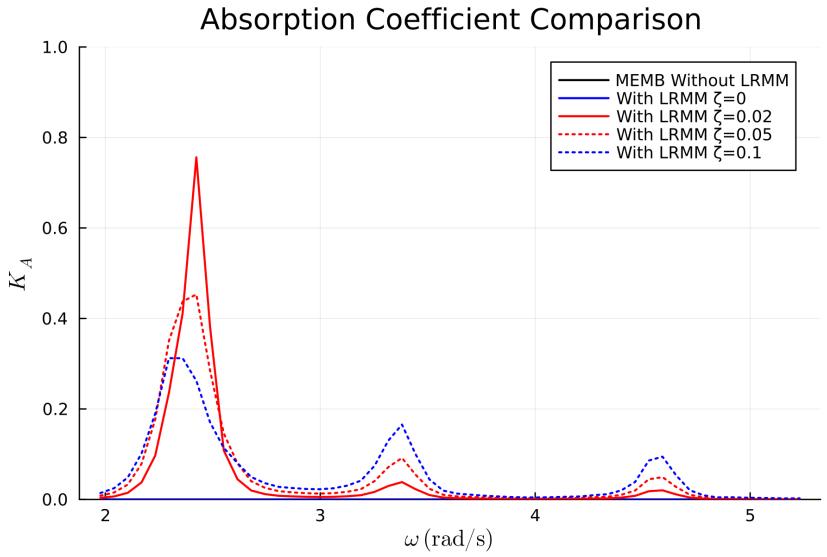

(a) $r_M = 100\,\mathrm{kg}$

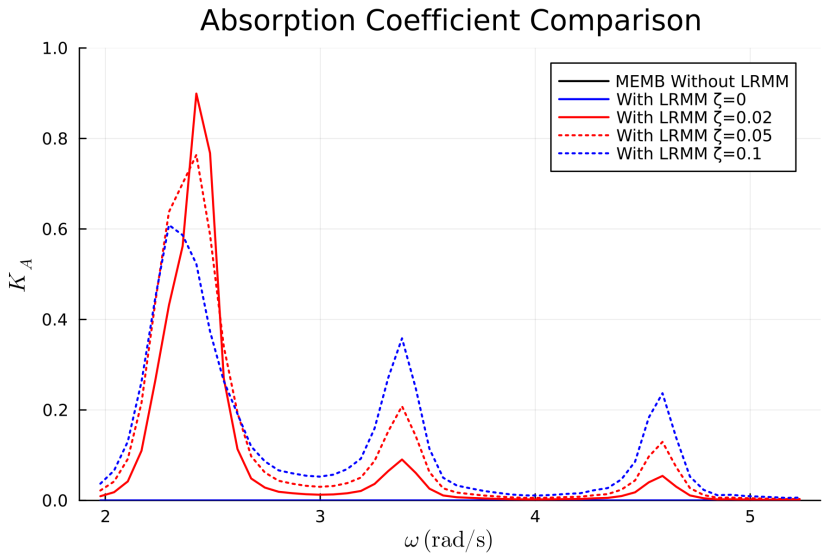

(b) $r_M = 250\,\mathrm{kg}$

Figure 7.4: Comparison of the absorbed wave energy by the system for $r_M = 100\,\mathrm{kg}$, and $r_M = 250\,\mathrm{kg}$.

These results jointly confirm that a properly tuned LRMM–membrane system can further reduce wave-induced structural loads compared to the membrane-only configuration. This improvement is particularly significant in the low-frequency range, where the membrane exhibits limited wave attenuation capability. By carefully selecting the LRMM's properties, the coupled system can be tailored to target specific resonant frequencies within a broader range wave spectrum, thereby enhancing its performance under complex sea-state conditions and improving protection of downstream structures. In addition, when structural damping is introduced to the resonator, part of the incoming wave energy is effectively dissipated—demonstrating the system's potential not only as a protective barrier, but also as a novel wave energy converter. The damping ratio plays a critical role: an appropriate value of ζ helps broaden the absorption band and stabilizes the response, making the system more robust under realistic sea-state excitation.

Moreover, the comparison between different resonator masses shows that a larger r_M generally leads

to stronger interaction and more pronounced reduction of wave-induced forces. This trend also aligns with the observations reported in section 6.3. However, in practical design, the resonator mass cannot be increased indefinitely. Excessive mass would introduce strong local loading and may compromise the floating condition of the membrane. Therefore, selecting an appropriate resonator mass requires balancing performance enhancement with structural safety and buoyancy constraints.

In addition, the present study considers only a single LRMM. An extended design strategy could incorporate an array of resonators or multiple LRMM units tuned to different eigen frequencies. Such configurations have the potential to target multiple frequency bands simultaneously, enabling force reduction and energy absorption over a wider portion of the wave spectrum. Exploring these multi-resonator layouts, as well as optimizing their spatial distribution on the membrane, will form a natural direction for future work.

8

Conclusion and Suggestions

8.1. Conclusion

This study presents a comprehensive numerical investigation of wave–structure interaction involving a floating flexible membrane coupled with a viscoelastic local resonant metamaterial (LRMM) under linear free-surface potential flow theory. Building on an existing monolithic finite element framework, we extended the model to incorporate internal resonators and applied it to analyze the frequency-dependent dynamic response of the system. The goal was to understand how LRMM can be employed to manipulate wave energy propagation, enhance energy absorption, and reduce transmitted forces, particularly under realistic wave conditions.

This study started with defining the governing equation of this multi-physics problem as well as the weak form of the strong coupled system following the monolithic finite element approach. It is worth mentioning that this weak form is used as the basis for all numerical simulations and also the modal analysis in this work.

Subsequently, a comprehensive set of modal analysis was performed, including both dry and wet conditions, to investigate how the introduction of LRMM affects the system's natural frequencies and mode shapes. Results showed that the LRMM introduces a new resonator-dominant mode and modifies other existing membrane modes mode-dependently. Notably, under resonance conditions, LRMM activate localized and highly responsive mode shapes that exhibit strong spatial amplification near the resonator. This effect becomes more pronounced with increasing resonator mass, leading to sharper and more peaked mode shapes. In addition, the influence of the surrounding fluid cannot be neglected. The added mass effect from the surrounding fluid lowers the natural frequencies and leads to smoother mode shapes compared to the dry counterparts.

Following the modal analysis, frequency domain simulations were performed to assess the dynamic wave response across a broad spectrum. Both undamped and damped cases were studied. In the undamped configuration, LRMM were shown to significantly enhance wave reflection near their natural frequencies, validating their frequency-selective behavior. Meanwhile, wave transmission were suppressed even at the natural frequencies of the membrane, which used to fully transmit the wave. This aligns with the fundamental working principle of LRMM: by resonating locally, they create bandgaps that inhibit wave propagation. Damping was found to further increase energy absorption while reducing transmitted wave forces, with an optimal damping ratio yielding the best trade-off between peak suppression and broadband performance. These findings confirm that LRMM remain effective in the context of water waves and highlight their potential for applications in wave energy conversion and coastal protection as passive breakwater systems.

To systematically explore LRMM design parameters, parametric sweeps were conducted over resonator frequency, spatial placement, and mass ratio. The frequency sweep revealed that LRMM only

affect the system when their natural frequency aligns with incoming wave excitation, and that their influence shifts the location and shape of the pass-bands. Interestingly, the resultant figure aligns closely with what we observed in the ω_n versus r_ω plot in the modal analysis part. It showed the relationship between wet natural frequencies and pass-bands. The spatial sweep demonstrated that the LRMM is most effective when placed at antinodes of the dominant mode shape and loses effectiveness near nodal points, underscoring the importance of the modal analysis. Lastly, the mass ratio sweep highlighted the nonlinear relationship between resonator mass and wave interaction: while heavier masses produce sharper resonance peaks, smaller masses contribute to broader and more distributed energy absorption.

The final part of this study demonstrated the application of the coupled membrane–LRMM system under a realistic sea-state condition derived from a JONSWAP spectra. A scaled-down model was used to simulate a floating structure under intermediate water depth conditions. Results showed that the inclusion of an LRMM can significantly reduce the dynamic force acting on downstream structures and enhance wave energy absorption. The performance is highly sensitive to the damping ratio, with moderate damping yielding the most favorable results in terms of both force reduction and absorption. Although the study did not prescribe an optimal parameter configuration for the given sea state, it proposed a complete design framework and evaluation criteria that can be followed for future applications. These findings validate the effectiveness and versatility of the coupled membrane–LRMM system and highlight its potential for wave mitigation and energy absorption in real-world conditions.

Overall, this work confirms the potential of LRMM as an effective tool for tailoring the dynamic behavior of floating membrane systems. Through combined modal analysis, parametric studies, and realistic wave simulations, it lays a numerical foundation for future design and optimization of novel wave energy absorbers or floating breakwaters using locally resonant components.

8.2. Reflection and Suggestions

Building on the framework and findings of this study, several avenues can be pursued to further develop the model and its applications.

First, the current implementation couples a one-dimensional membrane with a two-dimensional fluid domain. This setup effectively represents either a finite 1D structure under 2D water domain or an infinitely wide 2D structure subjected to 3D water domain. To better capture realistic wave–structure interactions, including diffraction, three-dimensional mode shapes, and other complex effect, future work could extend the model to two-dimensional membranes within three-dimensional fluid domains.

Second, since this work represents a first attempt to explore LRMM-coupled floating membranes under wave excitation, the model was deliberately limited to a single resonator for clarity and simplicity. This simplification allowed for the isolation and explanation of fundamental coupling mechanisms. Nonetheless, the developed framework already supports multiple resonators with arbitrary distributions and properties. Future studies may investigate the behavior of membranes coupled with arrays of LRMMs, aiming to optimize their layout for broader frequency coverage and improved energy absorption or mitigation.

In addition, the current simulations are based on linear wave theory and linear structural and resonator responses. While this provides a solid theoretical foundation, real-world wave–structure interactions often exhibit nonlinear behavior. Future research may incorporate nonlinear wave models (e.g., Stokes theory), as well as geometric or material nonlinearities in the membrane. Similarly, the LRMM model could be upgraded from a single-degree-of-freedom linear oscillator to a more complex or nonlinear system as mentioned in Chapter 2. These improvements would allow the model to handle a wider range of realistic conditions and better assess the practical performance and limitations of LRMM-based solutions.

Finally, from a modeling perspective, it is important to reflect on the structural representation adopted in this study. An important modeling assumption throughout this work is the use of a pre-tensioned membrane model to represent the flexible floating structure. This model describes structural stiffness purely through in-plane tension and leads to governing equations involving only second-order spatial derivatives of deformation. In contrast, an Euler–Bernoulli (EB) beam or plate model introduces bending stiffness derived from the material's elastic modulus and the shape of the structure's cross-section, resulting in fourth-order spatial derivatives. This fundamental difference reflects two distinct physical mechanisms: tension-dominated versus bending-dominated behavior. The membrane model is most suitable for ultra-thin, soft structures under significant pre-tension, such as fabrics or very flexible floating structures (VFFS), where structural rigidity primarily arises from axial forces. On the other hand, EB models are better suited for thicker, stiffer structures or those with rigid boundaries and no significant pre-tension, where bending moments become dominant. The choice of structural model can influence the simulation results. Membrane models yield more flexible behaviour, with lower natural frequencies and larger deformations, may lead to more optimistic energy absorption or load reduction estimates at a lower frequency range. Conversely, EB models tend to produce stiffer responses, shifting resonance peaks to higher frequencies. They may enhance wave reflection and suppress deformations at a higher frequency range. In future studies, a model sensitivity study comparing both modeling approaches would be an interesting direction, and could contribute to a more complete theoretical understanding of VLFS.

Bibliography

Abul-Azm, A. G., & Gesraha, M. R. (2000). Approximation to the hydrodynamics of floating pontoons under oblique waves. *Ocean Engineering*, *27*(4), 365–384. https://doi.org/10.1016/S0029-8018(98)00057-2

Agarwal, S., Colomés, O., & Metrikine, A. V. (2024). Dynamic analysis of viscoelastic floating membranes using monolithic finite element method. *Journal of Fluids and Structures*, *129*, 104167. https://doi.org/10.1016/j.jfluidstructs.2024.104167

Agnelli, J., Dib, A., Pierattini, A., & Fantuzzi, N. (2023). Feasibility study of floating photovoltaic panels in the adriatic sea [Madrid, Spain]. *Proceedings of the 2023 IEEE International Conference on Environment and Electrical Engineering and 2023 IEEE Industrial and Commercial Power Systems Europe (EEEIC / I&CPS Europe)*, 1–6. https://doi.org/10.1109/EEEIC/ICPSEurope57605.2023.10194722

Akkerman, I., Meijer, J. H. A., & ten Eikelder, M. F. P. (2020). Isogeometric analysis of linear free surface potential flow. *Ocean Engineering*, *201*, 107114. https://doi.org/10.1016/j.oceaneng.2020.107114

Badia, S., & Verdugo, F. (2020). Gridap: An extensible finite element toolbox in julia. *Journal of Open Source Software*, *5*(52), 2520. https://doi.org/10.21105/joss.02520

Bezanson, J., Edelman, A., Karpinski, S., & Shah, V. B. (2017). Julia: A fresh approach to numerical computing. *SIAM review*, *59*(1), 65–98. https://doi.org/10.1137/141000671

Bigoni, D., Guenneau, S., Movchan, A. B., & Brun, M. (2013). Elastic metamaterials with inertial locally resonant structures: Application to waveguides. *Physical Review B*, *87*(17), 174303. https://doi.org/10.1103/PhysRevB.87.174303

Bishop, R. E. D., & Price, W. G. (1979). Hydroelasticity of ships. *International Journal for Numerical Methods in Engineering*, *15*(6), 949–949. https://doi.org/10.1002/nme.1620150614

Causin, P., Gerbeau, J.-F., & Nobile, F. (2005). Added-mass effect in the design of partitioned algorithms for fluid-structure problems. *Computer Methods in Applied Mechanics and Engineering*, *194*(42–44), 4506–4527.

Cenedese, M., Belloni, E., & Braghin, F. (2021). Interaction of bragg scattering bandgaps and local resonators in mono-coupled periodic structures. *Journal of Applied Physics*, *129*(12), 124501. https://doi.org/10.1063/5.0038438

Chang, I. L., Liang, Z. X., Kao, H. W., Chang, S. H., & Yang, C. Y. (2018). The wave attenuation mechanism of the periodic local resonant metamaterial. *Journal of Sound and Vibration*, *412*, 349–359. https://doi.org/10.1016/j.jsv.2017.10.008

Chen, D., Feng, X., Hou, C., & Chen, J.-F. (2022). A coupled frequency and time domain approach for hydroelastic analysis of very large floating structures under focused wave groups. *Ocean Engineering*, *255*, 111393. https://doi.org/10.1016/j.oceaneng.2022.111393

Chen, Y., Li, L., & Wang, Q. (2024). Design of locally resonant acoustic metamaterials with specified band gaps based on genetic algorithms. *Materials*, *17*(14), 3591. https://doi.org/10.3390/ma17143591

Cheng, Y., Chen, X., Dai, S., Ji, C., Collu, M., Li, M., Yuan, Z., & Incecik, A. (2022). Wave energy extraction and hydroelastic response reduction of modular floating breakwaters as array wave energy converters integrated into a very large floating structure [Part A]. *Applied Energy*, *306*, 117953. https://doi.org/10.1016/j.apenergy.2021.117953

Cho, I. H., & Kim, M. H. (1998). Interactions of a horizontal flexible membrane with oblique incident waves. *Journal of Fluid Mechanics*, *367*, 139–161. https://doi.org/10.1017/S0022112098001499

Colomes, O. (2022, April). *MonolithicFEMVLFS.jl* (Version 0.1.0). https://doi.org/10.4121/19601419

Colomés, O., Verdugo, F., & Akkerman, I. (2022). A monolithic finite element formulation for the hydroelastic analysis of very large floating structures. *International Journal for Numerical Methods in Engineering*, 1–38. https://doi.org/10.1002/nme.7140

Dai, J., Wang, C. M., Utsunomiya, T., & Duan, W. (2018). Review of recent research and developments on floating breakwaters. *Ocean Engineering*, *158*, 132–151. https://doi.org/10.1016/j.oceaneng.2018.03.083

Ertekin, R. C., & Kim, J. W. (1998). A parametric study of the hydroelastic response of a floating, mat-type runway in regular waves. *IEEE Oceanic Engineering Society. OCEANS'98. Conference Proceedings (Cat. No. 98CH36259)*, *2*, 988–992.

European Commission. (2020). *An eu strategy to harness the potential of offshore renewable energy for a climate neutral future*. https://eur-lex.europa.eu/legal-content/EN/TXT/PDF/?uri=CELEX:52020DC0741

Fang, X., Wen, J., Yu, D., Huang, G., & Yin, J. (2018). Wave propagation in a nonlinear acoustic metamaterial beam considering third harmonic generation. *New Journal of Physics*, *20*. https://doi.org/10.1088/1367-2630/aaf65e

Georgiadis, C. (1981). *Wave induced vibrations of continuous floating structures* [Doctoral dissertation, University of Washington] [Doctoral thesis].

He, J., Liu, Y., Zhao, L., & Qiao, P. (2023). Vibration suppression and impact mitigation characteristics of locally resonant metamaterials under different excitation conditions. *Composite Structures*, *304*, 116288. https://doi.org/10.1016/j.compstruct.2022.116288

Huang, H. H., & Sun, C. T. (2009). Wave attenuation mechanism in an acoustic metamaterial with negative effective mass density. *New Journal of Physics*, *11*(1), 013003. https://doi.org/10.1088/1367-2630/11/1/013003

Hübner, B., Walhorn, E., & Dinkler, D. (2004). A monolithic approach to fluid–structure interaction using space–time finite elements. *Computer Methods in Applied Mechanics and Engineering*, *193*(23-26), 2087–2104. https://doi.org/10.1016/j.cma.2004.01.024

Ioannou, R., Stratigaki, V., Loukogeorgaki, E., & Troch, P. (2025). Establishing aem structural framework within sph-mbd coupling for hydro-viscoelastic response of very flexible floating structures. *Applied Ocean Research*, *164*, 104760. https://doi.org/10.1016/j.apor.2025.104760

Karmakar, D., & Soares, C. G. (2012). Scattering of gravity waves by a moored finite floating elastic plate. *Applied Ocean Research*, *34*, 135–149.

Kim, M. W., Koo, W., & Hong, S. Y. (2014). Numerical analysis of various artificial damping schemes in a three-dimensional numerical wave tank. *Ocean Engineering*, *75*, 165–173. https://doi.org/10.1016/j.oceaneng.2013.10.012

Krushynska, A. O., Kouznetsova, V. G., & Geers, M. G. D. (2014). Towards optimal design of locally resonant acoustic metamaterials. *Journal of the Mechanics and Physics of Solids*, *71*, 179–196. https://doi.org/10.1016/j.jmps.2014.07.004

Li, Z., Yu, L., Zhang, X., & Wang, X. (2025). Design and vibration isolation analysis of locally resonant metamaterials based on multiple anti-resonance modes. *International Journal of Non-Linear Mechanics*, *153*, 104639. https://doi.org/10.1016/j.ijnonlinmec.2024.104639

Liu, Z., Zhang, X., Mao, Y., Zhu, Y. Y., Yang, Z., Chan, C. T., & Sheng, P. (2000). Locally resonant sonic materials. *Science*, *289*(5485), 1734–1736. https://doi.org/10.1126/science.289.5485.1734

Lobeto, H., Menendez, M., & Losada, I. J. (2021). Future behavior of wind wave extremes due to climate change. *Scientific Reports*, *11*(1). https://doi.org/10.1038/s41598-021-86524-4

Loukogeorgaki, E., Michailides, C., & Angelides, D. C. (2012). Hydroelastic analysis of a flexible mat-shaped floating breakwater under oblique wave action. *Journal of Fluids and Structures*, *31*, 103–124. https://doi.org/10.1016/j.jfluidstructs.2012.02.011

Meylan, M. H. (2021). Time-dependent motion of a floating circular elastic plate. *Fluids*, *6*(1), 29. https://doi.org/10.3390/fluids6010029

Michele, S., Buriani, F., Renzi, E., van Rooij, M., Jayawardhana, B., & Vakis, A. I. (2020). Wave energy extraction by flexible floaters. *Energies*, *13*(23), 6167. https://doi.org/10.3390/en13236167

Ohkusu, M., & Nanba, M. (1996). Hydroelastic behavior of a very large floating platform in waves [Hamburg, Germany]. *Proceedings of the 11th International Workshop on Water Waves and Floating Bodies*.

Pires, F., Sangiuliano, L., Denayer, H., Deckers, E., Desmet, W., & Claeys, C. (2022). The use of locally resonant metamaterials to reduce flow-induced noise and vibration. *Journal of Sound and Vibration*, *535*, 117106. https://doi.org/10.1016/j.jsv.2022.117106

Price, W. G., & Wu, Y. (1985). Hydroelasticity of marine structures. *Theoretical and Applied Mechanics*, 311–337. https://doi.org/10.1016/B978-0-444-87707-9.50026-9

Ramanan, C. J., Lim, K. H., Kurnia, J. C., Roy, S., Bora, B. J., & Medhi, B. J. (2024). Towards sustainable power generation: Recent advancements in floating photovoltaic technologies. *Renewable and Sustainable Energy Reviews*, *194*, 114322. https://doi.org/10.1016/j.rser.2024.114322

Renzi, E., Stallard, C., & Crossley, A. J. (2016). Hydroelectromechanical modelling of a piezoelectric wave energy converter. *Proceedings of the Royal Society A: Mathematical, Physical and Engineering Sciences*, *472*(2195), 20160715. https://doi.org/10.1098/rspa.2016.0715

Rutten, J., Tissier, M., van Wiechen, P., Zhang, X., de Vries, S., Reniers, A., & Mol, J.-W. (2024). Continuous wave measurements collected in intermediate depth throughout the north sea storm season during the realdune/reflex experiments. *Data*, *9*(5), 70. https://doi.org/10.3390/data9050070

Sugino, C., Xia, Y., Leadenham, S., Ruzzene, M., & Erturk, A. (2016). A general theory for bandgap estimation in locally resonant metastructures. *arXiv preprint arXiv:1612.03130*. https://arxiv.org/abs/1612.03130

Suzuki, H. (2005). Overview of megafloat: Concept, design criteria, analysis, and design. *Marine Structures*, *18*(2), 111–132. https://doi.org/10.1016/j.marstruc.2005.07.006

Suzuki, H., Riggs, H., Fujikubo, M., Shugar, T., Seto, H., Yasuzawa, Y., Bhattacharya, B., Hudson, D., & Shin, H. (2006). Very large floating structures. *Proceedings of the International Conference on Offshore Mechanics and Arctic Engineering*, *42681*, 597–608.

Takeuchi, M., & Yoshida, I. (2022). Mega floating city "green float": Concept and technology innovations [In: Piątek, Ł., Lim, S.H., Wang, C.M., de Graaf-van Dinther, R. (eds), WCFS2020. Springer, Singapore]. *Lecture Notes in Civil Engineering*, *158*. https://doi.org/10.1007/978-981-16-2256-4_1

Taylor, R. E. (2007). Hydroelastic analysis of plates and some approximations. *Journal of Engineering Mathematics*, *58*(1–4), 267–278. https://doi.org/10.1007/s10665-006-9121-7

Trapani, K., Millar, D. L., & Smith, H. C. (2013). Novel offshore application of photovoltaics in comparison to conventional marine renewable energy technologies. *Renewable Energy*, *50*, 879–888.

Valappil, S. V., & Aragón, A. M. (2025). Analytical modeling of damped locally-resonant metamaterials. *Wave Motion*, *136*, 103527. https://doi.org/10.1016/j.wavemoti.2025.103527

Verdugo, F., & Badia, S. (2022). The software design of gridap: A finite element package based on the julia jit compiler. *Computer Physics Communications*, *276*, 108341. https://doi.org/10.1016/j.cpc.2022.108341

Wang, C. M., & Tay, Z. Y. (2011). Very large floating structures: Applications, research and development. *Procedia Engineering*, *14*, 62–72. https://doi.org/10.1016/j.proeng.2011.07.007

Wang, G., Wan, S., Hong, J., Liu, S., & Li, X. (2023). Enhancement of the vibration attenuation characteristics in local resonance metamaterial beams: Theory and experiment. *Mechanical Systems and Signal Processing*, *188*, 110036. https://doi.org/10.1016/j.ymssp.2022.110036

Wu, C., Arju, N., Kelp, G., Fan, J. A., Dominguez, J., Gonzales, E., Tutuc, E., Brener, I., & Shvets, G. (2013). Silicon-based infrared metamaterials with ultra-sharp fano resonances [Submitted on 25 Sep 2013]. *arXiv preprint arXiv:1309.6616*. https://doi.org/10.48550/arXiv.1309.6616

Wu, Y. (1984). *Hydroelasticity of floating bodies* [Doctoral dissertation, University of Brunel] [Doctoral dissertation].

Yago, K. (1997). Model experiment and numerical calculation of the hydroelastic behavior of matlike vlfs. *Proceedings of the International Workshop on VLFS*, 209–216.

Zhang, M., & Schreier, S. (2022). Review of wave interaction with continuous flexible floating structures. *Ocean Engineering*, *264*, 112404. https://doi.org/10.1016/j.oceaneng.2022.112404

A

Semi-analytical derivation of the natural frequencies of the coupled system

Appendix A presents a semi-analytical approach for deriving the formula of dry natural frequencies. This approach starts from the matrix form of eigenvalue problem and aims to provide insights for understanding how the LRMM influence the natural frequencies of the system. Please note that this is not the method used to calculate the natural frequencies in this research. Rather, it offers a perspective from the basic formulation to understand the coupled system's unique dynamic response.

Dry modal analysis with a point-coupled oscillator

$$\begin{bmatrix} K_{11}^d + K_{11}^r - \omega^2 M_{11} & C_{14} \\ C_{41} & K_{44} - \omega^2 M_{44} \end{bmatrix} \begin{bmatrix} \eta_h \\ q_h \end{bmatrix} = \begin{bmatrix} 0 \\ 0 \end{bmatrix}. \tag{A.1}$$

Matrix definitions.

$$\begin{aligned} M_{11}(\eta_h, v_h) &:= (m_\rho\, \eta_h,\, v_h)_{\Gamma_m}, & K_{11}^d(\eta_h, v_h) &:= (T_\rho \nabla \eta_h,\, \nabla v_h)_{\Gamma_m}, \\ K_{11}^r(\eta_h, v_h) &:= +rK\, \delta_p(\eta_h,\, v_h), & K_{44}(q_h, \xi_h) &:= +rK\, \delta_p(q_h,\, \xi_h), \\ M_{44}(q_h, \xi_h) &:= rM\, \delta_p(q_h,\, \xi_h), & C_{14}(q_h, v_h) &:= -rK\, \delta_p(q_h,\, v_h), \\ C_{41}(\eta_h, \xi_h) &:= -rK\, \delta_p(\eta_h,\, \xi_h), & \delta_p(f, g) &:= f(a)\, g(a). \end{aligned} \tag{A.2}$$

Weak forms and Schur elimination.

Let $\lambda = \omega^2$. For any v_h, ξ_h,

$$\big(K_{11}^d - \lambda M_{11}\big)(\eta_h, v_h) + rK\, \delta_p(\eta_h, v_h) - rK\, \delta_p(q_h, v_h) = 0, \tag{A.3}$$

$$-rK\, \delta_p(\eta_h, \xi_h) + (rK - \lambda rM)\, \delta_p(q_h, \xi_h) = 0. \tag{A.4}$$

Since $\delta_p(f, g) = f(a)g(a)$, from (A.4) we get

$$(rK - \lambda rM)\, q_h(a) = rK\, \eta_h(a) \;\Rightarrow\; q_h(a) = \frac{rK}{rK - \lambda rM}\, \eta_h(a). \tag{A.5}$$

Substituting $q_h(a)$ into (A.3),

$$\begin{aligned} &\big(K_{11}^d - \lambda M_{11}\big)(\eta_h, v_h) + \left[rK - \frac{rK^2}{rK - \lambda rM}\right] \delta_p(\eta_h, v_h) = 0 \\ \iff \quad &\big(K_{11}^d - \lambda M_{11}\big)(\eta_h, v_h) - \frac{rK\,\lambda rM}{rK - \lambda rM}\,\delta_p(\eta_h, v_h) = 0. \end{aligned} \tag{A.6}$$

Define the dynamic point-stiffness correction

$$\boxed{\alpha_{\mathrm{dyn}}(\omega) := \frac{rK\,\lambda rM}{rK - \lambda rM} = \frac{rK\,\omega^2 rM}{rK - \omega^2 rM}.} \tag{A.7}$$

Single-mode Ritz projection.

For the n-th dry mode shape ϕ_n, take

$$\eta_h(x) = \eta_p\,\phi_n(x), \qquad v_h = \phi_n(x).$$

Introduce

$$\boxed{M_d := (m_\rho \phi_n, \phi_n)_{\Gamma_m}, \quad K_d := (T_\rho \nabla\phi_n, \nabla\phi_n)_{\Gamma_m}, \quad \delta_n := \delta_p(\phi_n, \phi_n) = \phi_n(a)^2.} \tag{A.8}$$

Then (A.6) reduces to the scalar characteristic equation

$$-\lambda M_d + K_d \;-\; \alpha_{\mathrm{dyn}}(\omega)\,\delta_n = 0, \qquad \alpha_{\mathrm{dyn}}(\omega) \text{ given by (A.7).} \tag{A.9}$$

Quadratic form in $\lambda = \omega^2$.

Clearing the denominator in (A.9):

$$\begin{aligned} &\big(-\lambda M_d + K_d\big)(rK - \lambda rM) - \delta_n rK\,\lambda rM = 0 \\ \iff \quad &-M_d rK\,\lambda + M_d rM\,\lambda^2 + K_d rK - K_d rM\,\lambda - \delta_n rK rM\,\lambda = 0 \\ \iff \quad &-M_d rM\,\lambda^2 + \big(M_d rK + K_d rM + \delta_n rK rM\big)\lambda - K_d rK = 0. \end{aligned} \tag{A.10}$$

Closed-form eigenfrequencies.

Solving (A.10) gives two coupled branches:

$$\boxed{\omega_{n,\pm}^2 = \frac{M_d rK + rMK_d + \delta_n rK rM \;\pm\; \sqrt{\big(M_d rK + rMK_d + \delta_n rK rM\big)^2 - 4\,rMM_d\,rKK_d}}{2\,rMM_d}.} \tag{A.11}$$

Remarks.

(i) If $\delta_n = 0$ (oscillator mounted at a node of ϕ_n), then $(-\lambda M_d + K_d)(rK - \lambda rM) = 0$, so $\lambda = \frac{K_d}{M_d}$ (membrane dry mode) or $\lambda = \frac{rK}{rM}$ (oscillator).
(ii) If the oscillator is absent ($rK = 0$ or $rM = 0$), one recovers the dry frequency $\omega_{d,n}^2 = \frac{K_d}{M_d}$.

B

Derivation of Effective Added Mass in Wet Modal Analysis

Block-form EVP.

Let the unknown variable vector be $\mathbf{U} = [\,\eta,\ \phi,\ \kappa,\ q\,]^\top$, the generalized eigenvalue problem for the wet modal analysis can be written as

$$\big(\mathbf{K}(\omega) - \omega^2\mathbf{M}\big)\,\mathbf{U} = \mathbf{0}, \qquad \mathbf{U} = [\,\eta,\ \phi,\ \kappa,\ q\,]^\top, \tag{B.1}$$

where the mass and stiffness matrices are block-structured as

$$\mathbf{M} = \begin{bmatrix} \mathbf{M}_{11} & \mathbf{0} & \mathbf{0} & \mathbf{0} \\ \mathbf{0} & \mathbf{0} & \mathbf{0} & \mathbf{0} \\ \mathbf{0} & \mathbf{0} & \mathbf{0} & \mathbf{0} \\ \mathbf{0} & \mathbf{0} & \mathbf{0} & \mathbf{M}_{44} \end{bmatrix}, \qquad \mathbf{K} = \begin{bmatrix} \mathbf{K}_{11} + \mathbf{K}_{11}^{(r)} & \mathbf{C}_{12} & \mathbf{0} & \mathbf{C}_{14} \\ \mathbf{C}_{21} & \mathbf{K}_{22} & \mathbf{C}_{23} & \mathbf{0} \\ \mathbf{0} & \mathbf{C}_{32} & \mathbf{K}_{33} & \mathbf{0} \\ \mathbf{C}_{41} & \mathbf{0} & \mathbf{0} & \mathbf{K}_{44} \end{bmatrix}. \tag{B.2}$$

Here, $\mathbf{M}_{11}$ and $\mathbf{K}_{11}$ are the structural mass and stiffness matrices (including tension and gravity terms), $\mathbf{K}_{22}$ and $\mathbf{K}_{33}$ are from the fluid potential–free surface subsystem, $\mathbf{M}_{44} = rM\,\delta_p$, $\mathbf{K}_{44} = rK\,\delta_p$ are the point mass and stiffness of the local resonator, $\mathbf{K}_{11}^{(r)} = (rK - i\omega rC)\,\delta_p$ represents the direct stiffness contribution of a spring–damper connected in parallel to the membrane at point δ_p, and $\mathbf{C}_{14} = \mathbf{C}_{41}^\top = -(rK - i\omega rC)\,\mathbf{B}$ describes the membrane–resonator coupling, where $\mathbf{B}$ is the rank-one coupling operator associated with δ_p.

Eliminating (ϕ, κ): pure fluid added mass.

The fluid potential–free surface subsystem satisfies

$$\begin{bmatrix} \mathbf{K}_{22} & \mathbf{C}_{23} \\ \mathbf{C}_{32} & \mathbf{K}_{33} \end{bmatrix} \begin{bmatrix} \phi \\ \kappa \end{bmatrix} = -\begin{bmatrix} \mathbf{C}_{21} \\ \mathbf{0} \end{bmatrix} \eta. \tag{B.3}$$

Define

$$\mathbf{M}_\phi(\omega) := \mathbf{K}_{22} - \mathbf{C}_{23}\,\mathbf{K}_{33}^{-1}\,\mathbf{C}_{32}, \qquad \phi = -\,\mathbf{M}_\phi(\omega)^{-1}\,\mathbf{C}_{21}\,\eta. \tag{B.4}$$

Substitute back into the membrane equation:

$$\big[\mathbf{K}_{11} + \mathbf{K}_{11}^{(r)}\big]\eta + \mathbf{C}_{14}q = \omega^2\Big(\mathbf{M}_{11} + \underbrace{\mathbf{C}_{12}\,\mathbf{M}_\phi(\omega)^{-1}\,\mathbf{C}_{21}}_{:=\,\mathbf{M}_{\mathsf{hat}}(\omega)}\Big)\eta. \tag{B.5}$$

$\mathbf{M}_{\mathsf{hat}}(\omega)$ is the added mass due to the pure fluid subsystem. Under conservative boundary conditions and properly treated radiation conditions, $\mathbf{M}_{\mathsf{hat}}(\omega)$ is (Hermitian) semi-positive definite.

Eliminating q: frequency-dependent stiffness correction.

The resonator subsystem satisfies

$$\big(\mathbf{K}_{44} - i\omega rC - \omega^2\mathbf{M}_{44}\big)\, q = -\,\mathbf{C}_{41}\,\eta, \qquad q = -\big(\mathbf{K}_{44} - i\omega rC - \omega^2\mathbf{M}_{44}\big)^{-1}\mathbf{C}_{41}\,\eta. \tag{B.6}$$

Substituting into (B.5), we obtain the effective EVP in η alone:

$$\Big[\mathbf{K}_{11} + \mathbf{K}_{11}^{(r)} + \underbrace{\big(-\,\mathbf{C}_{14}\big(\mathbf{K}_{44} - i\omega rC - \omega^2\mathbf{M}_{44}\big)^{-1}\mathbf{C}_{41}\big)}_{:=\,\mathbf{R}_{\mathsf{osc}}(\omega)}\Big]\eta = \omega^2\big[\mathbf{M}_{11} + \mathbf{M}_{\mathsf{hat}}(\omega)\big]\eta. \tag{B.7}$$

Here $\mathbf{R}_{\mathsf{osc}}(\omega)$ is a frequency-dependent stiffness correction induced by eliminating the resonator DOF.

Definition and explicit expression of effective added mass.

We move $\mathbf{R}_{\mathsf{osc}}(\omega)$ to the mass side and normalize by ω^2, defining

$$M_{\mathsf{add,eff}}(\omega) := \mathcal{A}(\omega) - \frac{1}{\omega^2}\,R_{\mathsf{osc}}(\omega), \qquad K_{11}\eta_h = \omega^2[M_{11} + \mathcal{A}(\omega) - \frac{1}{\omega^2}\mathcal{R}_{\lambda f}(\omega)]\eta_h \tag{B.8}$$

For a single-DOF point resonator, $\mathbf{K}_{44} = rK\,\delta_p$, $\mathbf{M}_{44} = rM\,\delta_p$, and $\mathbf{C}_{14} = \mathbf{C}_{41}^{\top} = -(rK - i\omega rC)\,\mathbf{B}$ (where $\mathbf{B}$ is a rank-one coupling operator), we obtain

$$\mathbf{R}_{\mathsf{osc}}(\omega) = -C_{14}\big(\mathbf{K}_{44} - i\omega rC - \omega^2\mathbf{M}_{44}\big)^{-1}\mathbf{C}_{41} \tag{B.9}$$

$$= \boxed{\frac{-(rK - i\omega rC)^2}{\big(rK - i\omega rC - \omega^2 rM\big)}}\,\mathbf{B}\,\mathbf{B}^{\top}. \tag{B.10}$$

Therefore,

$$\boxed{\mathbf{M}_{\mathsf{add,eff}}(\omega) = \mathbf{M}_{\mathsf{hat}}(\omega) \;+\; \frac{(rK - i\omega rC)^2}{\omega^2\big(rK - i\omega rC - \omega^2 rM\big)}\;\mathbf{B}\,\mathbf{B}^{\top}}. \tag{B.11}$$

In the undamped case $rC = 0$, equation (B.11) reduces to

$$\boxed{\mathbf{M}_{\mathsf{add,eff}}(\omega) = \mathbf{M}_{\mathsf{hat}}(\omega) \;+\; \frac{rK^2}{\omega^2\big(rK - \omega^2 rM\big)}\;\mathbf{B}\,\mathbf{B}^{\top}}, \quad \omega_r := \sqrt{rK/rM}. \tag{B.12}$$

It is clear that when $\omega < \omega_r$, the denominator is positive, and the resonator contributes positively to the mass side; when $\omega > \omega_r$, the denominator becomes negative, and the resonator contributes negatively. If its amplitude dominates, an effective negative mass may appear in certain directions. The pure fluid added mass $\mathbf{M}_{\mathsf{hat}}(\omega)$ remains semi-positive definite.